UNIVERSITY OF OKLAHOMA

GRADUATE COLLEGE

ANTENNA SYNTHESIS THROUGH CHARACTERISTIC MODAL ANALYSIS FOR SMALL UNMANNED AERIAL SYSTEM APPLICATIONS

A THESIS

SUBMITTED TO THE GRADUATE FACULTY

in partial fulfillment of the requirements for the

Degree of

MASTER OF SCIENCE

By

Garrett Philip Robinson

Norman, Oklahoma

2019

ANTENNA SYNTHESIS THROUGH CHARACTERISTIC MODAL ANALYSIS FOR SMALL UNMANNED AERIAL SYSTEM APPLICATIONS

A THESIS APPROVED FOR THE
SCHOOL OF ELECTRICAL AND COMPUTER ENGINEERING

BY

Dr. Jessica Ruyle, Chair

Dr. Hjalti Sigmarsson

Dr. Phillip Chilson

Table of Contents

List of Figures

Abstract

Historically, antennas for airborne applications have been a separate class unto themselves. They have unique requirements for conformality, structural integrity, and long-range communication. Furthermore, the must successfully meet these criteria in a metallic environment. The antennas designed for Small Unmanned Aerial Systems (SUAS) have more stringent requirements than their predecessors due to the inherent Size Weight and Power (SWaP) restrictions and the increased importance of consistent communication for remote operation. Previous work has proven the utility of conformal antennas with a quasi-isotropic radiation pattern in the enhancement of SUAS communication for non-metallic structures. These structures however are not suited for performance on a metallic SUAS or in a metallic environment. For metallic SUAS, a new antenna will be devised using the Method of Moments (MoM). The following antenna synthesis procedure optimizes performance by taking into account the modality of the deformed ground structure the antenna is placed upon. The performance of this antenna will be assessed.

Chapter 1

Introduction

1.1 Motivation

Antenna design for standard airborne platforms is a unique and complex problem. The antennas must be able to operate in a metallic environment while maintaining a small aerodynamic form factor that is structurally sound [1]. Most SUAS are non-metallic, and thus avoid significant pitfalls in regards to mutual coupling. However, the antennas for these platforms are further limited by a compressed form factor and tighter SWaP constraints [2]–[4]. A further design consideration is that the SUAS needs to maintain a constant communication link with the controller or ground station throughout the craft's maneuvers as they are remotely operated [5], [6]. These two design factors are traditionally at odds with each other. For applications primarily concerned with electrical size, inductively loaded monopole antennas with rubber shielding are widely used. These "rubber duck" antennas have become commonplace throughout commercial electronics. However, they are not suitable for SUAS communications as they negatively affect aerodynamics, contain radiation nulls, and become increasingly inefficient as their electrical size decreases [7], [8]. At the other end of the optimization curve, almost all quasi-isotropic radiators are either too inefficient for long-range communication, or are neither conformal nor

electrically small and thus produce too much drag for use on a SUAS [9]–[11]. In order to adequately satisfy both requirements for SUAS communication, the primary focus of this work is aerodynamic quasi-isotropic antennas.

An ideal SUAS antenna would be purely isotropic to enable a communication link to the control station regardless of platform orientation. However, this is not merely difficult but mathematically impossible [12]–[16]. By focusing the design on quadcopters, the desired antenna pattern is altered because these platforms do not require the steep bank-angles for turning and altitude adjustments that fixed wing SUAS do. Instead of requiring a true quasi-isotropic pattern, the quadcopter SUAS simply needs the lower hemisphere of the antenna's radiation pattern to be null-free. This will enable the craft to maintain a communication link with ground control while safely completing all standard maneuvers. In situations where air-air communication is a priority, further consideration would have to be given to the radiation pattern in the upper hemisphere.

Although the antennas researched in [17] meet the standards for non-metallic SUAS, they are not suitable for metallic SUAS. This is because the mutual coupling between the conformal antenna and the metallic SUAS dramatically reduces the radiation efficiency[18]. Instead, an antenna that utilizes the structure of the SUAS in its design through the theory of characteristic modes will be created. Previous work has detailed the ability to generate radiating currents on the surface of commercial aircraft [1], [19], [20] while other work [21]–[23] has detailed the practicality of using MoM to create a wideband antenna that efficiently utilizes the conducting structure as a radiator. The following work will show that the generalized concepts presented in these papers can be applied to successfully create a quasi-isotropic radiation pattern on a metallic SUAS through the use of MoM.

1.2 Thesis Outline

This thesis begins in chapter two by introducing the antenna structures prevalent in Small Unmanned Aircraft Systems and assesses the general disadvantages they may have for broad use in such applications. This chapter continues with a brief survey of less commonplace novel and PCB-integrated structures included for consideration. The mathematical foundation for method of moments and its application to the theory of characteristic modes is then covered in chapter three. Chapter four discusses the antenna synthesis process through its completion and the finalized design of the SUAS antenna. The fabrication of this antenna is then covered in chapter five with the relevant measurements discussed in the following chapter. Chapter seven forms the conclusion to the thesis with a summary of the previous research and a description of future work.

Chapter 2

A Review of Existing SUAS Antennas

2.1 Introduction

One of the primary problems with SUAS communication comes down to electrical size. Because the attenuation of a communication signal propagating over free space is given by the Friss Transmission Formula as

$$Loss = 20 \log_{10} \frac{4\pi d}{\lambda} \tag{2.1}$$

[24], a higher frequency signal (with a smaller wavelength) will have a greater attenuation over the same distance. So, a relatively low operating frequency is desirable for SUAS transmitters that are necessarily low powered. The choice of using a lower operating frequency however comes at a cost. Since the dimensions of resonant antennas are often given in terms of a wavelength, for example the halfwave dipole antenna, the antenna size increases inversely proportional to the operating frequency. Because of this, the SWaP benefits of using a lower frequency signal for transmit efficiency must be balanced with the SWaP benefits of using a high frequency antenna to minimize the form factor of the radiating element. As a compromise, most commercially available long-range SUAS radios operate

at approximately 900 MHz. This poses a significant problem for the SUAS. The wavelength of a 900 MHz signal is approximately 33 cm, which means that many traditional antennas, including a standard halfwave dipole, would be prohibitively large. The sheer size of these antennas makes them impractical for use in SUAS that often have maximal dimensions smaller than this.

The first commercial solution to this problem is the omni-present inductively loaded monopole antenna or ”rubber duck”. In addition to this type of antenna, the skew-planar antenna described in [25], [26] is increasingly prevalent because it provides a circularly polarized radiation pattern. Although both of these antennas provide a theoretical quasi-isotropic radiation pattern in the azimuthal plane, there are significant nulls that exist along the central axis of the antenna [24], [25]. With these nulls, it is impossible for the SUAS to maintain a constant data link to the ground station over the full range of flights.

2.2 Rubber Duck Antennas

Many generalized commercial antennas fall under the classification of ”rubber duck” antennas. These antennas are primarily inductively loaded monopoles and whip antennas that are sheathed in a rubberized or plastic casing. Rubber duck antennas have proliferated throughout the field of radio communications because they are cheap to produce, relatively small, and have a theoretical radiation pattern that closely approximates an isotropic pattern in the azimuthal plane.

Many other wire antenna configurations, including a wire dipole or a standard monopole antenna, would provide a higher gain and a better characterized radiation pattern. However, the rubber duck antenna has commercially prevailed because of its rugged design and compact form factor for low frequency applications.

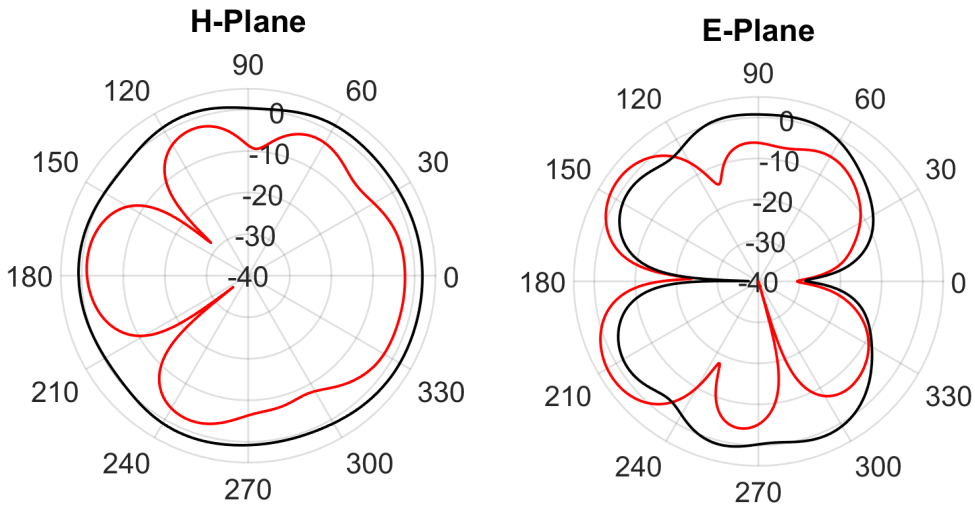

Figure 2.1: Measured radiation patterns for rubber duck antennas implemented with a half-wave dipole (black) and a coil loaded electrically small whip (red) [17]

While these antennas seem to meet many criteria for low cost radio communication, the actual resulting radiation pattern is far less consistent than the theoretical pattern. As can be seen in research done by [27] and in the measurements shown in Figure 2.1, many practical applications for these rubber duck antennas simply do not meet the established theoretical criteria for quasi-isotropic radiation in the azimuthal plane. While the loss in realized gain in the H-Plane can be explained by the loss in efficiency caused by inductively loading the monopole antenna [7], [8], there are significant nulls in this radiation plane that are over -30 dB in magnitude. One possible reason for these radiation nulls is that the electrical connection of these antennas does not approximate the infinite ground plane used in their theoretical characterization. Instead, they are simply attached to the SUAS in a place that is mechanically convenient regardless of if the location is electrically significant. This poor placement can be seen in Figure 2.2. The antenna is simply affixed to the outmost side of the plastic craft, with the internal circuitry and battery compartment located close enough that these elements can be loosely identified as a ground

Figure 2.2: Antenna configuration of the included coiled monopole rubber duck antenna on the IRIS craft used as an antenna test platform [17]

plane. However, the craft's internals provide a irregular ground plane model at best. At worst, this placement causes a significant deterioration in the realized radiation pattern because of unintended mutual coupling and loading effects. In the end, these radiation nulls make fully controlled scientific SUAS flights impossible because they cause the ground station to lose manual control of the craft during certain maneuvers and also cause spikes in the bit error rate (BER) as valuable data is permanently lost.

2.3 Skew-Planar Antennas

The skew-planar antenna, or cloverleaf antenna, has become increasingly popular in SUAS communication. First proposed by [26], the skew-planar antenna is characterized by three to five elements that are one wavelength long each consisting of

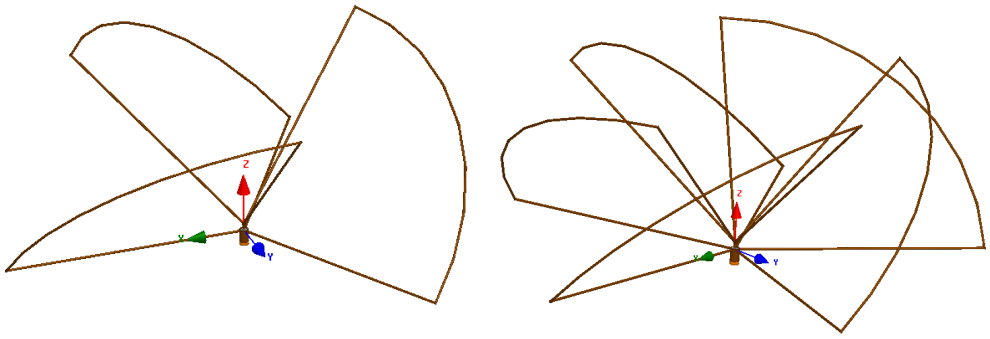

Figure 2.3: Cloverleaf antenna geometries: 3 element (left) and 5 element (right) [17]

two quarter wavelength straight sections connected by a half wavelength arc. As depicted in Figure 2.3, these elements are radially distributed around a center axis at a forty-five degree angle. This design provides a quasi-isotropic pattern in the azimuthal plane, is circularly polarized, and has a VSWR-less-than-two fractional bandwidth of 14.58% [25]. The bandwidth of the antenna is wideband enough to perform on almost any commercially available SUAS radio. Another comparative advantage of the skew-planar antenna over the rubber duck antenna is the fact that it does not need a ground plane and thus is significantly more placement insensitive for the majority of plastic and foam based SUAS.

While this antenna design has several impressive benefits, its drawbacks for SUAS communication are as notable. Of primary consideration is the sheer size of the antenna. The skew-planar antenna occupies a quasi-spherical space that is a wavelength in diameter and $\frac{\sqrt{2}}{4}\lambda$ tall. For a skew-planar antenna at 900 MHz, this corresponds to a space roughly 33 cm across and 12 cm tall. This is entirely too large for a standard SUAS due to SWaP constraints. Because of this, many skew-planar communication systems for SUAS opperate at 5.8 GHz. While this does mitigate the size of the antenna, it does so at the cost of significantly increasing

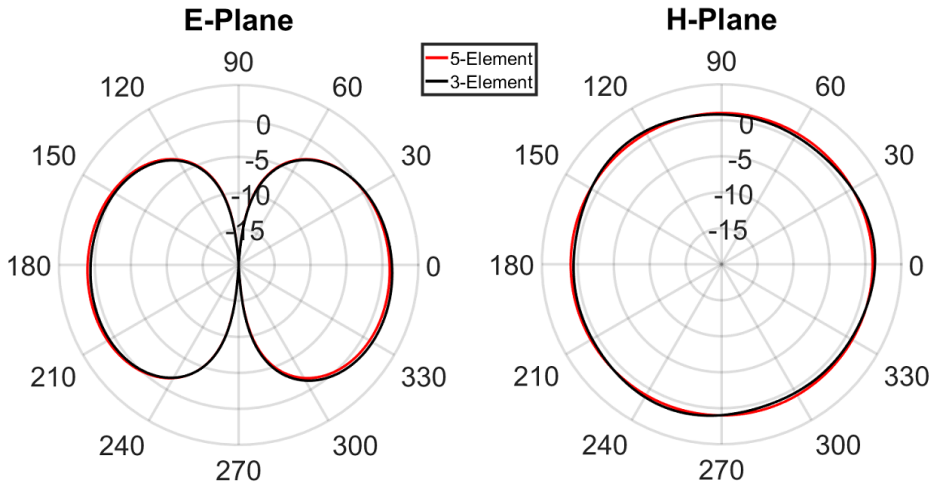

Figure 2.4: Far-field realized gain of 3-element and 5-element cloverleaf antennas [17].

the path loss of the transmitted signal and thus limiting the maximum craft range. In addition to the practical problem posed by its size, the skew-planar antenna still has a null about its feed axis [25] that necessitates that for some craft orientation in reference to the base station there will be significant communication loss.

Even though the skew-planar antenna does perform better in many categories than the rubber duck antennas, it is still not optimal for SUAS communication. The skew-planar antenna has a central null, shown in Figure 2.4. and can only be a suitable size for standard SWaP constraints at a significantly higher frequency, which correspondingly increases the signal loss. In the end, the combination of the prohibitive size of the skew-planar antenna and the central null in its radiation pattern severely limits its practicality for SUAS operation.

2.4 Conformal Planar Antennas

As previously discussed, outside of the standard SWaP considerations that must be taken into account for SUAS antennas is the desire for a conformal antenna system

that would minimize the drag and loss of aerodynamic efficiency caused by many standard antennas. There are two planar antennas that have proven to be effective for SUAS applications when conformally applied to the plastic shell: impedance modified loops and curved folded dipole antennas (CFDA). These antennas are made to be conformal by creating the antenna on a very thin (10-15 mil thick) substrate that can then be attached to the SUAS with minimal seperation. Although both antennas offer superior performance in comparison to rubber duck antennas for plastic SUAS communication, they are impractical for a metallic bodied SUAS.

Conformal loop antennas were studied as part of the research into SUAS antennas done in [17]. The primary concern with loop antennas comes down to the impedance of the structure itself. While electrically small loop antennas would be preferable from a SWaP perspective, these antennas are very inefficient transmitters because they have a real impedance much lower than 50 Ω and a relatively high reactance and thus become impractical [28]. Full wave loop antennas have the opposite problem. Although they have a low reactance, the impedance is similar to that of a folded dipole antenna, typically falling in the range between 270-300 Ω depending on the final design [24]. Once again, this impedance mismatch causes a significant degradation in the efficiency of the antenna. Although the difficulties with impedance matching seem to relegate the loop antenna's utility for SUAS communication, a solution to this mismatch was proposed in [29]. Starting with a full wavelength loop that has a relatively small reactance at its operating frequency, the addition of a metal region inside of the circumfrence of the loop successfully "loads" the loop and reduces its real impedance at the operating frequency to the point that it can be matched in a 50 Ω system. Fabricated versions of this antenna can be seen in Figure 2.5. The resulting radiation pattern is approximately that of a standard dipole.

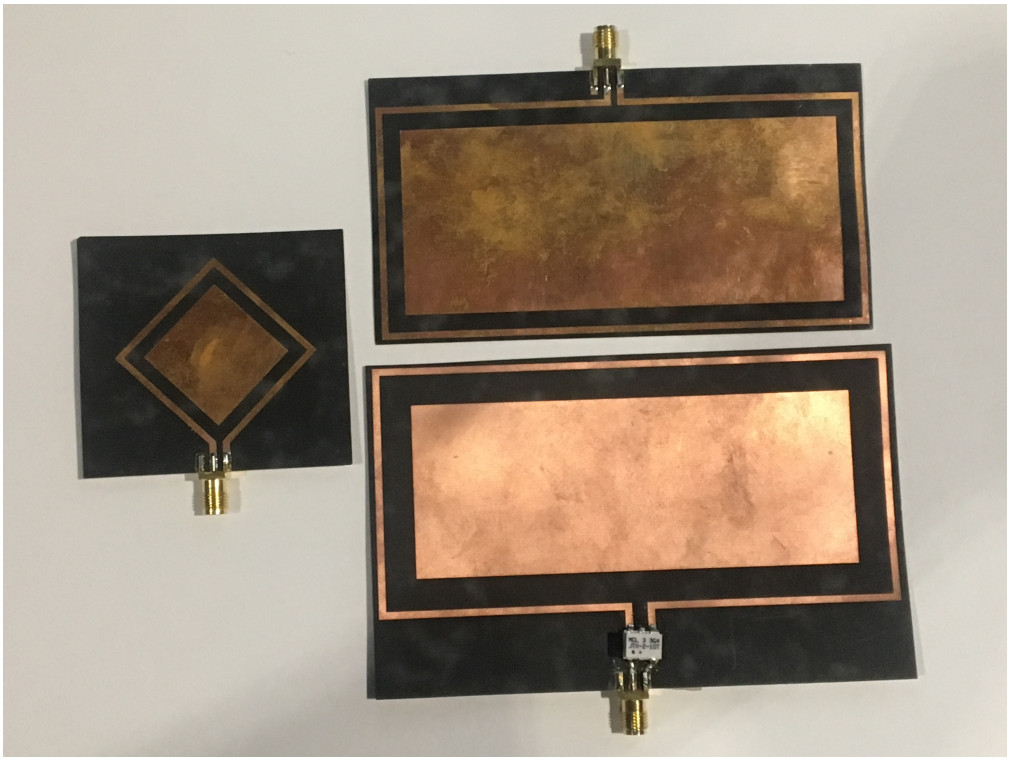

Figure 2.5: Fabricated Loop antennas: 2.4 GHz 50 Ω diamond loop (left), 915 MHz 50 Ω rectangular loop (top), and 915 MHz 100 Ω rectangular loop with 2:1 chip balun (bottom) [17]

CFDA antennas were also studied as part of the research into SUAS antennas done by [17]. The CFDA antenna was originally proposed by [30] as a quasi-isotropic radiator for radio communication networks. The basic theory of the antenna is that by curving a folded dipole around a central axis, as shown in Figure 2.6, it is possible to create a quasi-isotropic far field from the linear superposition of circularly positioned finite sections of a folded dipole. Additionally, the curvature of the CFDA lowers the real input impedance of the antenna from the 280 Ω expected of a standard folded dipole antenna to approximately 50 Ω. As a naturally matched antenna with a quasi-isotropic far field pattern, the CFDA is an appealing design choice for SUAS communication.

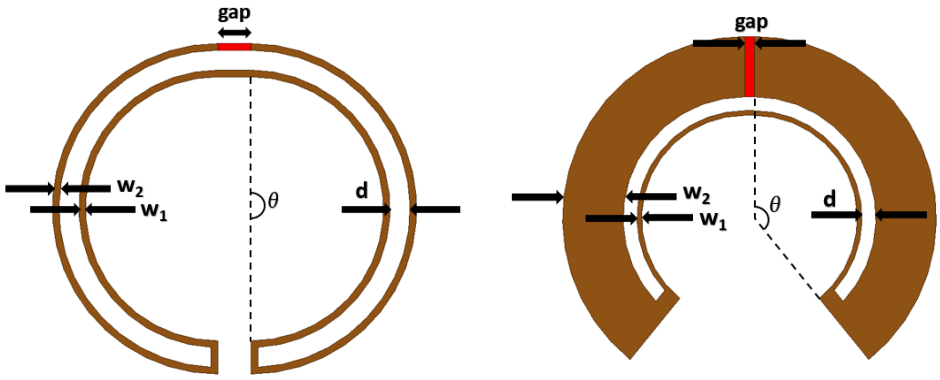

Figure 2.6: Geometry and design parameters for the curved folded dipole antenna in the nominal equal width configuration (left) and a wideband configuration (right) [17]

While both the loaded loop antenna and the CFDA show many positive characteristics for a conformal planar antenna design, both have problems that make them unsuitable for metallic SUAS communication. To begin with, the loaded loop antenna, much like the folded dipole antenna, has a null in its azimuthal far field radiation pattern that would limit the communication performance of this antenna at longer distances. This issue though is relatively insignificant for both of these antennas though in comparison to the placement sensitivity due to electrical loading and impedance shifts caused by a closely located ground plane. For both antennas, it has been experimentally shown that the far field radiation pattern has significant divergence from the theoretical expectations when placed near large metallic objects, including the battery and other craft internals [17]. These differences include the occurrence of significant nulls in the far field pattern and significant shifts in the operational frequency of the antenna. Although this loading effect does not significantly affect the craft when placed on the wings of a foam based fixed wing SUAS, it is detrimental to the performance of the antenna on a quadcopter body, which typically has densely packed internal components. The practical results of

this loading can be seen in Figures 2.7 and 2.8. The placement sensitivity of the CFDA is a significant disadvantage for using this style of antenna for quadcopter SUAS communication.

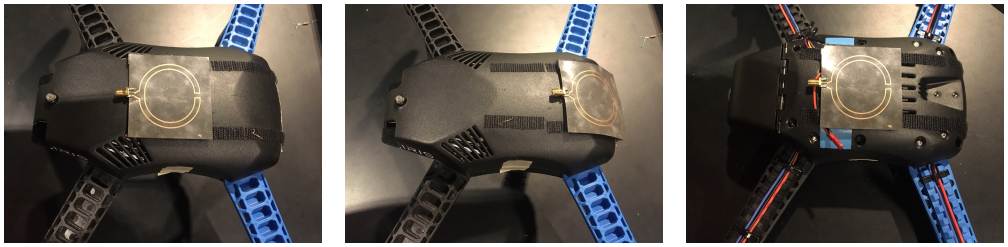

Figure 2.7: Conformally mounted 20-MHz-bandwidth CFDA variation in the top (left), rear (middle), and bottom (right) positions [17]

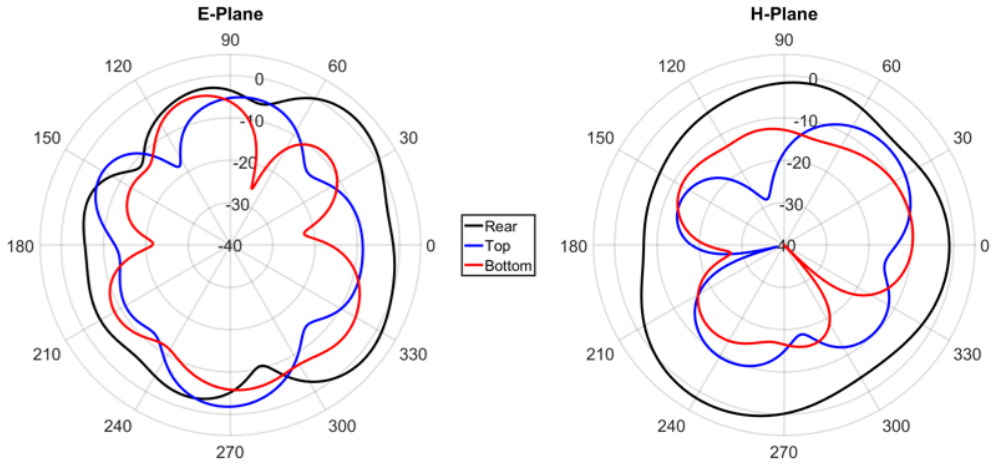

Figure 2.8: Radiation pattern E-Planes (left) and H-Planes (right) of 20 MHz nominal CFDA conformally attached to IRIS aircraft in top, bottom, and rear locations showing impact of placement on antenna functionality [17]

One potential solution to the problem of degraded performance is to utilize a metallic groundplane on the underside of the SUAS to limit the coupling between the radiating element and the densely packed electronics stored inside the craft's body. However, these planar antennas perform significantly worse in the presence of a ground plane. This is because the efficiency of these antennas are dramatically

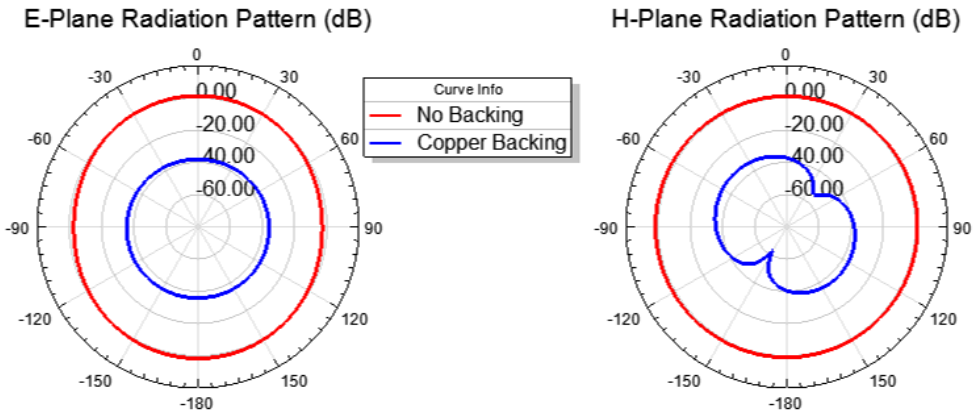

Figure 2.9: Comparison of CFDA simulated realized gain between an antenna with a substrate that is backed by an air box and an antenna with a ground plane added to the substrate.

impacted by the significant decrease in impedance caused by closely placing the antennas next to a ground plane [31]–[33]. Because the most efficient long range SUAS communication systems operate at approximately 900 MHz, the 10-15 mil separation between the conformally placed planar antenna and the ground plane created by the metallic SUAS would only be equivalent to less than 0.004λ even when you account for the shorter effective wavelength within the dielectric. The resulting model for this case includes an image of the excited antenna nearly collocated with the original antenna [34]. The minuscule electrical separation reduces the effective radiation efficiency of the antenna to nearly zero [31]. The only way to solve this problem is to increase the electrical separation between the excited antenna and the ground plane. However, once this seperation is adequately increased, the antenna is no longer conformal nor practical for SUAS communication due to SWaP considerations. This change can be clearly seen in Figure 2.9. After the addition of the ground plane to the model, the antenna which had quasi-isotropic performance essentially became a resistive load. In the end, while these conformal antennas are potential solutions for plastic and foam based SUAS, they are not

practical for metallic SUAS communication and have degraded performance when used on quadcopters.

2.5 Chapter Summary

Many different antennas have been previously proposed for SUAS communication. While they all have practical benefits, there are significant limitations in their application on metallic SUAS. The omnipresent rubber duck antenna is cost effective, compact, and would have an improved radiation pattern when applied to a metallic SUAS that could provide a consistent ground plane. However, that radiation pattern still includes a significant null colinear to its central axis and a limitation in realized gain caused by inductive loading. The skew planar antenna provides a circularly polarized radiation pattern and a higher realized gain than the rubber duck antenna. Once again though there is a radiation null in the far field colinear to the central axis, the antenna is prohibitively large at the frequencies most efficient for long range communication, and the addition of an electrically close ground plane would reduce the radiation efficiency significantly. Both planar antennas, the loaded loop antenna and the CFDA, are cost effective antennas that offer quasi-isotropic radiated far fields when conformally applied to plastic SUAS. When the SUAS is a quadcopter with densely packed components though, the resulting radiation patterns show significant degradation from the theoretical measurements. When a metallic ground plane is introduced to limit the coupling between the radiating element and the craft internals, the resulting efficiency of these conformal antennas is reduced to the extent that they are practically no longer radiating. Clearly, a new antenna must be designed that can accurately meet the SWaP constraints of SUAS communication while maintaining null free radiation in the lower hemisphere when used

in conjunction with a quadcopter or metallic SUAS.

Chapter 3

Method of Moments

3.1 Introduction

Instead of attempting to design an antenna that works in spite of the metallic body of the SUAS, it is a far better process to design an antenna that utilizes the metallic structure to its advantage. One of the best ways to do this is through the use of Characteristic Modal Analysis (CMA). CMA is a technique that provides insight into the radiation patterns intrinsic to a metallic object by analyzing the fundamental modes of current dispersion on the objects surface. Method of moments (MoM), the mathematical basis of CMA, is first detailed to aid in the conceptual understanding of CMA. After an example of MoM applied to a bounded ordinary differential equation, CMA is then summarized. This summary includes several points of analysis that become the basis for the antenna synthesis detailed in the next chapter of this thesis.

3.2 The Method of Moments

Mathematical problems without closed form solutions have posed a challenge for scientists and mathematicians for centuries. In this situation, numerical approxima-

tions are the closest that any researcher could get to the solution. However, these approximations are necessarily inexact and tedious to calculate by hand. Computers solved this problem. The accuracy of approximations calculated by computers increased to the point that they effectively solved for the exact solution in practical applications. The only remaining problem now is the computational speed of these solutions. MoM is a procedure for solving mathematical problems through linearization. It is especially efficient because computers operate linearly. At a basic level, the MoM works to functionally reduce an integro-differential equation into a basic linear function that can be solved through matrix inversion and multiplication. Although it is often referred to as an approximation technique in totality, that is not the case. This method can be applied to almost any problem and will produce exact solutions when a closed form solution does exist.

The mathematical basis for the method of moments has been described by numerous publications. While the general idea of converting functional equations to linear matrix equations began with Galerkin around 1920 [35], it was not until Harrington and Mautz's work in the early 1970s on applying the MoM to solving eigenvalue problems [36], [37] that the theory became popular. The process of the MoM according to Harrington begins with the supposition that there is an inhomogeneous equation in the form of

$$L(f) = g. \tag{3.1}$$

In this equation, L is a known linear operator between f and g, g is a known function, and f is what is being solved for. For this space, it is necessary to have a defined inner product that satisfies the following criteria for functions f,g, and h

using constants α and β:

$$\begin{aligned} \langle f, g \rangle &= \langle g, f \rangle \\ \langle \alpha f + \beta g, h \rangle &= \alpha \langle f, h \rangle + \beta \langle g, h \rangle \\ \langle f^*, f \rangle &> 0 \quad \text{if} \quad f \neq 0 \\ \langle f^*, f \rangle &= 0 \quad \text{if} \quad f = 0 \end{aligned} \tag{3.2}$$

Once a satisfactory inner product is defined, the next step is to create a representative expansion of f with a series of known linearly independent functions $\tilde{f}_1, \tilde{f}_2, \tilde{f}_3, ..., \tilde{f}_N$. Therefore, the function f can be fully represented as

$$f = \sum_n \alpha_n \tilde{f}_n. \tag{3.3}$$

In Equation 3.3, the terms α_n are coefficients that properly weight the linear combination of $\tilde{f}_n$. In general, the terms $\tilde{f}_n$ are often referred to as expansion functions or basis functions as they are a subset of functions that span the functional space. This summation has three distinct cases:

1. an exact and finite decomposition of f when a closed form solution exists,

2. an approximated and finite decomposition of f when a closed form solution does not exist, and

3. an exact and infinite decomposition f for any linearizable problem.

However, since a problem with a closed form solution is often not a practically interesting problem and a solution that is infinite in extent does not lend itself to forthright analysis, the majority of practical problems that the MoM is applied to are approximated by a finite functional decomposition. This is why the MoM is

often incorrectly referred to in totality as an approximation technique.

In the next step of the derivation of MoM, Equation 3.3 is substituted into Equation 3.1. Due to the principle of linearity, which states that for every linear operator L, vector f, and constant c: $L(\mathrm{c}f) = \mathrm{c}L(f)$, the resulting equation in the functional subdomain is seen as:

$$\sum_n \alpha_n L(\tilde{f}_n) = g. \tag{3.4}$$

The next step is in part an error correction formulation. In a process described by Chen and Ney [38] for a practical application of MoM that induces some error due to the incomplete decomposition of f, Equation 3.3 should actually be written as

$$f \approx \tilde{f} = \sum_n \alpha_n \tilde{f}_n. \tag{3.5}$$

In this situation, the error can be calculated as

$$R = L(\tilde{f}) - g \tag{3.6}$$

where R is equal to the calculated error. In order to practically reduce the theoretical error in this case, known weighting functions in the range of L denoted as w_m, representative of $w_1, w_2, w_3, ..., w_m$, are incorporated such that the inner product of the two falls within the kernel of the functional range. In other words,

$$\langle R, w_m \rangle = 0. \tag{3.7}$$

The next step in the formulation of MoM begins by taking the inner product of each side of Equation 3.6 with respect to w_m:

$$\langle R, w_m \rangle = \langle Lf - g, w_m \rangle. \tag{3.8}$$

but, because of how w_m is defined it can be stated that Equation 3.8 reduces to

$$0 = \langle Lf - g, w_m \rangle. \tag{3.9}$$

In accordance to Equations 3.2, Equation 3.9 reduces to

$$\langle Lf, w_m \rangle = \langle g, w_m \rangle. \tag{3.10}$$

By substitution with Equation 3.3, it can be shown that Equation 3.10 is equivalent to

$$\langle L(\sum_n \alpha_n \tilde{f_n}), w_m \rangle = \langle g, w_m \rangle. \tag{3.11}$$

Applying linearity once again leads to the equation

$$\sum_n \alpha_n \langle w_m, L(\tilde{f_n}) \rangle = \langle w_m, g \rangle. \tag{3.12}$$

This equation can now be visualized as a fully linearized system that can be written as

$$\left[l_{mn}\right]\left[a_n\right] = \left[g_m\right] \tag{3.13}$$

where l_{mn} is an MxN matrix defined as

$$\left[l_{mn}\right] = \begin{bmatrix} \langle w_1, L(\tilde{f_1}) \rangle & \langle w_1, L(\tilde{f_2}) \rangle & ... & \langle w_1, L(\tilde{f_N}) \rangle \\ \langle w_2, L(\tilde{f_1}) \rangle & \langle w_2, L(\tilde{f_2}) \rangle & ... & \langle w_2, L(\tilde{f_N}) \rangle \\ \vdots & \vdots & \ddots & \vdots \\ \langle w_M, L(\tilde{f_1}) \rangle & \langle w_M, L(\tilde{f_2}) \rangle & ... & \langle w_M, L(\tilde{f_N}) \rangle \end{bmatrix}, \tag{3.14}$$

α_n is a Nx1 matrix defined as

$$\left[\alpha_n\right] = \begin{bmatrix} \alpha_1 & \alpha_2 & ... & \alpha_N \end{bmatrix}^T, \tag{3.15}$$

and g_m is a Mx1 matrix defined as

$$\left[g_m\right] = \begin{bmatrix} \langle g, w_1 \rangle & \langle g, w_2 \rangle & ... & \langle g, w_m \rangle \end{bmatrix}^T. \tag{3.16}$$

If the number of weighting coefficients is equal to the number of expansion functions (i.e. M=N), then the resulting matrix l_{mn} is a square matrix. So long as it is not singular, the coefficients a_n can then be found by matrix inversion through the formula:

$$\left[a_n\right] = \left[l_{mn}^{-1}\right]\left[g_m\right]. \tag{3.17}$$

The solution for f, the original unknown being solved for, is thus given by Equation 3.3 as

$$\left[f\right] = \left[\tilde{f}\right]\left[\alpha_n\right] = \left[\tilde{f}\right]\left[l_{mn}^{-1}\right]\left[g_m\right] \tag{3.18}$$

where

$$\left[\tilde{f}\right] = \begin{bmatrix} f_1 & f_2 & ... & f_N \end{bmatrix} \tag{3.19}$$

This is the end of the generalized formulation of the MoM. While this is presented as a direct and unified theory, there is a great divergence in potential solution accuracy and computational speed caused by an infinite set of choices for defining both w_m and f_n [37]–[40]. In general, a compromise must be made between absolute accuracy and computational efficiency in the choice of both the weighting coefficients and basis functions as for problems without a closed form solution it is impossible to practically achieve the conditions set forth by Equation 3.7. Instead,

the error caused by the approximation of f by the basis functions f_n must simply be reduced. A common method for this reduction is actually the original method that was proposed, the Galerkin Method [35], [37]. The Galerkin method is defined as setting the weighting functions equivalent to the basis functions ($w_m = f_n$). This method, which can be shown to be the same as the Rayleigh-Ritz variational method [41], [42], is an effective way to minimize the inherent error in the MoM approximation.

By realizing that the inner product defined by Equation 3.2 can be viewed as a projection onto a vector subspace, it can be seen that Equation 3.12 is merely equating vector projections. In general, vector projections are a way to calculate the proportion of an existing vector that exists in a smaller subspace. An example of this is the simple dot product used to calculate electric flux. The dot product, which is a type of inner product, equates the flux passing through a surface to the projection of the electric field, defined within a third order vector space, into the vector subspace defined by the normal vector, which is a first order space. In this example, it is easy to see that the result of this operation lies fully within the secondary vector subspace while the rest of the original vector is defined as existing in a two-dimensional orthagonal subspace. When looking at the resulting order of each of these subspaces it can be seen that

$$Order(E) = Order(P) + Order(R) \tag{3.20}$$

where $Order(E)$ is the order of the Cartesian vector space defining the electric field, $Order(P)$ is the order of the subspace defined by the normal projection, and $Order(R)$ is the subspace orthogonal to the projection. Although this example is simplistic in nature, it can be generalized to hold for more complex vector projec-

tions, including the vector projection in the MoM derivation.

In the MoM defined by Equation 3.12, the first vector projection is the projection of the approximation of $L(f)$, represented by $L(\tilde{f})$, projected onto the subspace spanned by w_m and is seen by $\langle L(\sum_n \alpha_n \tilde{f}_n), w_m \rangle$. The second vector projection is the projection of $L(f)$ onto the same subspace and is seen as $\langle w_m, g \rangle$. The minimum error, R, described earlier can thus be seen as the orthogonal vector space that exists between the range of $L(f)$ and the subspace spanned by the finite number of basis functions $L(\tilde{f})$. By equating the range of the approximation to the to the subspace spanned by the weighting functions, the error is minimized to merely be the inner product of the error function with itself

$$\text{Error} = \langle R, R \rangle \tag{3.21}$$

[38]. Because the inherent approximation error is caused by the subspace spanned by the basis functions having a lower order than the original range of $L(f)$, the error can be further minimized as the order of $L(\tilde{f})$ approaches the order of $L(f)$. While this is a feasible bound when a simplistic closed form solution exists, exact solutions to many complex problems are computationally impossible because the convergence of the two vector spaces would require an infinite order subspace of expansion functions.

3.3 Solving an Ordinary Differential Equation

Although the MoM may seem difficult to implement due to the generalized definition seen in the preceding section, the following example showing the solution to a standard boundary value problem elucidates the methodology more directly.

Similar to an example done by Harrington in [37], the boundary value problem is that:

$$-\frac{\partial^2 f}{\partial x} = 1 + 4x^2 + 3x^4 \tag{3.22}$$

where $f(0) = f(1) = 0$. Going back to the inhomogeneous equation defined in Equation 3.1, it can be seen that

$$L = -\frac{\partial^2}{\partial x} \tag{3.23}$$

$$f = f \tag{3.24}$$

$$g = 1 + 4x^2 + 3x^4. \tag{3.25}$$

The first step after identifying the parts of the inhomogeneous equations is selecting a set of basis functions $\tilde{f}_n$ that will represent the function f. With the consideration that $\tilde{f}_n$ must meet the stated boundary conditions [38], the basis functions $f_n = x - x^{n+1}$ were selected. This basis is comprised of a linear combination of the standard polynomial basis function $f_n = x^n$ for $n \geq 0$, which spans the entire functional domain. To demonstrate the utility of the Galerkin method, the weighting functions w_m are defined as

$$w_m = f_n = x - x^{m+1}. \tag{3.26}$$

Next, a suitable inner product must be defined. Because this problem exists in the n dimensional functional space existing between $f(0)$ and $f(1)$, the inner product is defined as

$$\langle u, v \rangle = \int_0^1 u(x) \cdot v(x) dx \tag{3.27}$$

where u and v are both functions over the domain of x.

Now, the matrix $\left[l_{mn}\right]$ can be calculated. In accordance to Equations 3.12, 3.13, 3.26, and 3.27, the values within the matrix are defined by:

$$\begin{aligned}
\langle w_m, L(f_n)\rangle &= \int_0^1 w_m \cdot L(f_n)dx \\
&= \int_0^1 (x - x^{m+1}) \cdot -\frac{\partial^2}{\partial x}(x - x^{n+1})dx \\
&= \int_0^1 (x - x^{m+1}) \cdot (n+1)(n)x^{n-1}dx \\
&= (n+1)(n)\int_0^1 (x - x^{m+1})x^{n-1}dx \\
&= (n+1)(n)\int_0^1 x^n - x^{m+n}dx \\
&= (n+1)(n)\left[\frac{1}{n+1}x^{n+1} - \frac{1}{m+n+1}x^{m+n+1}\right]_0^1 \\
&= (n+1)(n)\left[\frac{1}{n+1} - \frac{1}{m+n+1}\right] \\
&= n - \frac{(n+1)(n)}{m+n+1} \\
&= \frac{mn}{m+n+1}.
\end{aligned} \tag{3.28}$$

Therefore, the value at any index of the matrix is given in terms of it's indices.

Likewise, the matrix $\left[g_m\right]$ can also be solved for using Equations 3.12, 3.13,

3.26, and 3.27. The matrix values are defined by:

$$\begin{aligned}
\langle w_m, g\rangle &= \int_0^1 w_m * g dx \\
&= \int_0^1 (x - x^{m+1})(1 + 4x^2 + 3x^4) dx \\
&= \int_0^1 x + 4x^3 + 3x^5 - x^{m+1} - 4x^{m+3} - 3x^{m+5} dx \\
&= \left[\frac{1}{2}x^2 + x^4 + \frac{3}{6}x^6 - \frac{1}{m+2}x^{m+2} - \frac{4}{m+4}x^{m+4} - \frac{3}{m+6}x^{m+6}\right]_0^1 \\
&= 2 - \frac{1}{m+2} - \frac{4}{m+4} - \frac{3}{m+6}
\end{aligned} \tag{3.29}$$

Once the equations for $\left[l_{mn}\right]$ and $\left[g_m\right]$ are established, the matrices can then be put into MATLAB to solve for f using Equation 3.18. The results for each round of processing are as follows:

1. $\left[a_n\right] = \left[1.3143\right]^T$

   $\therefore f \approx 1.3143(x - x^2)$

2. $\left[a_n\right] = \left[\begin{array}{cc} -.2214 & 1.0238 \end{array}\right]^T$

   $\therefore f \approx .8024x + .2214x^2 - 1.0238x^3$

3. $\left[a_n\right] = \left[\begin{array}{ccc} .6786 & -.4762 & .75 \end{array}\right]^T$

   $\therefore f \approx .9524x - .6786x^2 + .4762x^3 - .75x^4$

4. $\left[a_n\right] = \left[\begin{array}{cccc} .4643 & .1667 & 0 & .3 \end{array}\right]^T$

   $\therefore f \approx .931x - .4643x^2 - .1667x^3 - .3x^5$

5. $\left[a_n\right] = \left[\begin{array}{ccccc} .5 & 0 & .3333 & 0 & .1 \end{array}\right]^T$

   $\therefore f \approx .933x - .5x^2 - .3333x^4 - .1x^6$

6. $\begin{bmatrix} a_n \end{bmatrix} = \begin{bmatrix} .5 & 0 & .3333 & 0 & .1 & 0 \end{bmatrix}^T$

$\therefore f \approx .933x - .5x^2 - .3333x^4 - .1x^6$

Because the sixth order solution, where order is defined as the order of the matrix $\begin{bmatrix} g_m \end{bmatrix}$, is equivalent to the fifth order solution, it can be stated that the process converged on the closed form solution to the ODE on the fifth attempt. This can be proved by simply verifying that the calculated function fulfills the conditions of the boundary value problem.

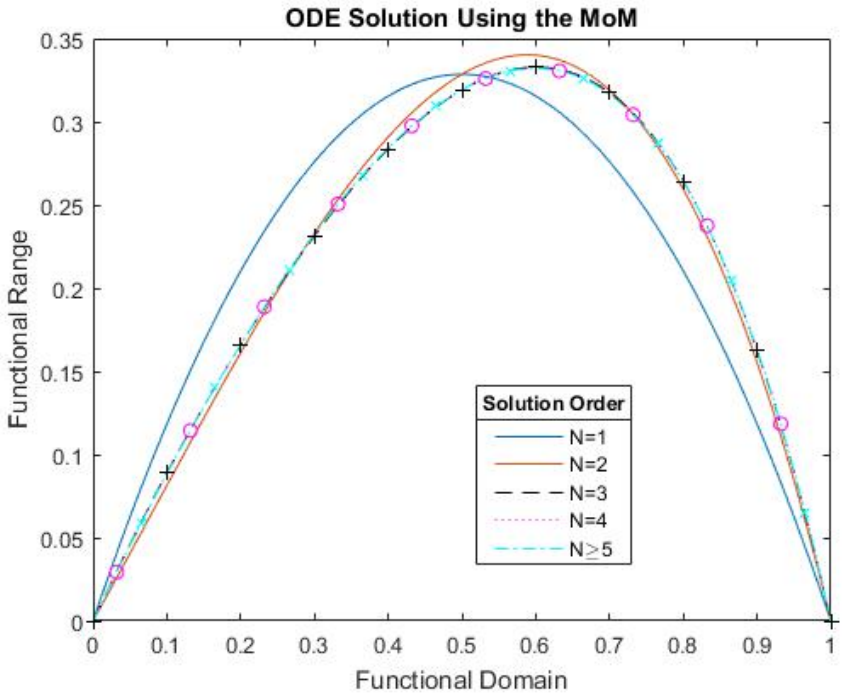

Figure 3.1: The iterative solution to an ODE problem using the Method of Moments

The results of this iterative process are shown above in Figure 3.1. Visually, it is possible to see that although the first order solution varies significantly from the closed form solution, the second order solution has minimal variation and all subsequent solutions are practically equivalent to the closed order solution. Although this is an introductory example to the application of the MoM, the results can be gener-

alized to apply to the theory as a whole. With a carefully selected set of basis and weighting functions, consistent higher order solutions (represented here by $N \geq 3$) are equivalent to the closed form solution to the extent that there is not a practical difference between the two. This is why a MoM algorithm can be deemed to accurately solve problems regarding electromagnetic radiation even when a closed form solution cannot be reached due to the practical limitations on the order of the subspace defined by the basis functions.

3.4 Theory of Characteristic Modes

The theory of characteristic modes was first described as an explanation for scattering behaviors in the generally described resonance region. In this frequency range, between the low frequency Rayleigh region and the high frequency geometrical optics region, there was no consistent mathematical explanation for the scattering of electrical fields. Garbacz was the first to theorize that there existed a set of orthogonal modal currents that, when weighted by their respective radiation resistances, would linearly combine to represent the current distribution on a metal scatterer [43]. He further posited that these modes existed for arbitrary shapes defined by nonseparable coordinate systems that would be dependent on the shape of the scattering object. Together with Turpin, Garbacz showed that these modes could be calculated by diagonalization of the scattering matrix [44]. Though this process, Garbacz was able to characterize several different wire body scatterers including circular and elliptic loops. However, the diagonalization of the scattering matrix was too specific of a process to perform modal calculations of arbitrary bodies. Harrington approached the problem from a different perspective and successfully generalized the theory for all applications by diagonalizing the impedance matrix.

It is this formulation of characteristic modal analysis that will be presented in this thesis.

Harrington's derivation begins with the definition of the linear relationship between the tangential component of an electric field, E^i, impressed on a metallic object and the surface charge movement, J, created in response to this field. These two components are related by the linear operator L defined below:

$$\left[L(J) - E^i\right]_{tan} = 0. \tag{3.30}$$

Because L is a linear operator relating an electric potential to a current, it can be seen through Ohm's Law, $V = IR$, that L is a measure of impedance. Therefore it is possible to define a new operator Z such that

$$Z(J) = \left[L(J)\right]_{tan}. \tag{3.31}$$

Z is a symmetric operator separable into real Hermitian parts:

$$R = \frac{1}{2}(Z + Z^*) \tag{3.32}$$

$$X = \frac{1}{2j}(Z - Z^*). \tag{3.33}$$

With this definition, $Z = R + jX$.

Once the first set of linear operators is defined as shown above, the next step in Harrington's derivation begins with the formulation of an eigenvalue equation

$$Z(J_n) = v_n M(J_n). \tag{3.34}$$

The matrix M can be arbitrarily defined in this relationship. However, by choosing M such that $M = R$, the matrix Z is diagonalized and the radiation patterns are orthogonal [36]. Next, defining the complex eigenvalue v_n as

$$v_n = 1 + j\lambda_n \tag{3.35}$$

allows for the simplification of 3.34 into

$$X(J_n) = \lambda_n R(J_n). \tag{3.36}$$

This leads to the result that the eigenfunctions J_n and the eigenvalues λ_n are real. Since the eigenfunctions are real and they are defined by the orthogonal relationships

$$\begin{aligned} \langle J_m, RJ_n \rangle &= 0 \\ \langle J_m, XJ_n \rangle &= 0 \\ \langle J_m, ZJ_n \rangle &= 0 \end{aligned} \tag{3.37}$$

where $m \neq n$, the inner products also maintain the same orthogonality such that

$$\begin{aligned} \langle J_m^*, RJ_n \rangle &= 0 \\ \langle J_m^*, XJ_n \rangle &= 0 \\ \langle J_m^*, ZJ_n \rangle &= 0. \end{aligned} \tag{3.38}$$

These definitions lead to the diagonalization of the impedance matrix Z.

This diagonalization is the single most important aspect of the derivation. As can be seen in Equation 3.18, the MoM can only be solved when the inverse of

the linear map L can be calculated. For many practical applications, this matrix is infinite in extent. Since the efficient computation of the inverse of a matrix involves solving for the determinant of that matrix, which in this case is infinite, this process is not possible. However, for a diagonal matrix the inverse is found by simply taking the reciprocal of each value along the diagonal. Since typically only the first few modes are significant, this process reduces to finding the reciprocal of enough modes such that the original function is effectively approximated.

Continuing with Harrington's derivation, once the matrices are defined as diagonal operators on this functional basis, it is possible to normalize the radiated power, calculated as

$$\langle J_n^*, RJ_n \rangle = 1, \tag{3.39}$$

such that the the previous orthagonality relationships can be generalized as

$$\begin{aligned} \langle J_m, RJ_n \rangle &= \langle J_m^*, RJ_n \rangle = \delta_{mn} \\ \langle J_m, XJ_n \rangle &= \langle J_m^*, XJ_n \rangle = \lambda_n \delta_{mn} \\ \langle J_m, ZJ_n \rangle &= \langle J_m^*, ZJ_n \rangle = (1 + j\lambda_n)\delta_{mn} \end{aligned} \tag{3.40}$$

where δ_{mn} is the Kronecker delta.

With the definitions complete, the modal solution can now be quickly derived using the MoM. To start, the surface current on the object J can be approximated as a linear summation of eigencurrents such that

$$J = \sum_n \alpha_n J_n. \tag{3.41}$$

Equation 3.30 then becomes

$$\sum_n \alpha_n Z J_n - E^i = 0. \tag{3.42}$$

Using the Galkerin method, the weighting functions are defined as J_m. Taking the inner product of Equation 3.42 with the weighting functions results in the equation

$$\sum_n \alpha_n \langle J_m, Z J_n \rangle = \langle J_m, E^i \rangle. \tag{3.43}$$

By substitution with Equation 3.40, Equation 3.43 reduces to

$$\alpha_n (1 + j\lambda_n) = \langle J_n, E^i \rangle. \tag{3.44}$$

Solving for α_n converts Equation 3.41 to

$$J = \sum_n \frac{V_n^i J_n}{1 + j\lambda_n} \tag{3.45}$$

where V_n^i is known as the modal excitation coefficient and is defined as

$$V_n^i = \langle J_n, E^i \rangle = \oiint_S J_n \cdot E^i ds \tag{3.46}$$

[36]. The electric fields are linearly related to the currents and can be described as

$$E = \sum_n \frac{V_n^i E_n}{1 + j\lambda_n}. \tag{3.47}$$

The important thing to note is that since the modes are sorted by radiation resistance [43], the values of λ_n increase with n such that there is less real radiated power and more complex stored energy with higher order modes. Furthermore, the

modal excitation coefficient V_n^i is the practical way that an individual can influence the resulting modal decomposition through source excitation. With this in mind, the overall radiation pattern created by an antenna designed with CMA is a weighted combination of existing modes where the modes are intrinsic to the structure and are defined by λ_n and the weights are defined by source excitation and can be incorporated into V_n^i. Using this technique, it is possible to quickly characterize the potential performance of a metallic object as a radiating structure, and then design a feed network to excite the desired radiation pattern.

3.5 Chapter Summary

To design an antenna for a metallic SUAS (or a quadcopter utilizing a metallic ground plane to shield the internal components), CMA is an efficient and effective way to intrinsically understand the radiation characteristics of the metal object and design a suitable antenna utilizing the structure. In this section, the mathematical basis for the antenna synthesis defined in this thesis was shown and explained. The initial derivation of MoM and the boundary value problem that followed gave practical insight into the fundamental math underlying CMA. The derivation of CMA was then given to explain the forthcoming antenna synthesis procedure.

Chapter 4

Antenna Synthesis

4.1 Introduction

The initial design for the antenna began with the generation of an aerodynamic base plate by a graduate student in the Center for Autonomous Sensing and Sampling (CASS) for the quadcopter. The quadcopter used for this project can be seen in Figure 4.1. The base plate for the quadcopter will be 3-D printed and plated with copper to provide a lightweight ground plane that will serve as a metallic boundary to eliminate the majority of the coupling and loading effects caused by the proximity of the radiating element to the densely packed internal components. In the end, this boundary should prevent the placement sensitivity and pattern degradation seen previously in Figure 2.8 when the radiating element is measured in situ. Once the ground plane was designed, the first step in the antenna synthesis was to model the ground plane in FEKO to perform CMA. After the structure is analyzed, one mode was selected as a basis for a proposed radiation pattern based on its radiation performance. The first attempt to couple into the primary modes of the craft are described in the subsequent section. This endeavor proved to be unsuccessful, and led to a reimagined design of the radiating element. The final design of the antenna was based around an inverted F antenna (IFA), and the simulated design

and measurements of this model are presented in this chapter.

Figure 4.1: The quadcopter SUAS used as the basis for this design.

4.2 Ground Plane Analysis

Before the antenna synthesis process could truly begin, the aerodynamic bottom plate of the SUAS had to first be created. The finalized ground plane for this project is shown in Figure 4.2. This base plate was designed to be conformally attached to the quadcopter while allowing for airflow through the quadcopter's forward facing vent and for the later addition of signal lights for night flights. The conformal application of the depicted in Figure 4.3. Once a copper coating is applied to the 3D printed base plate, it will become an effective ground plane to aid in the antenna performance as discussed above.

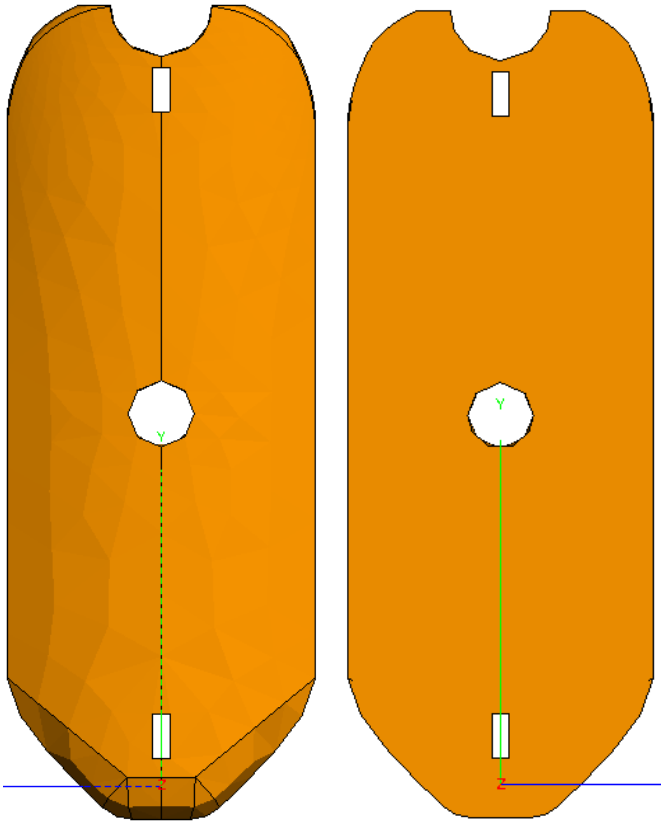

Figure 4.2: The ground plane design. The aerodynamically curved bottom side of the ground plane is shown on the left. The flat top side of the ground plane that will connect to the SUAS is shown on the right.

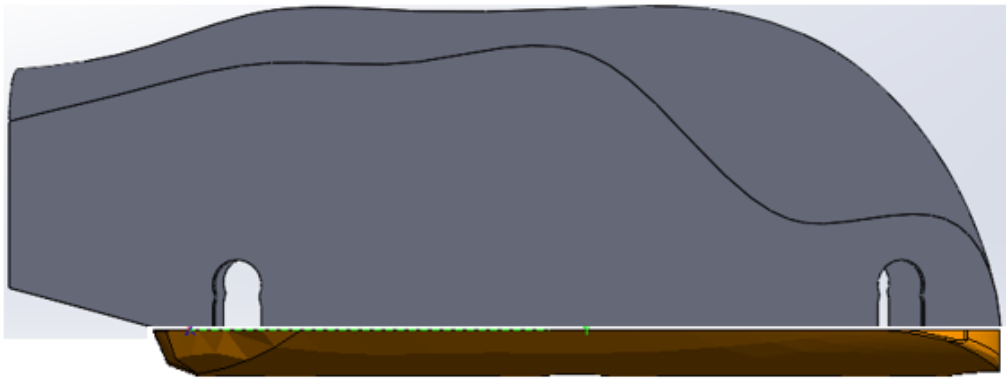

Figure 4.3: A rendering of the conformal application of the ground plane to the existing quadcopter shell.

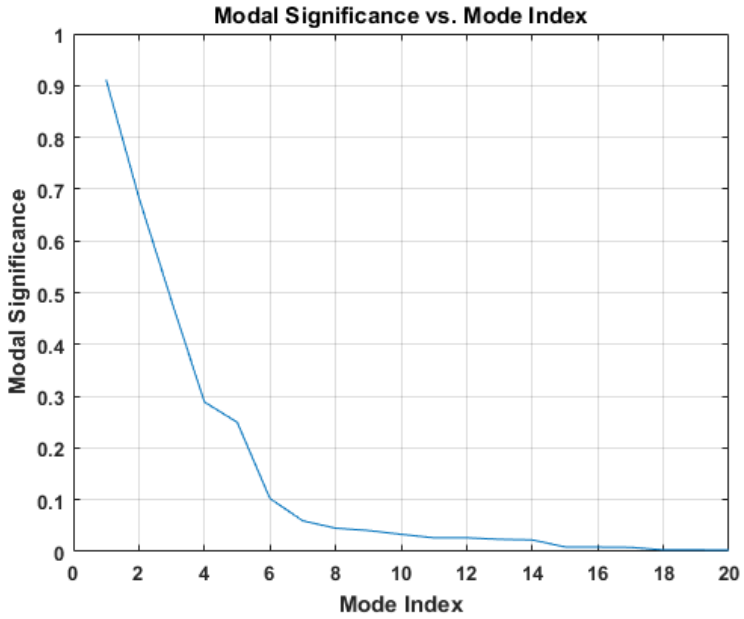

Figure 4.4: The decreasing modal significance of the first twenty modes of the SUAS ground plane.

Once the ground plane was designed, the model was then imported into FEKO and analyzed. The first twenty characteristic modes of the ground plane were calculated and the respective modal significance is shown in Figure 4.4. In this analysis, the modal significance is defined by

$$MS = \left| \frac{1}{1 + j\lambda_n} \right| \tag{4.1}$$

[23]. Although twenty modes were solved for, only the first six could be directly coupled into, as any mode with a modal significance of lower than 0.1 contains too much stored energy for efficient radiation [23]. The reason for this relationship between modal significance and stored energy can be attributed to Equation 3.47 and Figure 4.5. Figure 4.5 shows that eigenvalue magnitude increases with the modal index. As is shown in Equation 3.47, the larger eigenvalue means that the com-

plex portion of the normalized electric field magnitude is also higher. Therefore, the higher-order modes should not be excited because they have significantly more stored energy than the first six.

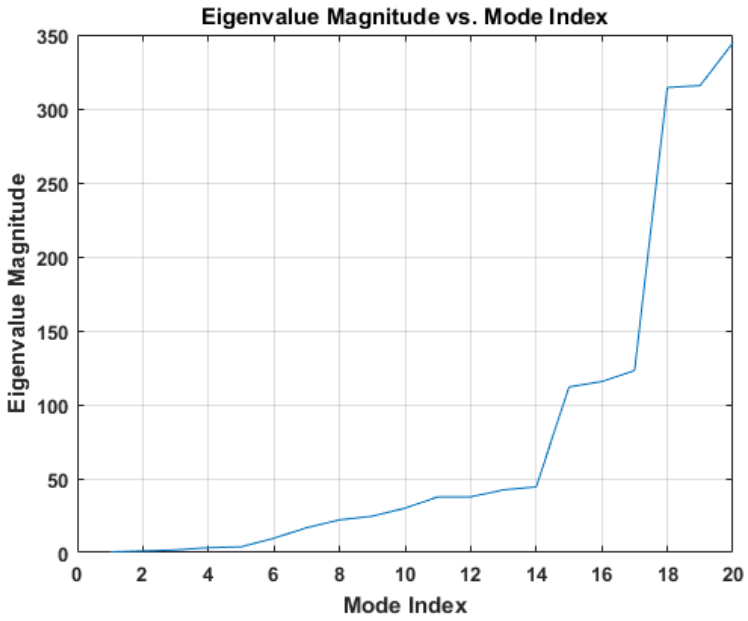

Figure 4.5: The progressive increase in eigenvalue magnitude as the modal index increases

With the search now limited to the first six characteristic modes of the ground plane, these modes can now be evaluated more closely to see if any of them match the desired radiation pattern. These six modes are shown for quick comparison in Figure 4.6. For modes with a desirable radiation pattern, the surface current also should be described in terms of a standard antenna with a comparable nominal surface current distribution. This comparison aids not only in the understanding of the relationship between the surface current and the resulting radiation pattern but also gives insight into potential modal excitation techniques.

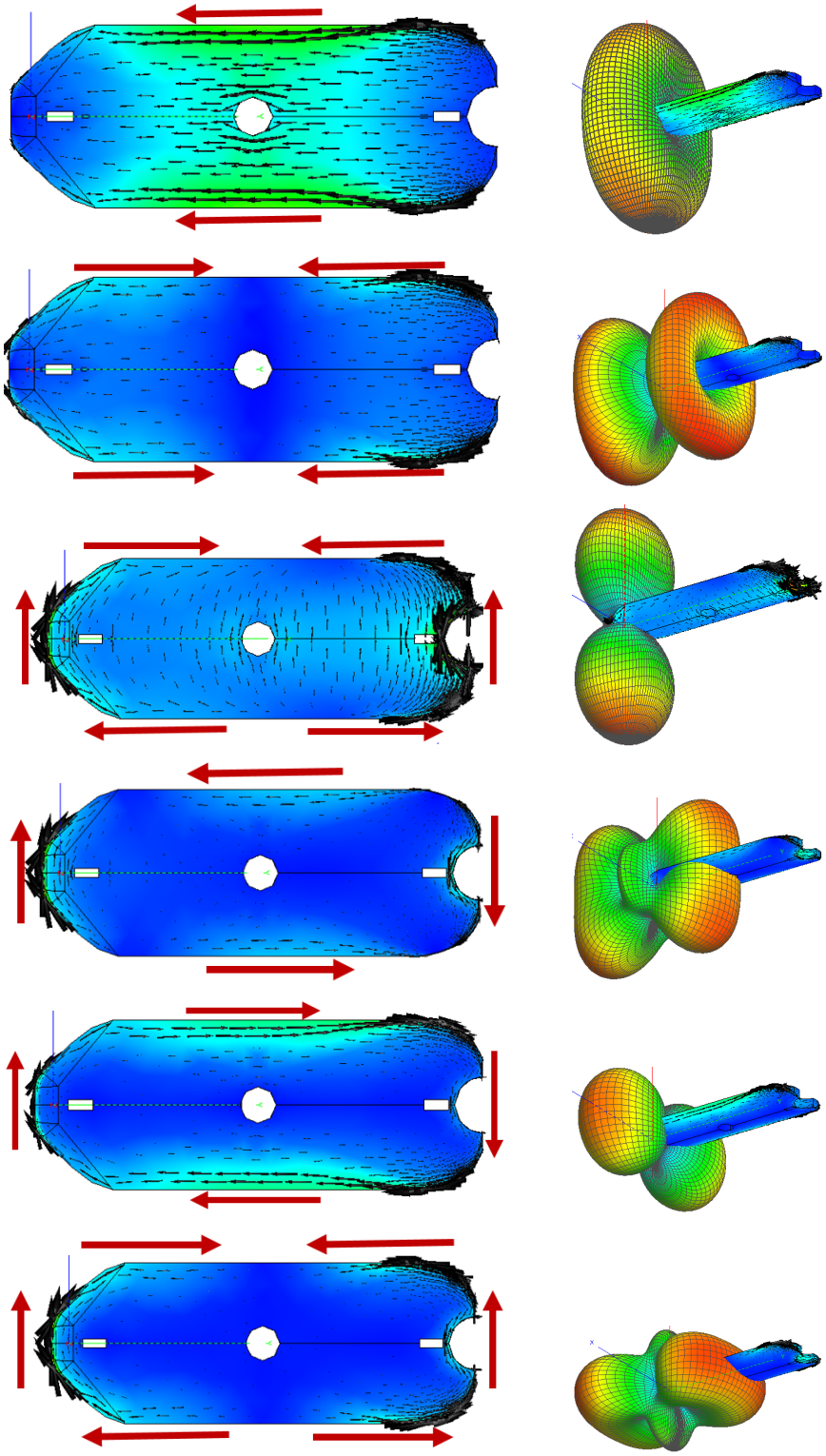

Figure 4.6: The first six characteristic modes presented in order starting with the first mode and ending with the sixth. The left column depicts the surface currents with red arrows depicting the direction of the edge currents. The right column shows the corresponding radiation pattern.

Beginning with the first mode, the current distribution is similar to that of a dipole antenna. The surface current flows linearly from the right side of the ground plane to the left with a current maximum located towards the center of the craft that tapers towards the respective termination points. The resulting radiation pattern is also similar to that of a dipole antenna, with an H-Plane radiation that appears nominally quasi-isotropic and a significant null along the central axis of the ground plane. Although this resulting radiation pattern is not ideal for long range flights because of the null, this is an acceptable starting point for the antenna design because it is quasi-isotropic in one plane and the null in the other plane could be filled by loosely coupling into a secondary mode. The only other mode that offers the potential for at least communication while primarily overhead is the third. The edge current distribution in this mode are similar to the current pattern around a resonant slot antenna with the current in the center of the craft flowing from the bottom of the page to the top of the page. The resulting radiation pattern has a greatly reduced field strength in the plane of the ground plane. Because of these nulls, this mode is less than ideal for long range communication and should not be singularly excited. The other four modes are not individually suitable for this application because they all have nulls in their radiation pattern directly below the bottom of the ground plane that would hamper overhead communication. After the completion of this modal analysis, it was apparent that the only mode with both a high enough modal significance to radiate efficiently and a desirable radiation pattern was in fact the first mode.

4.3 The First Characteristic Mode

After the first mode was selected, further analysis was done to analyze the ground current and the resulting radiation pattern. Figure 4.7 shows the ground current on both the top and bottom side of the ground plane. The current flows from the top of the page to the bottom of the page on both sides of the ground plane and the current magnitude distribution appears to be relatively equivalent on both sides with slightly more current flowing on the craft's bottom. Figure 4.8 depicts the normalized radiated field strength in both the H-Plane and the E-Plane. Because the ground current distribution actually most closely represents two narrowly spaced dipole antennas that are strongly coupled, the resulting H-Plane magnitude is more directive than the quasi-isotropic performance that is expected of a nominal dipole radiation pattern. This can be explained by an effective array factor scaling of the H-Plane radiation caused by the closely located dipoles. As expected, the E-Plane has a strong null along the central axis of the ground plane. Overall, the eigencurrent of this mode appears relatively straightforward and the radiation pattern is acceptable as a starting point for the antenna design.

The next step in the antenna synthesis process is to excite the desired mode. Previous work has shown that an impedance matched patch antenna with a meander line to enforce current circulation can be used to excite a loop of current along the edge of a square ground plane [23]. Using a similar approach, the goal for this design will be to create a U-shaped patch antenna with a feed along the symmetry plane of the patch. A planar example of this patch design is shown below in Figure 4.9. The symmetric feed point for this patch is critical to the design. An offset feed would cause a different phasing for what is essentially two separate but strongly coupled elements. This phase offset would in effect be a linear phase shift

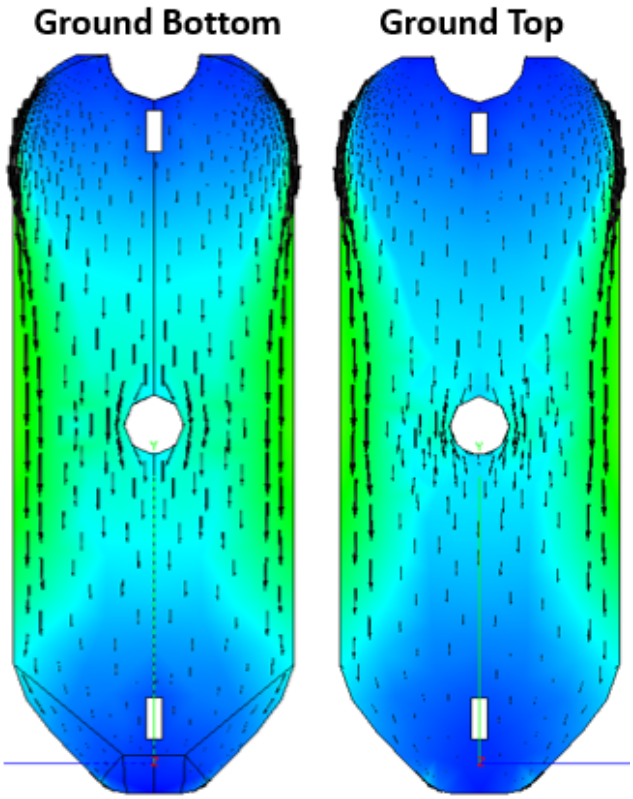

Figure 4.7: The current distribution of the first mode

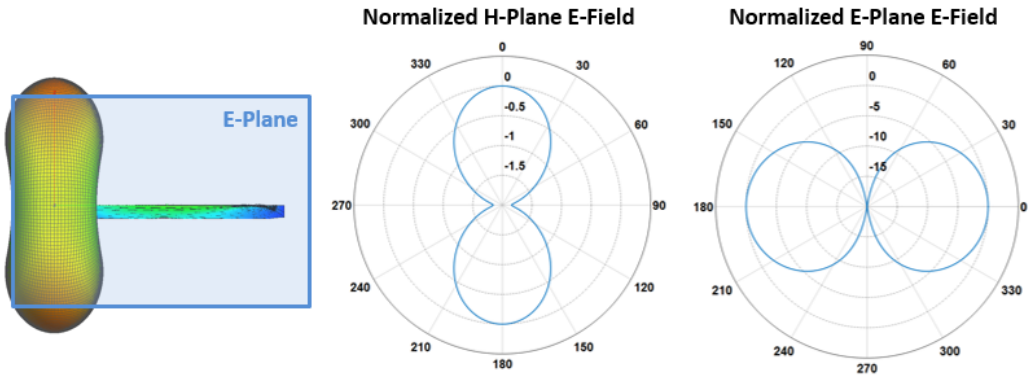

Figure 4.8: The far left plot shows the orientation of the E-Plane of the radiation pattern, with the craft for reference. The other two plots show the normalized radiation pattern measured in dB for both the E-plane and the H-plane.

applied to a two element array and could cause unintentional beamsteering in the H-Plane shown in Figure 4.8. After the dimensions of the patch are determined to

maximize the return loss at the operating frequency of 915 MHz, the patch will be conformally applied to the bottom of the ground plane. When correctly placed, the arms of the patch will excite a linear current distribution on the ground plane like what is seen in Figure 4.7. An additional advantage of this style of feed network is that, by exciting the first mode's currents only on the bottom of the ground plane, the magnitude of the radiation pattern in the upper hemisphere of the design would be weaker than that of the lower hemisphere. This would significantly decrease the coupling between the ground plane and the craft internals.

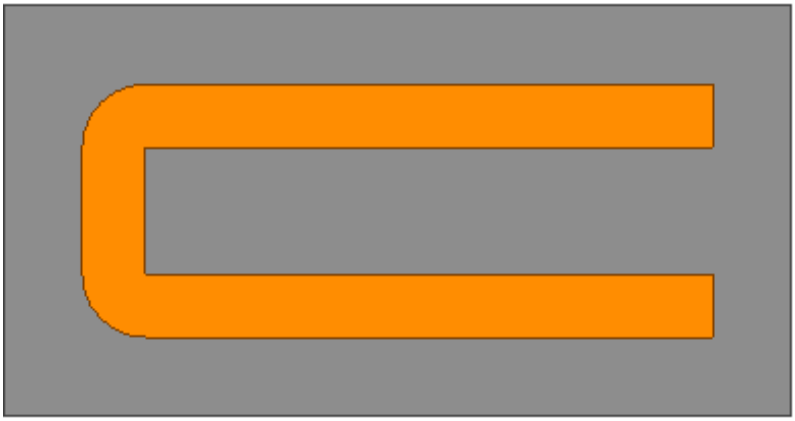

Figure 4.9: Planar U-shaped patch

With the fundamental feed network design decided upon, the next step was to use HFSS [45] to determine the physical dimensions of the planar U-shaped patch. Figure 4.10 shows the simulated return loss of the initial design. Although the design is too narrowband for the radio currently utilized by CASS, which operates from 902 MHz to 928 MHz, the resulting patch has a return loss of 15 dB at 915 MHz. This indicates an impedance match that is good enough to test the underlying design of the patch antenna.

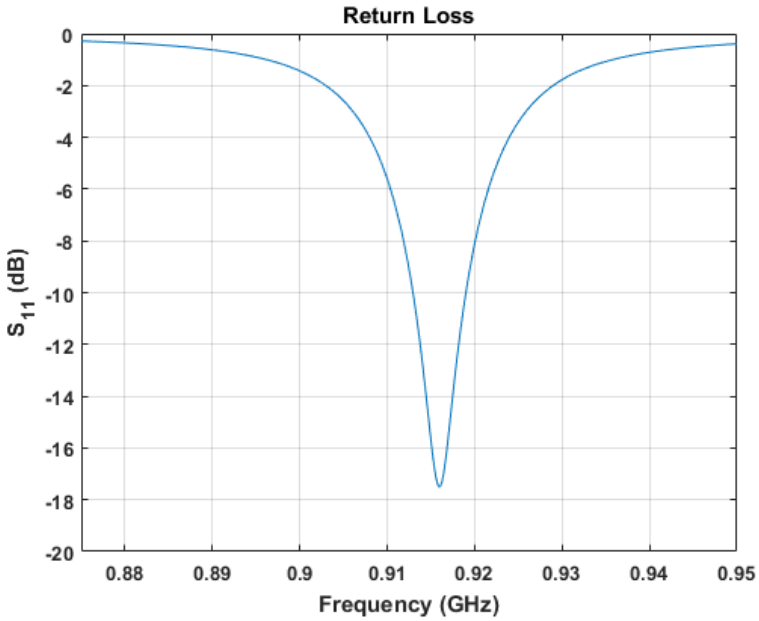

Figure 4.10: Return loss of the planar U-shaped patch

The next step was to analyze the structure in FEKO to make sure that the presented design was feasible. The planar patch designed in the previous section was conformally projected onto the ground plane and then exported onto FEKO for analysis. The eigenvalues of this structure can be seen in Figure 4.11. From the graph it is clear to see that only the first four modes could potentially be excited [23]. The surface current magnitude and current direction for these four modes is shown in Figure 4.12. The first mode has the correct current direction, with the current on both arms of the patch running from the bottom of the page to the top of the page. Furthermore, the surface current density of this mode has a maximum at the center of the arms' outer length. This is the ideal current distribution and density for coupling into the first mode of the ground plane shown in Figure 4.7. It mimics both the magnitude and direction of the desired current. However, it has a very weak surface current density along the symmetry axis of the patch, which had been previously selected as the patch's feed point. This is a problem because the

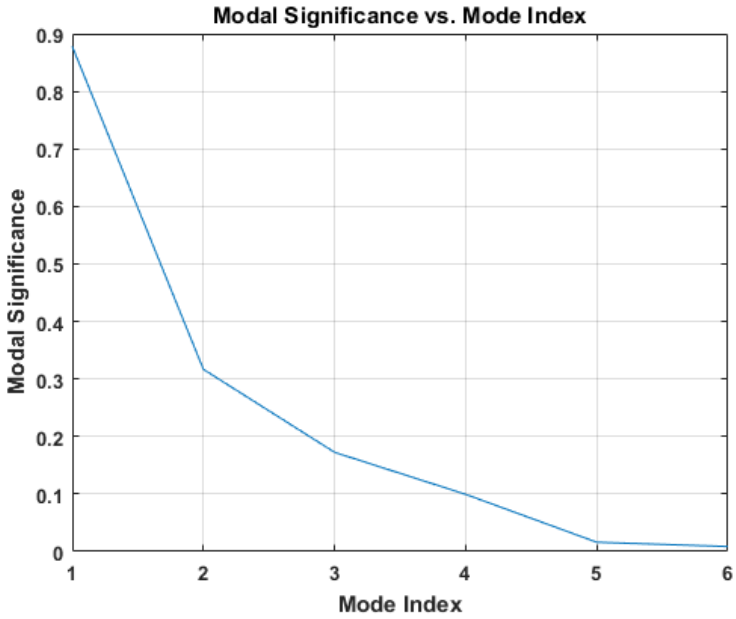

Figure 4.11: The modal significance of the first six modes of the U-shaped patch antenna.

current probe used to excite the first mode on the U-shaped patch should be located in a current maximum of the mode [23]. The second mode has a perfect surface current density for a symmetric excitation. The maximum of this mode lies directly on the symmetry axis. However, the surface current direction on either arm is 180 degrees out of phase with the other. Because of the coupling described previously, this would at best cause unintentional beamstearing and at worst would cause severe current cancellation because of the strong coupling between the two elements. The third and fourth mode had lower modal significance than the second mode and a lower surface current density on the axis of symmetry. Therefore, these modes would have been too weakly excited to be concerned with the non-ideal current distribution on the arms of the patch.

In the end, the first mode of the ground plane was nearly ideal for the purposes of this research. Furthermore, the U-shaped patch's first mode had a very good

surface current distribution and density to allow for direct coupling into the ground plane's first mode. Exciting currents solely on the bottom of the craft would only improve upon the efficacy of air-to-ground communication by increasing the field magnitude in the lower hemisphere of the craft's radiation. However, this mode was impossible to excite properly because a modal analysis on the patch itself shows that there is a current density minimum along the symmetry plane for the first mode of the patch antenna. Instead, any mode that could be strongly excited with a feed on the symmetry plane of the antenna had the wrong surface current direction on the arms of the patch antenna to correctly couple into the first mode of the ground plane. Because of this, the standard U-shaped patch was not a potential design option.

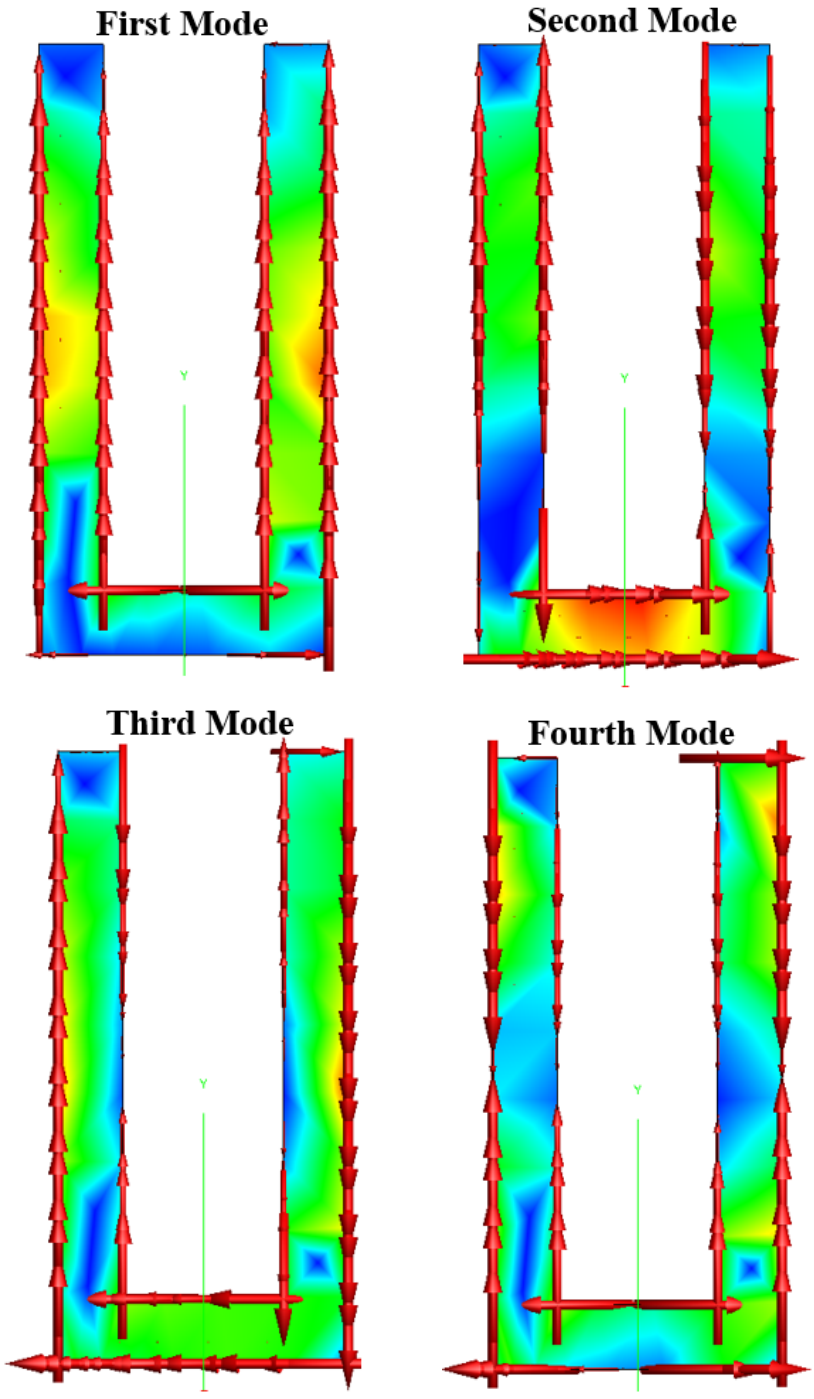

Figure 4.12: The first four characteristic modes. The surface current magnitude is displayed as a heat map with the direction of the current shown on the edges with red arrows.

While the standard U-shaped was not suitable for use as a feed network, further research into the general design was necessary. Alteration of the design of the patch, by adding minimal changes such as selectively changing line widths or through the addition of meander lines, might permit symmetric excitation. The first attempted alteration was simply to reduce the line width of the bottom of the U-shaped patch with the idea that the a narrower section of the patch would inherently have a higher current density with the same applied voltage. The results of this can be seen in Figure 4.13. There is still clearly a surface current minimum on the axis of two symmetry planes. Two more designs shown in Figure 4.13 show that neither a vertically or horizontally oriented meander line is capable of maintaining the same surface current direction on the arms as the first mode shown in Figure 4.12 while also having a surface current maximum on the axis of symmetry.

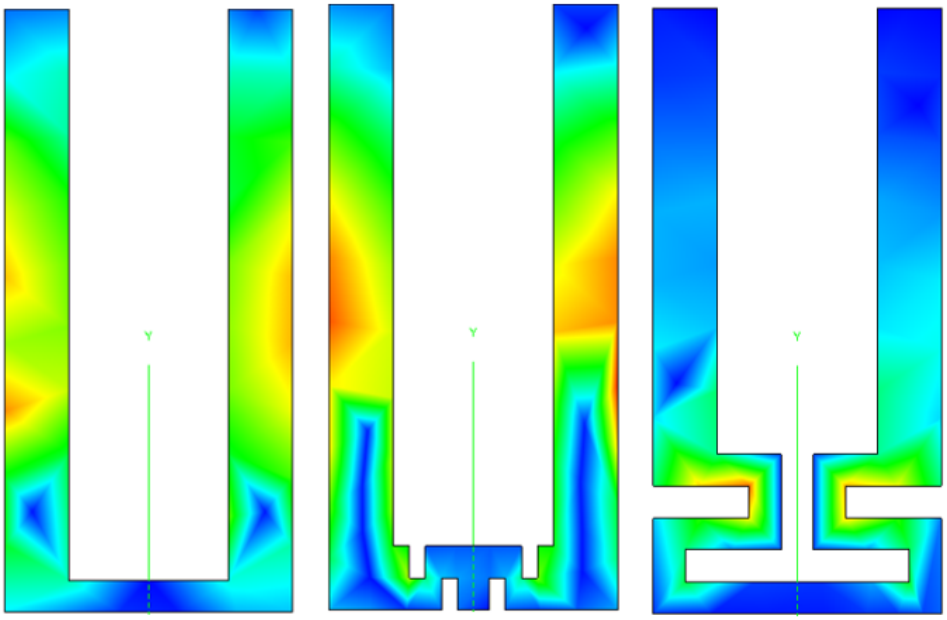

Figure 4.13: The current density of the first mode of variations on the U-shaped patch. The leftmost design features a smaller line width at the base of the patch. The central design has a vertically oriented meander at the base of the patch. The rightmost design features a horizontal meander at the base of the patch.

After the above attempts to correct the current density of the first mode of the U-shaped patch shown in Figure 4.12, it was determined that the generalized U-shaped patch simply was not a viable structure to couple into the first mode. Instead, further research will need to reanalyze the characteristic modes of the ground plane to find generalized insight into the characteristic radiation patterns of the ground plane and the corresponding currents required.

4.4 Reanalyzing the Characteristic Modes

Before revisiting the SUAS presented in this thesis, it is important to understand the generalized performance of CMA as a function of ground plane size. Starting with the models for electrically small antenna designs, it can be noted that the characteristic radiation performance of these shapes is described by a limited number of modes [23], [46]. In this case, the resulting radiation patterns of an excited structure are defined primarily by the structure. Inversely, the characteristic performance of an electrically large ground plane is defined not by the ground plane but rather the radiating element. This can be seen in the common design considerations and testing of monopole antennas. It is the intermediary definition of ground plane size though that is the focus of this research. In the zone characterized by an electrically medium ground plane, the impedance matrix and resulting modal characteristics of the ground plane with an attached antenna are not dominated by either the ground plane structure or by the chosen antenna. Instead, the impedance matrix is defined and dominated by a combination of characteristics from both the antenna and the ground plane. For this case, the best methodology for antenna synthesis is not necessarily the direct excitation of a significant mode from the original ground plane but rather an effective alteration of the original impedance matrix through the addi-

tion of a resonant element.

In reviewing the original modes significant enough for excitation from Figure 4.6, it can be seen that none of the six modes individually are enough to meet the stated design goals of quasi-isotropic performance in the lower hemisphere. So, instead of further trying to couple into one of the craft's fundamental modes of resonance, CMA was simply used as a starting point for this synthesis process. Once an intuitive understanding of the eigencurrents and resulting radiation patterns is achieved, it is possible to select a resonant antenna to provide the desired excitation. This effectively is a way to select an antenna's design and placement for operation on a deformed ground plane.

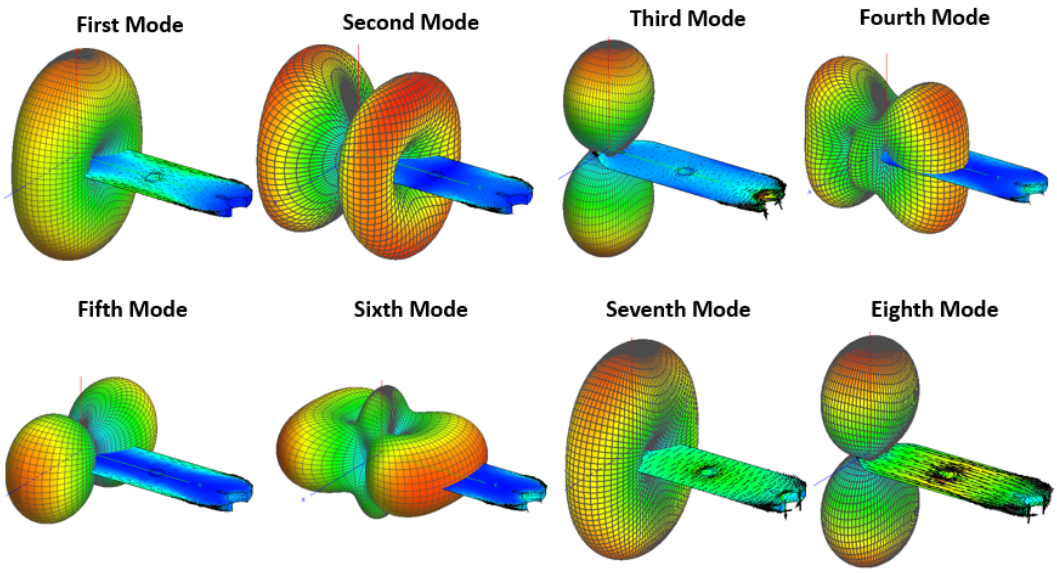

Figure 4.14: The E-Field pattern for the first eight ground plane modes superimposed on the ground plane.

Starting with the first modal resonance shown in Figure 4.7, it can be seen that fundamentally the current pattern that has the highest radiation resistance, and therefore the highest radiation efficiency, is a linear current distribution that runs parallel to the length of the craft. Because of this, the selected antenna should in-

duce a surface current that runs primarily along the center of the craft. The surface current distributions and resulting E-field patterns of the twenty modes originally solved for were then analyzed to find the next most significant mode with a linearly distributed current and a relatively desirable E-field. The first eight modes are displayed in Figure 4.14 because it was discovered that the eighth mode was the next to meet these conditions. The current distribution of this mode can be seen in greater detail in Figure 4.15, the direction of the current on the bottom of the craft is nearly identical to the first mode's current direction. However, the current magnitude is significantly different between the two. While the first mode has a relatively even current distribution with the current increasing close to the edges of the craft, in the eighth mode the current magnitude is distinctly concentrated at the center of the craft. The result of this difference is that the radiation pattern of the eighth mode, shown in Figure 4.16, is much more directive than the radiation pattern of the first mode, shown in Figure 4.8. Since the goal of this project is to create a semi-directive antenna, the current excited by the antenna should be centrally concentrated on the bottom of the ground plane in order to have the best air-to-ground communication link. However, to prevent poor radiation in the plane of the ground plane, there is a limit to the desired concentration of the current. Some current diffusion towards the edges of the plane is necessary for the design's performance. This can be seen in the comparing the edge current magnitude in the first mode to the eighth and the resulting far-field pattern in the plane of the ground. In the end, the ideal current distribution for this ground plane is one with a primarily linear current concentrated on the bottom of the ground plane with some current diffusion towards the edges.

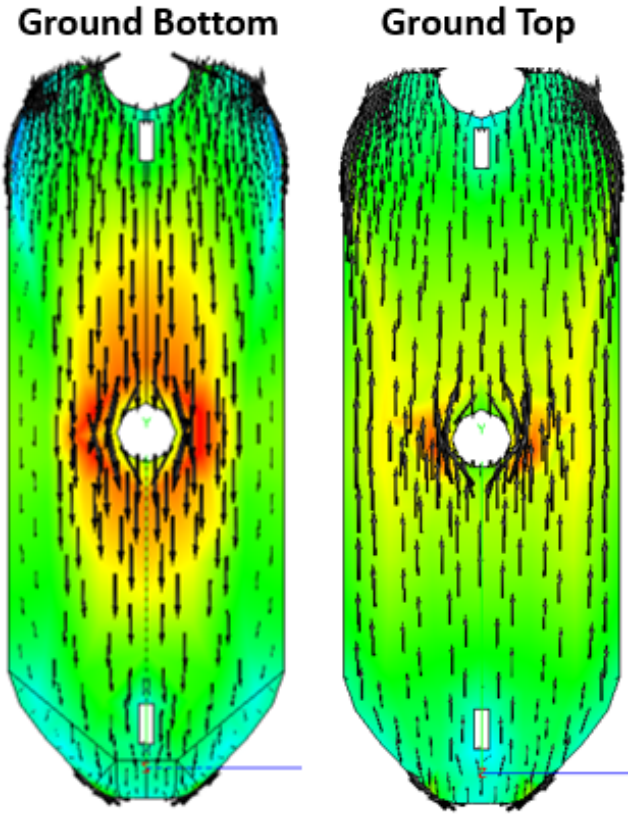

Figure 4.15: The current distribution of the eighth mode

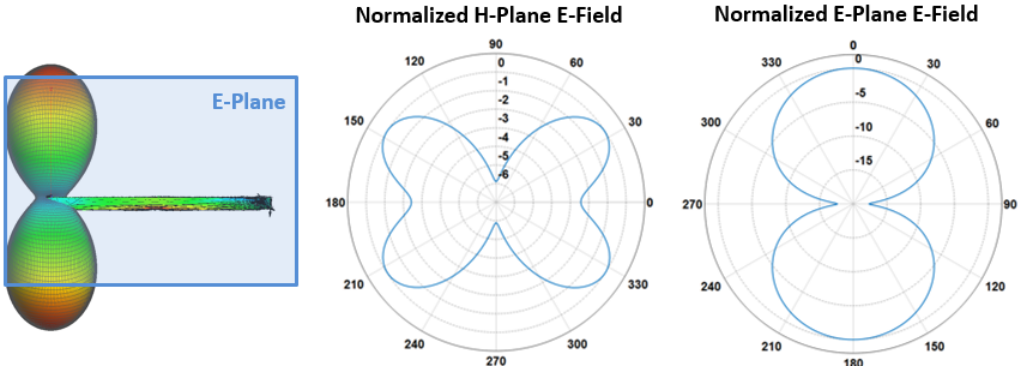

Figure 4.16: The far left plot shows the orientation of the E-Plane of the radiation pattern, with the craft for reference. The other two plots show the normalized radiation pattern measured in dB for both the E-plane and the H-plane.

4.5 The Inverted F Antenna

After establishing the ideal current distribution for the ground plane, a review of characterized antenna models showed that the inverted F antenna (IFA) was a potential solution. A profile view of the IFA placed on an electrically large ground plane can be seen in Figure 4.17. The IFA is essentially a shorted wire monopole that can be modeled as half of a half-wavelength slot antenna. The main current path is between the feed point on the IFA and the shorted stub to the ground plane. The overall current pattern can be seen in Figure 4.18. From the vector length and orientation it is apparent that the current is concentrated towards the area directly underneath the antenna and is predominantly colinear to the IFA itself with some current diffusion towards the edges of the ground plane. This is a very close match to the desired ground plane current pattern. Furthermore, although the design is not strictly conformal, it has the same general profile of the pitot tubes used to measure airspeed on conventional aircraft and therefore is a relatively aerodynamic design.

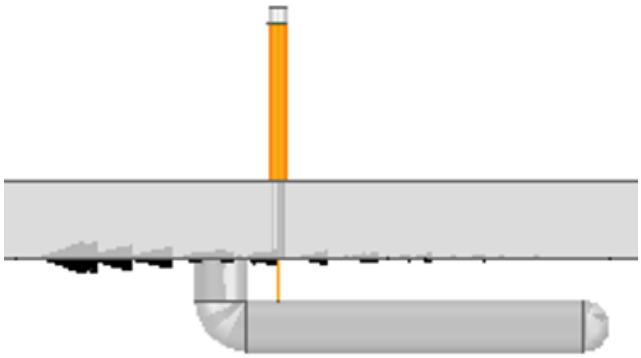

Figure 4.17: The side profile of the IFA excited by a semi-rigid coaxial probe feed on an electrically large ground plane.

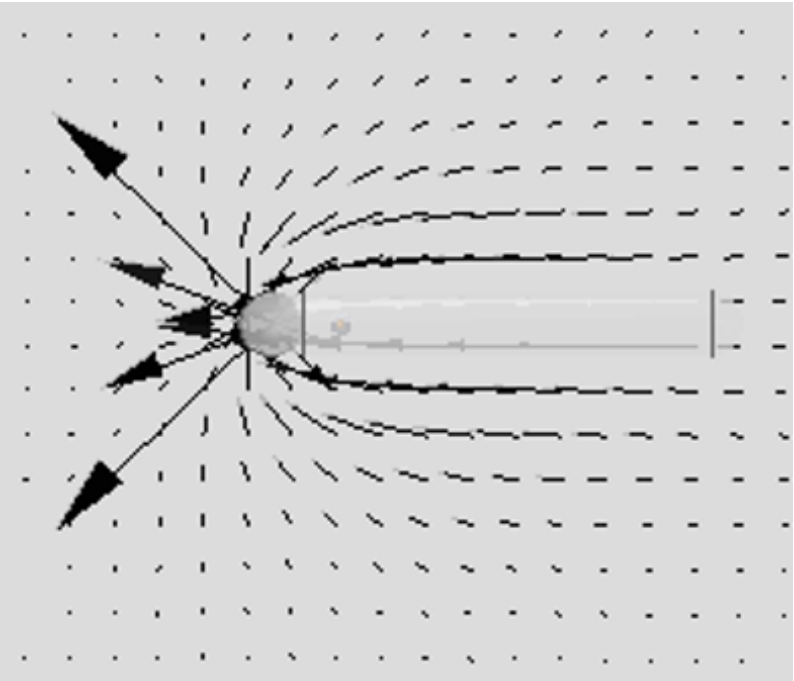

Figure 4.18: The vector current distribution of the IFA excited by a semi-rigid coaxial probe feed on an electrically large ground plane.

The design characteristics for the IFA are presented in [47], [48]. The bandwidth is determined by the wire radius, r, used in the design and the height, h, of the IFA above the ground plane. This is similar to how the bandwidth of a monopole antenna gets larger as the radial dimension increases because the number of potential current pathways rises. Likewise, the effects of alterations on the height of the IFA on the bandwidth of its performance can be understood through the lens of slot antenna theory. Just as increasing the width of a resonant slot antenna makes the bandwidth of its operation larger by allowing higher order modes to propagate, the IFA also increases in bandwidth as the height increases. The final design consideration for the IFA is the characteristic impedance of the structure. This impedance is primarily determined by the separation distance, d, between the feed point and the shorted stub. This is a clear extension of general circuit theory because that distance is

the fundamental shortest current pathway between the excitation and the ground plane and is therefore directly related to the element's impedance. The operating frequency of the antenna is determined by the element's length, L, in the same way that the operating frequency of a monopole is determined.

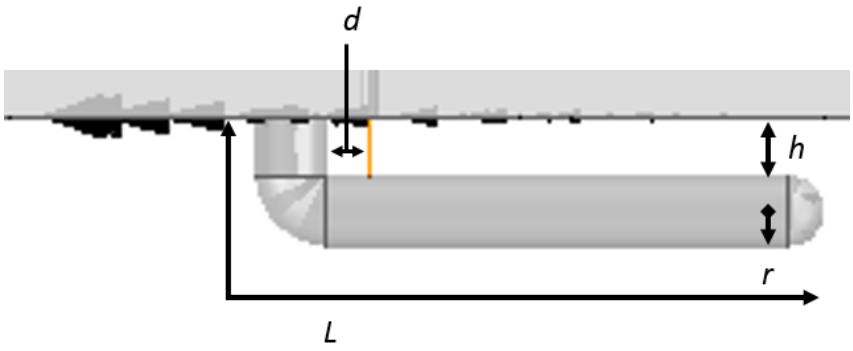

Figure 4.19: The design parameters for an IFA

4.6 Simulated Results

The first design consideration for the IFA was the placement of the resonant element. To concentrate the current distribution on the bottom of the ground plane, shown in Figure 4.2, the IFA must be placed on the bottom side of the ground plane. For the desired symmetric phase excitation along the length of the ground plane, the horizontal placement of the antenna can only be along the plane's central axis. The shorted stub of the IFA must either be placed on the front or the rear of the ground plane, with the element extending towards the craft's center. In this way, the linear current distribution will extend over the length of the craft while the holes in the ground plane will have relatively weaker current concentrations on them than what is seen in the eighth mode, shown in Figure 4.15. Because the radio module for the SUAS is on the front of the craft, the IFA shorted stub was placed on the front of the ground plane to minimize the cable length required to connect the antenna. This

IFA placement is shown below in Figure 4.20.

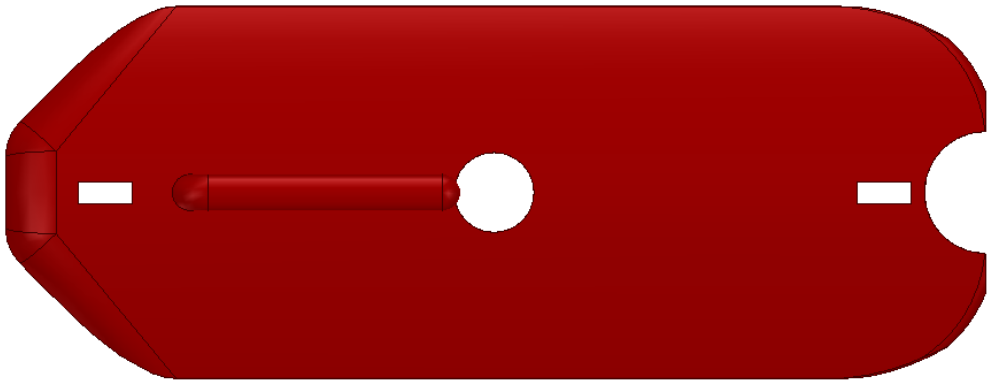

Figure 4.20: The placement of the IFA

Once the IFA placement was determined, the next step was to validate the current distribution on the craft.The resulting vector representation of the current distribution can be seen in Figure 4.21. The direction and relative magnitude of the current agrees closely with the desired current pattern. The surface current on the ground plane flows predominately parallel to the length of the craft. However, there is some lateral current diffusion towards the edges of the ground plane. The current magnitude is more clearly depicted in Figure 4.22. Once again, the current magnitude has strong agreement with the design goals. There is a strongly centralized current distribution directly underneath the IFA that does gradually spread towards the edges of the craft with little to no current on the top of the ground plane.

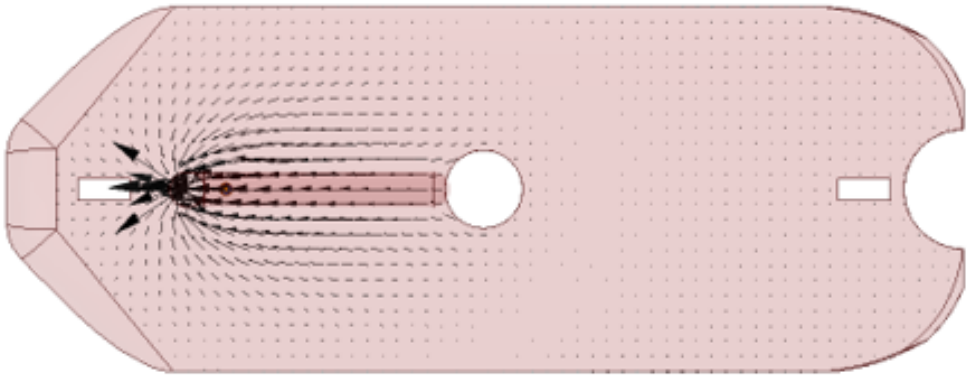

Figure 4.21: The current distribution on the ground plane caused by the IFA

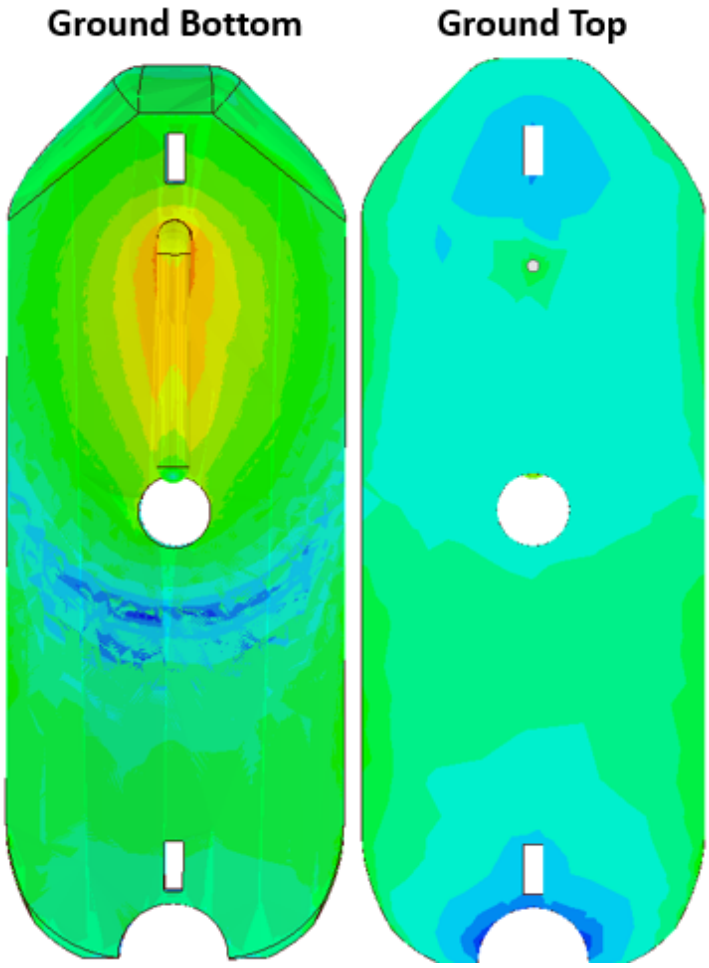

Figure 4.22: The current magnitude on either side of the ground plane caused by the IFA

Now that the ground plane current excited by the IFA has been confirmed to meet the design guidelines, the IFA design was optimized to meet the communication system requirements described previously. The final design has a minimum value of S_{11} of -29 dB at 914.5 MHz and a VSWR$\leq$2 bandwidth of roughly 30 MHz from 900 MHz to 930 MHz. This sufficiently covers the operating bandwidth of the radio used for the SUAS, which operates between 902 and 928 MHz, and has a peak return loss at the approximate center frequency of the radio. Figure 4.24 shows the imaginary impedance of this antenna over the same frequency range. There is a resonance at approximately 910 MHz with relatively small imaginary impedance in the band of operation for the radio. At 915 MHz, the antenna has an expected radiation efficiency above 0.98. The combined analysis of these graphs and the antenna's radiation efficiency verifies that the antenna will successfully radiate within the operating bandwidth of the radio system.

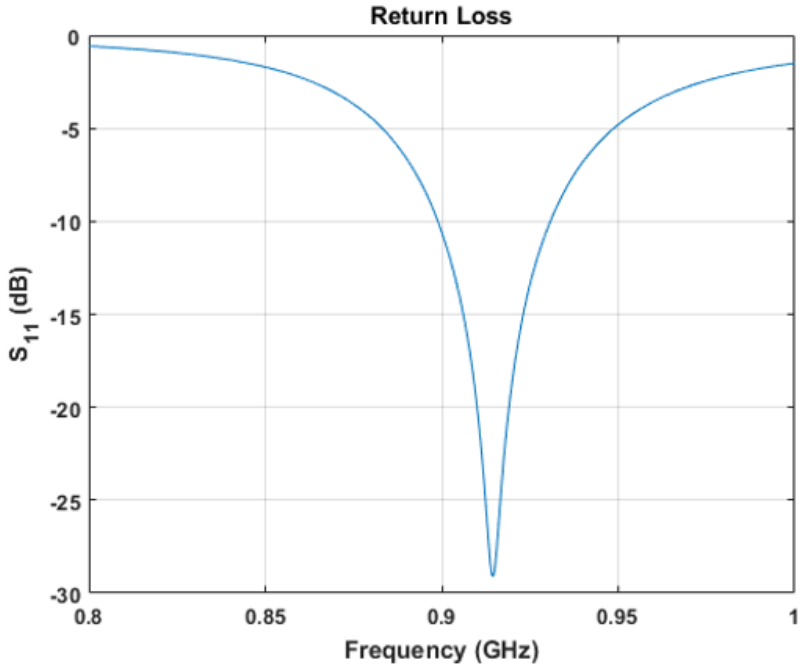

Figure 4.23: The Return loss of the IFA on the SUAS ground plane

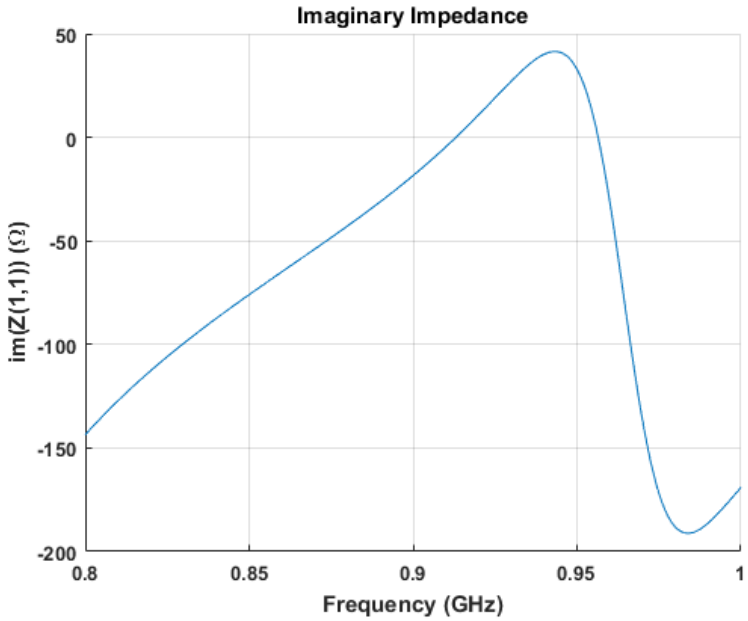

Figure 4.24: The imaginary impedance of the IFA on the SUAS ground plane

With the antenna now designed with a suitable broadband impedance match, the resulting radiation pattern can now be characterized. The realized gain of the antenna is first shown in Figure 4.25 with individual cut planes of the radiated field shown in Figure 4.26. The realized gain has a maximum of 4.1 dBi that occurs approximately at broadside, $\theta = -180°$ and a minimum of -2.83 dBi at $\theta = \phi = -90°$. This means that the antenna has full HPBW in comparison to an isotropic radiator in the lower hemisphere, meeting the design goals of the project. Furthermore, for much of the lower hemisphere the effective realized gain is higher than that of an isotropic radiator and thus will be highly effective in air-to-ground communication.

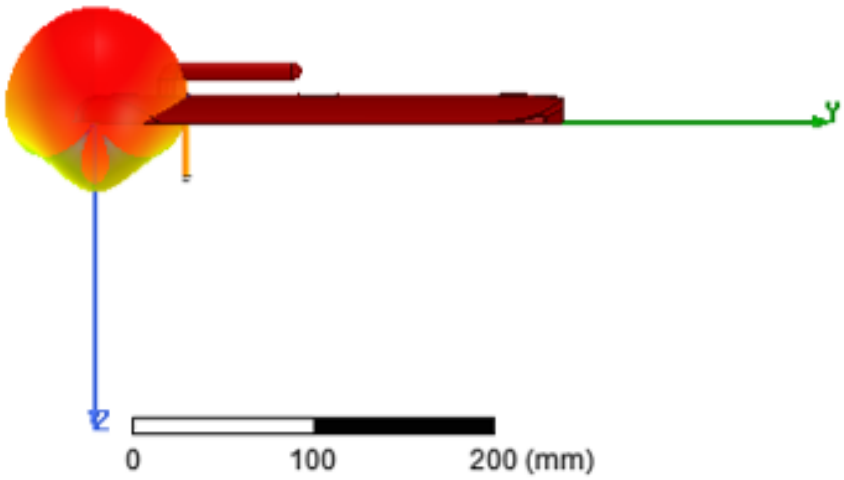

Figure 4.25: The realized gain of the IFA at 915 MHz superimposed on the ground plane for reference

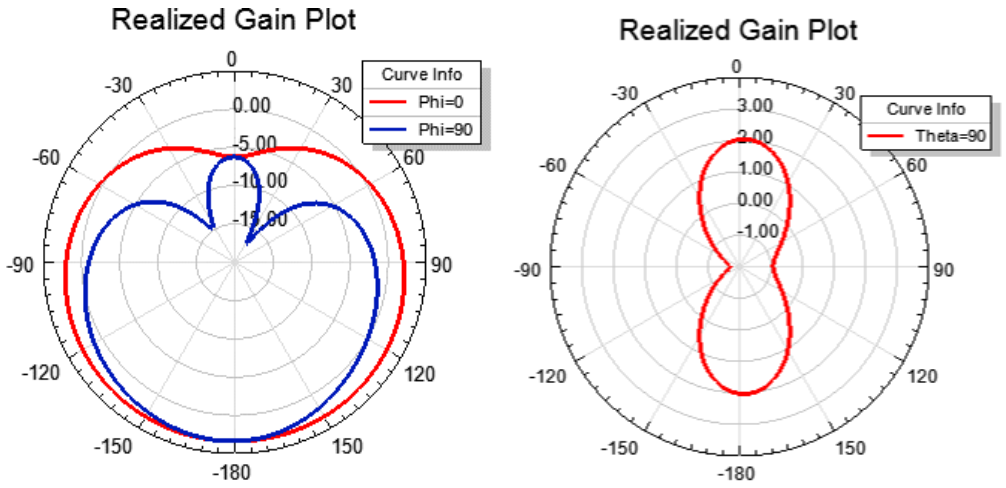

Figure 4.26: The realized gain of the IFA at 915 MHz shown in three different cutplanes

As a final analysis of the structure, a quick comparison of the performance of the IFA on the SUAS ground plane to the IFA performance on an electrically small and an electrically large ground plane is warranted. The resulting realized gain patterns for these structures is shown in Figure 4.27 and Figure 4.28. For these two figures, and the original IFA gain plot in Figure 4.25, the view plane is the same between the

three models and the IFA size, orientation, and feed structure are also identical. The performance of the IFA on a square ground plane that is roughly 8λ in side length is depicted in Figure 4.27. This radiation pattern is relatively constant in reference to ϕ, since the ground plane is much larger than the IFA extents. However the most significant divergence in pattern from that of the IFA on the SUAS ground plane is the fact that this gain pattern is significantly less directive with a maximum gain of only approximately 1.7 dBi and a greater proportion of radiated energy directed towards the side of the ground plane where the feed is located. The performance of the IFA on an electrically small ground plane, approximately λ in length but only about $\lambda/10$ in width, is shown in Figure 4.28. The realized gain of this antenna is relatively similar to that of a dipole pattern with the significant exception that there is a relative null around the $\theta = 0^{\circ}$ cut plane. Although this ground plane is roughly the same length as the SUAS ground plane, the IFA does not radiate in a comparable manner. When considering the realized gain of both the electrically large and electrically small ground plane, it is apparent that neither gain pattern is wholly similar to nor more desirable than that of the IFA on the SUAS ground plane. For this electrically medium ground plane, the use of CMA to select and place the antenna has resulted in a tailored solution to the original problem by taking into account both the effects of the deformed ground plane and the antenna itself.

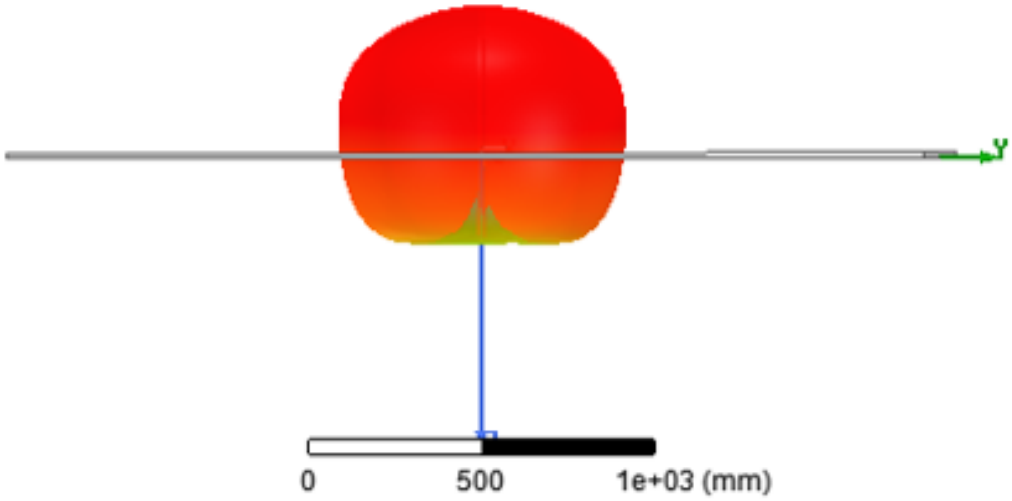

Figure 4.27: The realized gain of the IFA superimposed on the electrically large ground plane for reference

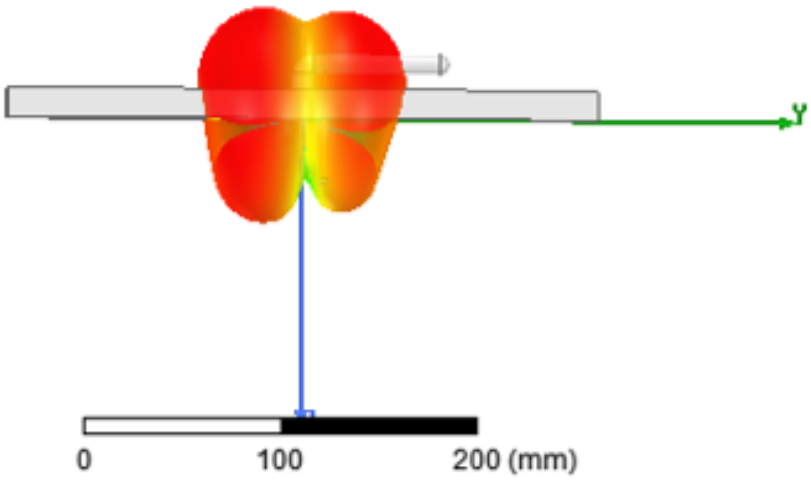

Figure 4.28: The realized gain of the IFA superimposed on the electrically small ground plane for reference

4.7 Modal Analysis of the IFA

With the IFA placement and size optimized through HFSS simulations, CMA was performed on the new structure to see how the addition of the IFA had altered the

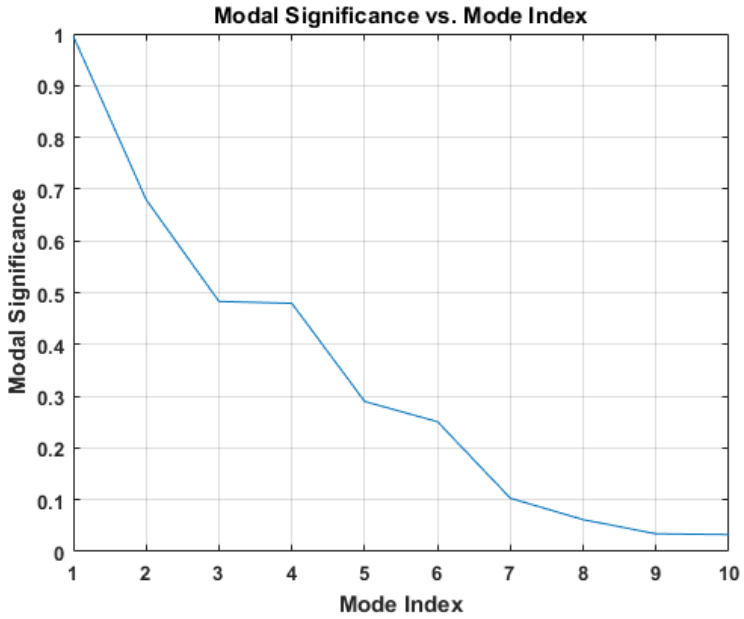

Figure 4.29: The modal significance of the ground plane with the resonant IFA attached

existing modality of the ground plane. This was done to verify that the addition of the resonant element significantly changed the ground plane and to provide greater context for its effects. The modal significance of the new structure can be seen in Figure 4.29. As discussed previously, only modes with a significance of at least 0.1 will radiate efficiently when excited [23]. With this in mind, the first seven modes of the IFA on the SUAS ground plane are significant enough to effect the final radiation pattern. This is one more significant mode than the ground plane without the IFA, shown in Figure 4.4.

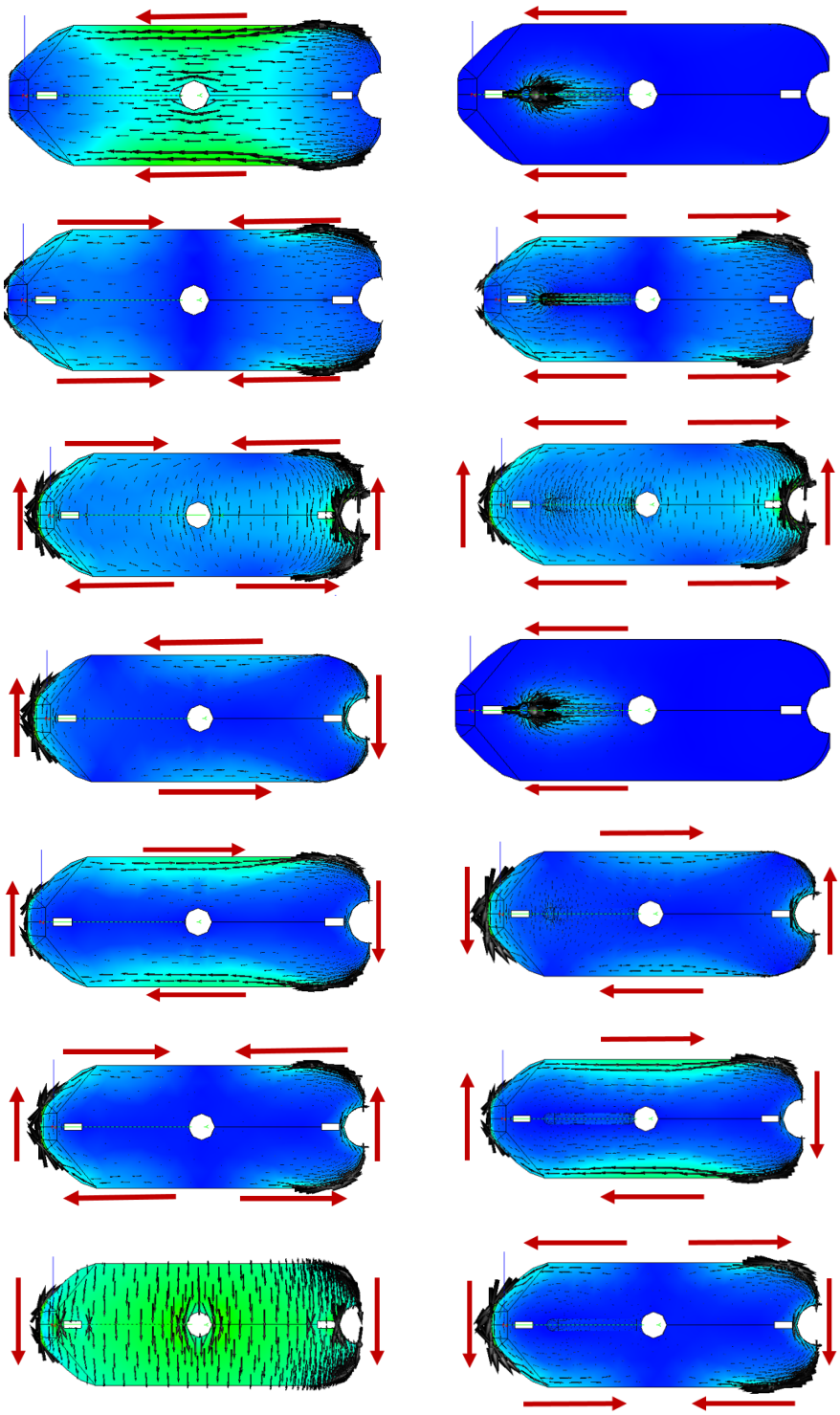

Figure 4.30: The current distribution of the first seven modes of the structure presented in decreasing order. The left column is just the SUAS ground plane while the right column is the ground plane with the IFA attached.

The current distribution of the first seven modes of the SUAS ground plane with and without the IFA are shown in Figure 4.30. The general current direction of the first three modes is the same, as is represented by the current arrows located on the outside of the craft. However, the first three modes with the IFA show a higher current density on/around the IFA than the current density that exists on the same area of the SUAS ground plane without the IFA. This is especially noticeable on the first two modes with the first mode in particular looking like a purely IFA based current distribution. This direct relationship between the modes changes with the fourth mode. The fourth mode of the ground plane with the IFA has a very similar current distribution to the first mode and also to the current pattern of the excited IFA antenna shown in Figure 4.21. Meanwhile, the current distribution of the fourth mode of the ground plane without the IFA appears to align with the fifth mode of the ground plane with the IFA. This pattern (where the current distribution of the n^{th} mode of the ground plane with the IFA aligns with the $n-1$ mode of just the ground plane) continues for the rest of the significant modes. When this pattern is analyzed in conjunction with the fact that the addition of the IFA to the ground plane increased the number of significant modes by one, it seems apparent that the fourth mode of the ground plane with the IFA attached is primarily caused by the resonant structure while the rest of the modes are primarily influenced by, and retained from, the model of just the SUAS ground plane.

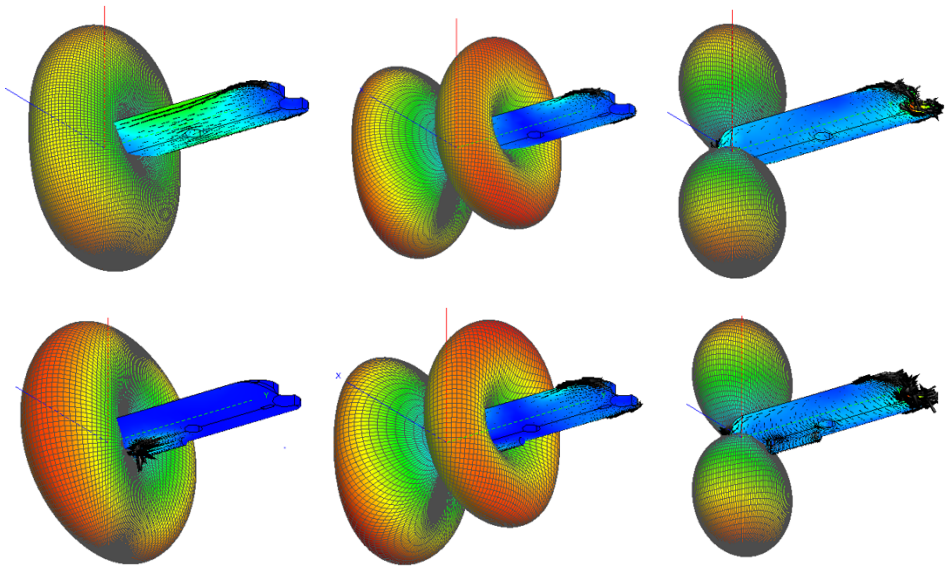

Figure 4.31: The radiation patterns of the first three modes of the structure presented in decreasing order from left to right. The top row is just the SUAS ground plane while the bottom column is the ground plane with the IFA attached.

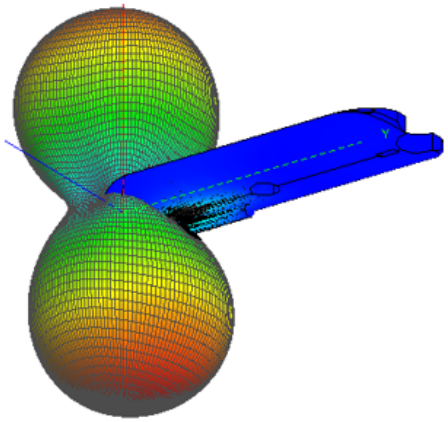

Figure 4.32: The radiation pattern of the fourth mode of the SUAS ground plane with an attached IFA.

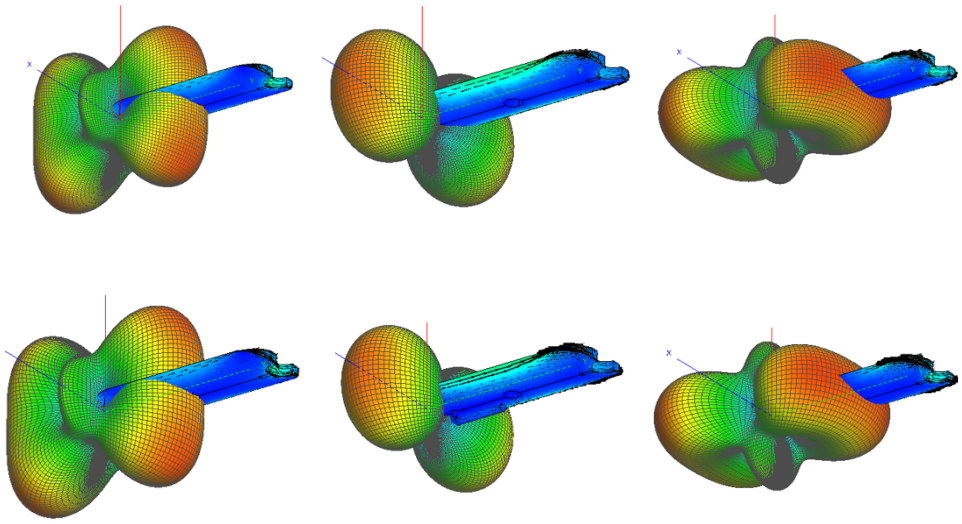

Figure 4.33: The radiation patterns of the last three significant modes of the structure presented in decreasing order from left to right. The top row is the fourth, fifth, and sixth modes of just the SUAS ground plane while the bottom is the ground plane with the IFA attached.

This idea is further corroborated by the radiation patterns shown in Figure 4.31, Figure 4.32, and Figure 4.33. From the radiation pattern plots, it is clear to see that the modal radiation of the first three and last three significant modes of either structure are nearly identical even if the current distribution did change with the addition of the IFA. The radiation pattern of the fourth mode of the ground plane with the IFA stands out from the others and is clearly a new and distinct mode. The most noticeable change in any of the radiation patterns appears to occur in the first mode. When the IFA was added, the modal current distribution no longer looks like two closely located dipoles but instead follows the primary current distribution of an excited IFA. In return, the resulting radiation pattern appears to have greater uniformity in the plane orthogonal to the central axis.

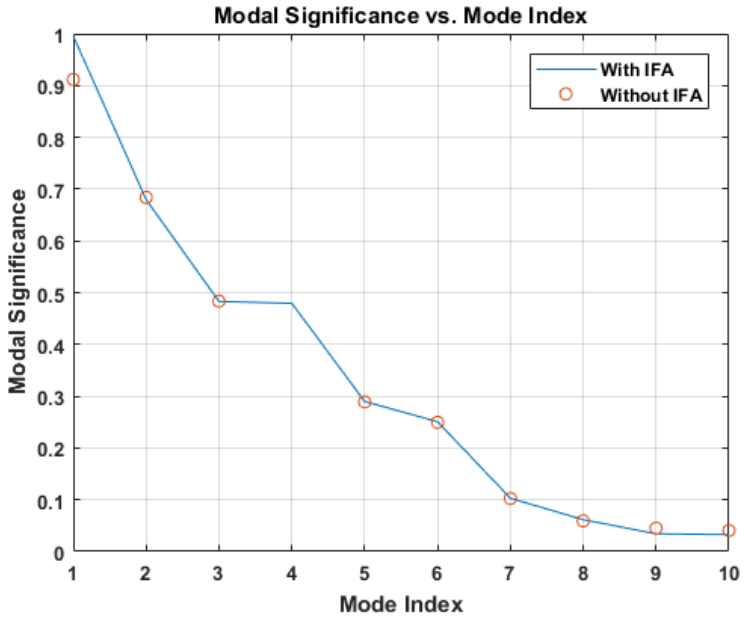

Figure 4.34: A comparison of the modal significance of ground plane modes with and without the IFA. The first nine modes without the IFA are shown in comparison to the first ten modes with the IFA. This discrepancy occurs because the addition of the IFA created a significant fourth mode that does not exist on the original structure.

The previously detailed modal similarities, the IFA's introduction of a new significant mode, and the noticeable divergence between the first mode with and without the IFA are seen once again in Figure 4.34. By shifting the modal index of the ground plane without the IFA after the third mode, it is readily apparent that there is strong agreement between the modal significance of the original six significant modes before and after the IFA's inclusion. Once again, the fourth mode of the SUAS ground plane with the IFA is clearly a new mode introduced by the addition of the IFA. Another detail in Figure 4.34 is that the dominant first mode of the original SUAS ground structure shows the most significant change in modal significance after the addition of the IFA. This deviation is apparent from previous figures, Figure 4.30 and Figure 4.31, detailing the noticeable effects of the IFA on

the current distributions and radiation patterns of this mode.

Although there is not much of a difference between the original six significant modes of the SUAS ground plane and the same modes after the IFA is added, this difference is significant. Because the resonant structure was designed to work with the existing modality, the modal significance and radiation patterns of the original modes were largely unchanged. Instead, the primary difference can be seen in the enhanced current density surrounding the IFA in 4.30. Since the basic theory behind coupling into significant modes relies on the placement of a probe excitation in a region where that mode has a high current density [23], the IFA, by increasing the modal current density around itself, allows for the simultaneous excitation of multiple significant modes with a single element. This simultaneous excitation of multiple modes leads to the desired radiation pattern shown in Figure 4.25. In this way, the addition of a resonant element designed to compliment the modality of the SUAS ground plane introduced a new significant mode and, more importantly, allowed for the simultaneous excitation of multiple existing modes to create a more ideal radiation pattern.

While this analysis did verify the theory underlying the previously described antenna synthesis methodology, for future applications of this method it would be practical to analyze the modal impact of adding the selected resonant structure before analyzing the excited combined structure. This revised order of events would allow for a quick verification that the addition of the resonant structure properly affected the desired impact on the original significant characteristic modes.

4.8 Chapter Summary

Throughout this section, the design of an antenna for quadcopter applications has been performed. The antenna synthesis process began with a characterization of the structure using CMA. From the list of modes significant enough to choose as a radiation basis, the first mode was selected. The resulting attempt to excite the first mode of the ground plane through the use of a non-radiating element was unsuccessful due to the modality of the U-shaped patch. After this setback, a new design process was initiated. Instead of settling for one of the original characteristic modes of the ground plane, a resonant element would be added to the ground plane to alter its fundamental modality. The first step in this process was to reanalyze the original ground plane modes in order to fundamentally understand what the desired surface current distribution should be. The desired surface current distribution was a primarily linear current concentrated on the bottom of the ground plane with some current diffusion towards the edges. An IFA was selected as a resonant element that would create this current distribution. After placing the antenna on the ground plane, the IFA characteristics were tuned to optimize the performance of the antenna in accordance to the system performance. The final antenna design has a simulated bandwidth that spans the operating range of the SUAS radio, with a simulated quasi-isotropic realized gain in the lower hemisphere that satisfies the original conditions of the design. The resulting radiation pattern diverges considerably from the resulting radiation pattern of the same IFA on an electrically large and an electrically small ground plane, proving that the solution was uniquley tailored to the deformed ground plane. Further analysis on the impact of the addition of the IFA has confirmed that its introduction to the SUAS ground plane created a new significant mode while slightly altering the original modality of the structure

so that multiple modes could be excited simultaneously. This in turn produced the previously detailed radiation pattern that optimally solves the original problem by accounting for the modality of both the deformed ground plane and the antenna itself.

Chapter 5

SUAS Antenna Fabrication

5.1 In-House Fabrication

Because the antenna is designed to operate on a SUAS, the weight of the ground plane is a significant design factor. Instead of forming the ground plane through subtractive manufacturing of the object from a solid piece of metal, the ground plane and antenna were fabricated using additive manufacturing. Not only is plastic significantly lighter than metal by volume, but the process of additive manufacturing also allows for the construction of the ground plane with structurally supported air-filled cavities that can decrease the weight of the object without affecting the electrical performance. While this process increases the viability of the design as a practical structure, it does also complicate the fabrication process. Because the designed object is purely composed of plastic, a layer of copper multiple-skin-depths thick must be deposited on the surface of the ground plane for the design to efficiently operate as simulated. To achieve this using in-house fabrication techniques, the electroplating procedure is used for this project. Before electroplating can begin however, the plastic design must first undergo a finishing process where excess material is removed and the surface is smoothed before being made conductive through the use of a conductive aerosol.

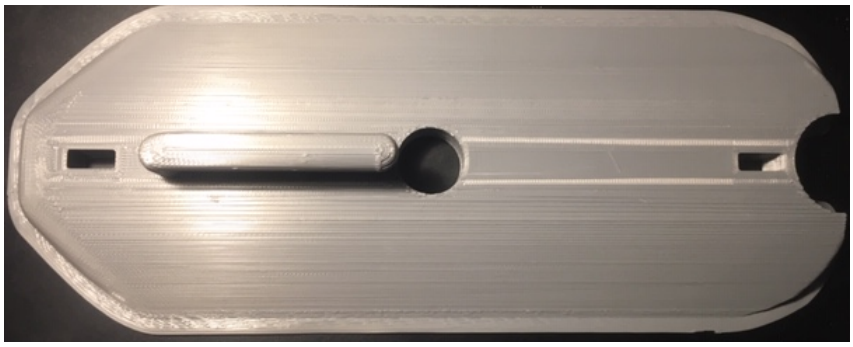

Figure 5.1: The PLA model of the ground plane and IFA

The first step in this additive manufacturing process is to print out the ground plane using a PLA 3D printer. Although the desired additive manufacturing process would have been stereolithography, because it provides significantly higher resolution, the stereolithography printer used in the lab is not large enough to print the craft. Instead, a PLA printer with a larger print base was used. The initial print is shown in Figure 5.1. After the print is complete, the finishing process begins in earnest. First, the excess material must be removed from the outside trim of the ground plane using an X-Acto knife. Then, the required IFA printing supports also should be removed. The results of this process are shown below in Figure 5.2. As can be clearly seen from the enhanced view, there is significant surface roughness involved with the PLA build of the ground plane. This is because the layer resolution for the printer ranges from 0.05-0.4 mm and this finite layer thickness leads to significant surface roughness along the curvature of the ground plane model. This surface roughness if left untreated would increase the surface resistance of the structure and disrupt the outward diffusion of surface currents from the IFA.

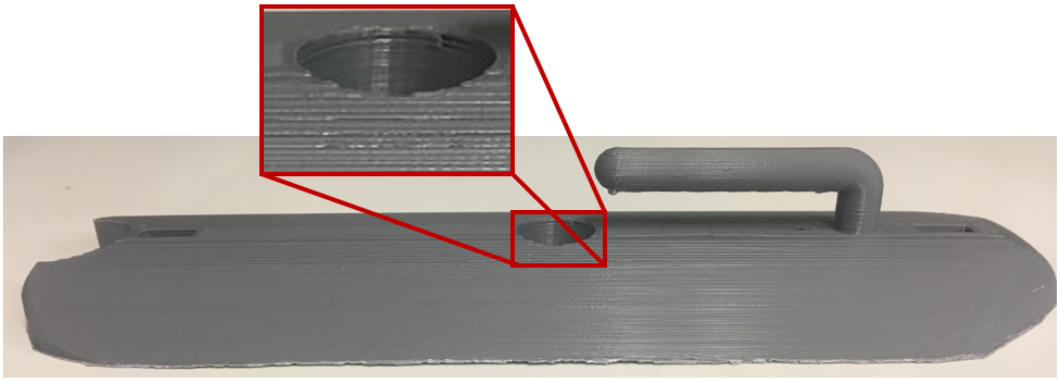

Figure 5.2: The trimmed PLA ground plane with an enhanced view of the craft's surface displaying PLA surface roughness

To correct this surface roughness, the next fabrication step was to sand the craft's surface. The sandpaper grit used on the ground plane was gradually increased until it is smooth to the touch. Once the ground plane was sanded, the next step was to create a conductive seed layer to create enough surface conductivity for the electroplating process to occur. Typically, for via-plating and resin based 3D printed models, a thin layer of copper is added in this step through an electroless plating process. This could not be done for the PLA ground plane for two main reasons. The first problem with this process is that the ground plane is simply too big for the current beakers used for plating 3D printed resin and would require a very large amount of Cu-4000 to be made in a single use batch specifically for this project. The larger issue however is that the PLA print is not actually watertight due to the large tolerances in the printing. It is possible that further iterations of the design could have produced a watertight model by adjusting the resolution settings on the printer. However this was not investigated further and the original prints were not watertight. Because of this, the design would fill with each solution used in the plating process and would either create a hazardous plating condition or simply cause the plating process to fail. Instead of attempting to create the conductive seed layer

through electroless plating, the PLA was sprayed with MG Chemicals Super Shield Silver Coated Copper Conductive Coating. This conductive aerosol is primarily used in electrical shielding for acoustic devices, however it conductive enough to use as a seed layer for the electroplating process and it is viscous enough to form a watertight seal on the ground plane. This seal prevents the ground plane from filling with the plating solution used in the electroplating process. The resulting ground plane after the application of the conductive aerosol can be seen in Figure 5.3. This coating was then sanded once more to smooth out uneven sections of the coating. The conductivity of the model was then preliminary verified using a Fluke Multimeter to verify that there was minimal surface resistance at DC.

Figure 5.3: The sanded and sprayed PLA ground plane

Once the initial seed layer has been created for the ground plane, the electroplating process could begin. For this process, a conductive object is connected to an electrode and then submerged in a tank filled with an acidic solution carrying free copper ions. The other electrode is connected to copper plates that are also submerged in the plating solution. When current flows through the solution, these copper ions are deposited on the object's surface, thus electroplating it. The result of this electroplating process on this ground plane can be seen in Figure 5.4.

The zoomed edge feature shows the two primary problems with electroplating this shape: surface roughness and edge plating. Because of the large relative size of the ground plane, it is difficult to position the craft in such a way between the two copper plates (which provide the solution's copper ions). This leads to increased surface roughness towards the edges of the shape and increases the surface current resistance. The edge plating is another large problem. Because the sharp edges of the ground plane have a higher surface charge than the surface of the plane, copper tendrils form along the edges. This essentially forms a miniaturized bank of capacitors along the edges that cannot be removed without chipping the plating because the electroplated copper adheres more strongly to other electroplated copper than the ground plane. This unintended effect changes the impedance of the ground plane and further reduces the design's efficiency.

Following the electroplating, the last step in the fabrication process is connectorizing the antenna by feeding a candlestick SMA through the ground plane. Although there is a hole for the candlestick SMA to go through in the model, the low resolution on the PLA printer resulted in a mostly filled hole in the final print. So, the first step in connectorization was to drill a hole from the top of the ground plane to the bottom using the drill press. After the hole is drilled, a candlestick SMA connector with copper tape wrapped around the exposed dielectric is inserted through the hole. The SMA is then mechanically connected to the bottom of the craft using a tap and die kit. The electrical connection between the SMA and the ground plane, including both the grounded termination and the probe excitation, is then made using silver epoxy. In this case, silver epoxy is used instead of solder because the heat of the soldering iron would melt the PLA. The connectorization is shown below in Figure 5.5. The connection was tested by measuring the DC resistance between different elements and showed that there was a strong electrical

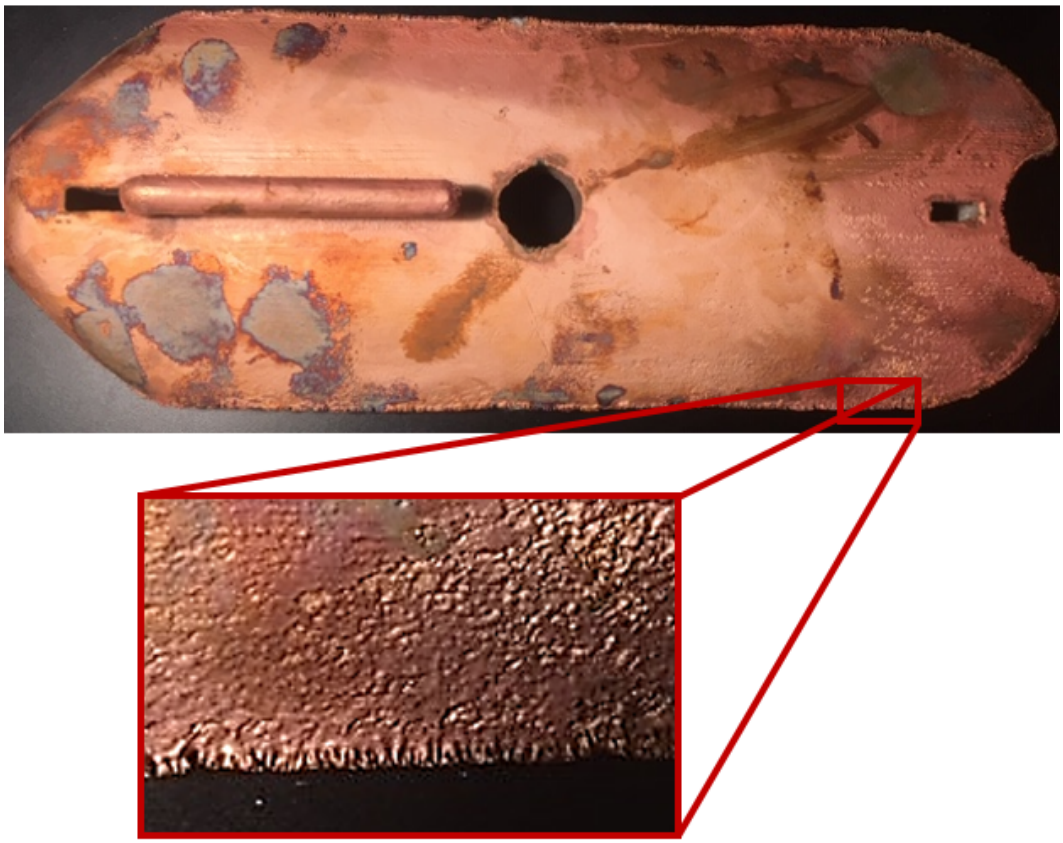

Figure 5.4: The electroplated ground plane with a zoomed view detailing the surface roughness and edge plating effects

connection between the outer SMA shielding and the ground plane. There was also little resistance between the signal pin and the IFA.

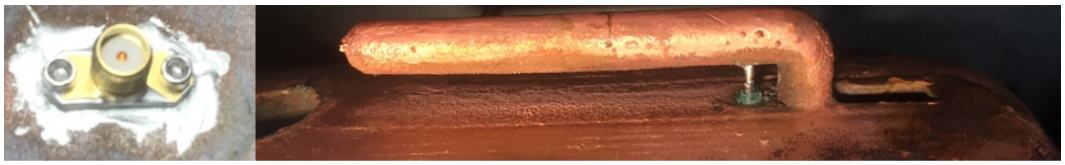

Figure 5.5: The connectorization of the ground plane is shown in this figure. The left image is of the SMA connection to the top of the ground plane and shows the tap and die work and the silver epoxy connection. The right image depicts the connection of the SMA feed pin to the IFA.

With the fabrication of the antenna complete, the final step was to check the accuracy of the fabrication by measuring the return loss of the antenna and comparing

it with the simulated data. This comparison can be seen in Figure 5.6. Clearly, the first fabrication of the antenna was not successful. There are many obvious problems with the process that could be mitigated with subsequent fabrication efforts. First, the electroplating should be done on a lower amps-per-square-foot (ASF) setting. This will cause the charge concentration to be weaker and should decrease the surface roughness by extending the length of the plating process and could reduce the edge plating effects. Possibly the largest problem that could be avoided however was unintended radiation inside the craft itself. Because the hole was not printed correctly by the SLA printer, the final hole in the body of the ground plane for the signal pin to go through was routed through the exposed plastic cavity inside of the copper shell. The copper tape that was wrapped around the candlestick SMA in an attempt to prevent the dielectric coated signal pin from radiating inside the craft was almost certainly not successful. To prevent this unintentional radiation from occurring, the hole for the signal pin should be created using the PLA printer so that the side walls of the hole can then be electroplated. This can be achieved by experimentally determining what initial hole size would result in a final printed hole of the correct diameter according to the original model. Additionally, the candlestick SMA connector should be replaced by a connectorized section of semi-rigid coax. The combination of these two factors would prevent internal radiation and increase the efficiency of the IFA feed while.

Even if these corrective steps are executed properly, there are still numerous problems with the fabrication process that cannot be solved. First and foremost among these problems is the variability of the process itself. Because the rough PLA must first be sanded before being coated by a slightly uneven and unspecified amount of conductive aerosol, there is no set change in the dimensions of the ground plane from the start of the process to the final result. Unlike the printabil-

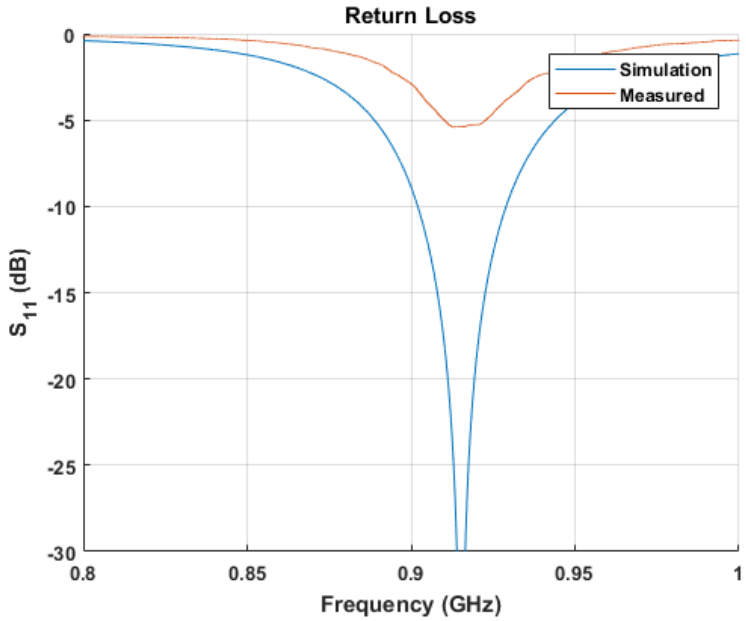

Figure 5.6: Comparison of the return loss between the first fabrication attempt and the simulated return loss

ity of the feed hole for the IFA, there is not a way to experimentally determine a consistent methodology for this process that would result in significantly reduced tolerances. Because of this, the tolerance range of the original SUAS ground plane with the attached IFA must be determined before determining how to proceed with the fabrication.

5.2 Tolerance Analysis

Before beginning the tolerance analysis of the structure, it is important to remember the design characteristics of the IFA described by Figure 4.19. In general, changes to the length of the antenna will primarily affect the operating frequency, moving the feed point will primarily affect the efficacy of the impedance match, and alterations to the separation distance between the antenna and the ground plane or the radius of the wire will serve to change the bandwidth of the antenna. With

this in mind, the performance of the original design of the IFA is shown below in Figure 5.7. The VSWR$\leq$ 2 bandwidth ranges from 902 MHz to 929 MHz with a peak return loss of 67.65 dB at 915.2 MHz. This is a nearly ideal simulated S_{11} measurement as it effectively covers the operating bandwidth of the SUAS radio, which is 902 MHz to 928 MHz, and indicates a good impedance match at the operating freuquency. While the antenna's simulated performance is strong, the narrow VSWR$\leq$ 2 bandwidth range gives little room for error in fabrication.

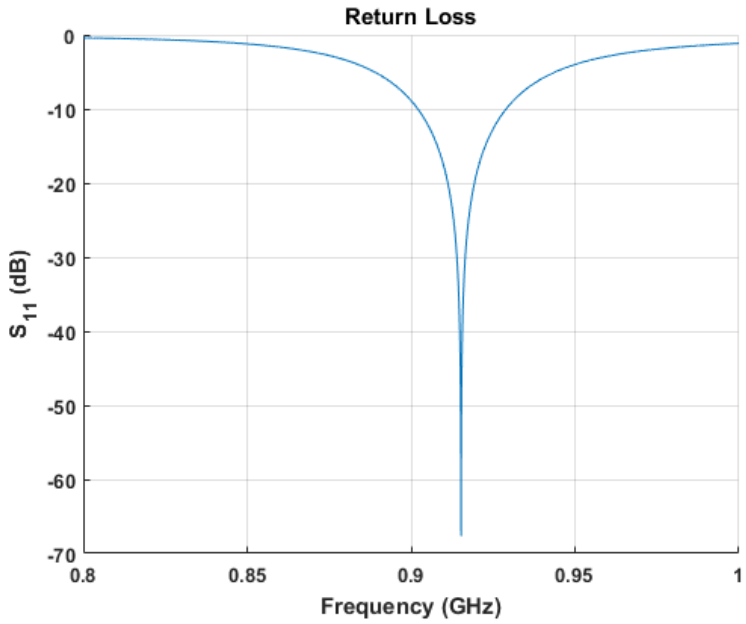

Figure 5.7: The return loss of the original IFA design

The first tolerance that was studied for this project was the conductivity of the metal plating used for the SUAS ground plane. While the original simulation was performed using the conductivity of copper, the electroplating techniques used for in house fabrication do not offer that high of conductivity and so the effects of this change were analyzed. The results are shown in Figure 5.8. Although the maximum return loss is significantly decreased, from over 60 dB shown in Figure 5.7 to less than 35 dB shown in Figure 5.8, by using the lower conductivity value, the conduc-

tivity does not further impact the return loss of the IFA. The VSWR≤ 2 bandwidth of the two are the same. All future simulated comparisons are done with a conductivity of 1.5e7 in order to more accurately represent the fabrication capabilities of the lab.

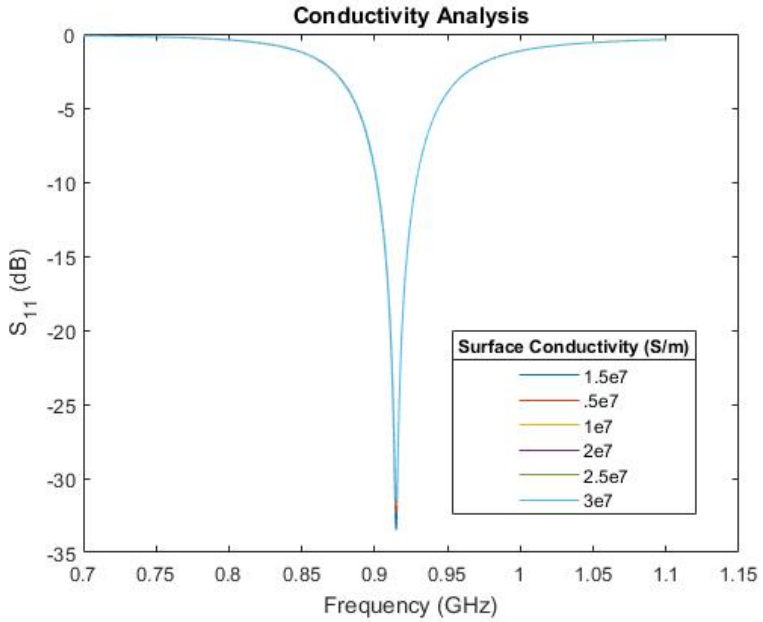

Figure 5.8: A tolerance analysis on the effects of the lower conductivity

The next tolerance case is the length of the antenna. This is important because after the completion of the printing, sanding, spray painting, and electroplating, there is a large possible variation in the length of the antenna. A zoomed graph of this tolerance study is shown in Figure 5.9. The data was compared over a ± 0.8mm range in increments of 0.4 mm. This increment range was chosen because the 3D printer alone has a dimensional accuracy of ± 0.2 mm. Further fabrication tolerances including the variability of the sanding and application of the conductive aerosol would increase this tolerance range. Therefore, a total tolerance of ± 0.4 mm was selected as an approximation of the entire fabrication process. As can be seen in the figure, just a 0.4 mm shift in the total length of the antenna shifts

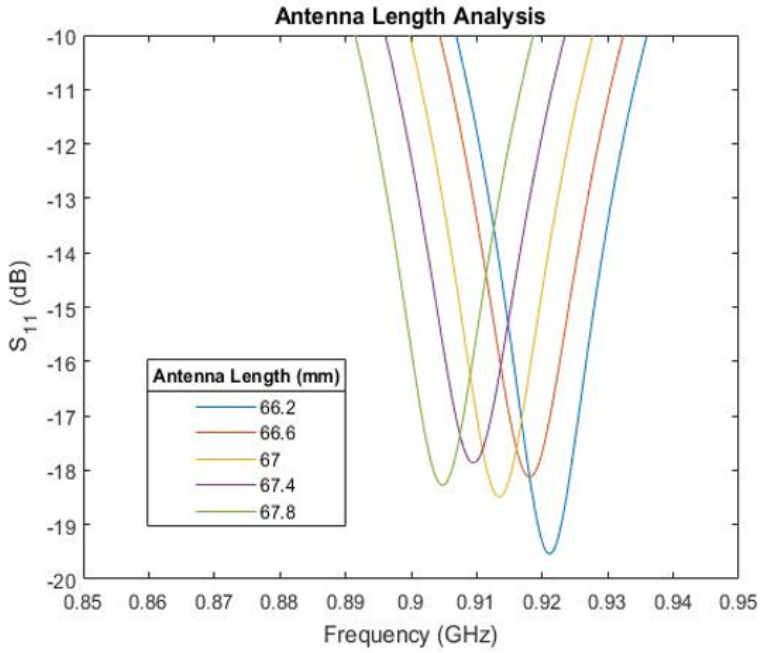

Figure 5.9: A tolerance analysis on the effects of the antenna length

the VSWR$\leq$ 2 bandwidth by approximately 5 MHz. Since the original design had a VSWR$\leq$ 2 bandwidth only 1 MHz larger than the bandwidth required by the SUAS radio, this shift is unacceptable.

After seeing the dramatic impact of changes to the length of the IFA on the resulting operating bandwidth, the effect of changes to the radius were also studied. As is highlighted in Figure 5.10, the same 0.4 mm shift in the physical dimensions of the IFA radius dramatically shifts the VSWR$\leq$ 2 bandwidth of the antenna and significantly reduces the maximum return loss.

Another tolerance case presented here is an analysis of the feed placement for the antenna. Since the existing process for feed placement involves simply drilling a hole through the body of the SUAS ground plane with the drill press, exact accuracy is not possible. Presented in Figure 5.11 is the results of this tolerance case. In this case a 0.5 mm shift causing approximately 5 MHz of shift in the VSWR$\leq$ 2

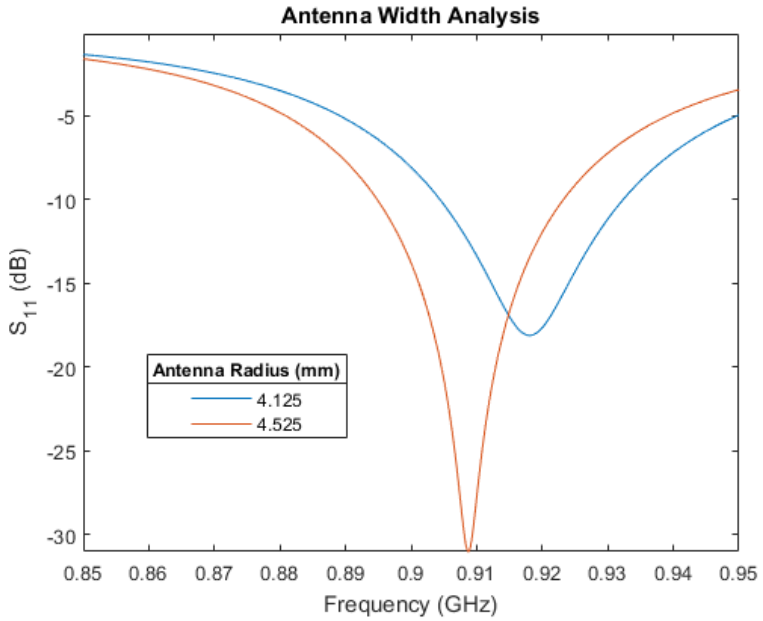

Figure 5.10: A tolerance analysis on the effects of the antenna radius

bandwidth which is once again unacceptable in this design. Further simulations verified that this deviation could be mostly mitigated by bending the IFA feed so that it excited the IFA at the right point. However, this was not an original design consideration and was thus presented as a tolerance case.

After considering only a few of the possible independent tolerances of this design, it is clear that the current model cannot be successfully built with the existing fabrication method. This is because the design fails to meet the project specifications with marginal error in the physical dimensions of the SUAS ground plane with attached IFA. Specifically, this is seen in how very small changes to the length and width of the IFA itself results in dramatic shifts in the VSWR≤ 2 bandwidth. And, these tolerance studies dealt only with independent tolerances. Compounded error from many different tolerance failures is both more likely than the occurrence of a single error and has a more dramatic impact. These compounded failures can result in the poor measured performance of the previously fabricated antenna shown in

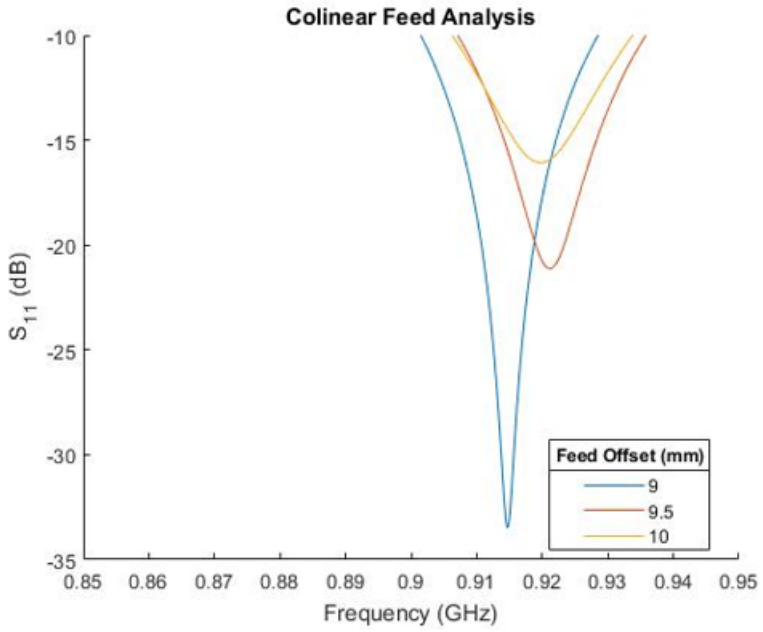

Figure 5.11: A tolerance analysis on the effects of the feed placement

Figure 5.6. In the end, in house fabrication of this antenna was not feasible because of the tight tolerances required for its design and the atypical fabrication methodology required. Instead, the primary fabrication process needs to be contracted out to vendors who can achieve greater accuracy for this design.

5.3 Out of House Fabrication

The overarching solution to the rigid specification of the fabrication process was to work with out-of-house vendors. However, before the model could be sent out of house, the VSWR$\leq$ 2 bandwidth needed to be made greater by increasing the height and the diameter of the IFA. This was done for two main reasons. First, these changes directly increased the tolerable frequency shift by expanding the operational bandwidth of the antenna. Second, having a wider wire radius decreases the percent change caused by the same tolerance shifts to the IFA design and thus in-

creases the designs resistance to variability in the design process. The performance of the final IFA design is first depicted in Figure 4.23 and is shown in comparison to the original design in Figure 5.12. As can be seen in this figure, the redesigned IFA trades the higher return loss of the original design for a greater VSWR$\leq$ 2 bandwidth. As noted previously, the final design has a VSR$\leq$ 2 bandwidth of roughly 30 MHz from 900 MHz to 930 MHz with a minimum S_{11} of -29 dB at 914.5 MHz.

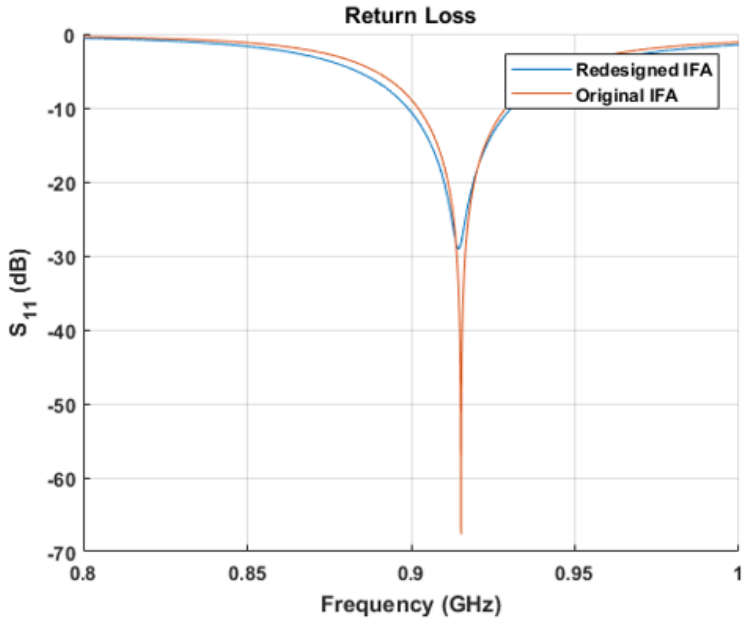

Figure 5.12: The simulated return loss comparison between the initial IFA design and the final design.

The final design was fabricated using stereolithography by Protolabs. The part was printed out of Accura 60 resin in 4 mil layers. The quoted tolerances are ± 0.0508 mm for the first inch of the print and ± 0.0254 mm per inch afterwards in the X/Y dimension and ± 0.127 mm for the first inch and ± 0.0254 mm per inch afterwards in the Z dimension. The plating was done through RepliForm where 12 μm of copper, just over 5 skin depths, was added. This is a significant improvement in the fabrication accuracy of the design. But, to be certain that it would function

properly, the tolerance cases for the design are shown below in Figure 5.13. All of the physical dimensions of the antenna, including the length, radius, height, and feed placement, were analyzed in a parametric to measure the potential impact of the fabrication error. In a worst case scenario, with every compounded tolerance reaching the maximum value of divergence, the highest measured VSWR value was approximately 2.3 instead of the desired 2. This is not ideal, but is acceptable and unlikely to occur.

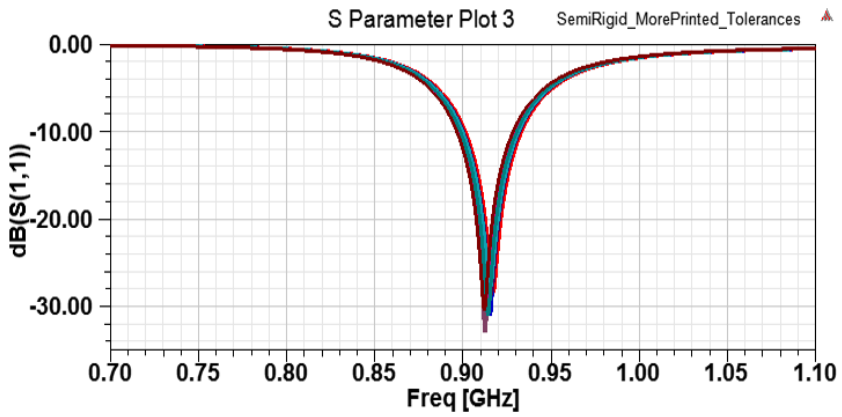

Figure 5.13: The simulated tolerance case for the IFA built out of house.

The result of out of house fabrication is shown below in Figure 5.14. The IFA was then connectorized using a section of semirigid coax that was connected to an SMA cable. This semirigid was electrically connected to the craft using silver epoxy. The resulting connection is shown in Figure 5.15. Overall, the final product appeared very close to the designed model with a smooth craft surface and even copper deposition. The connectorization process was successfully completed and the antenna was then ready to be measured.

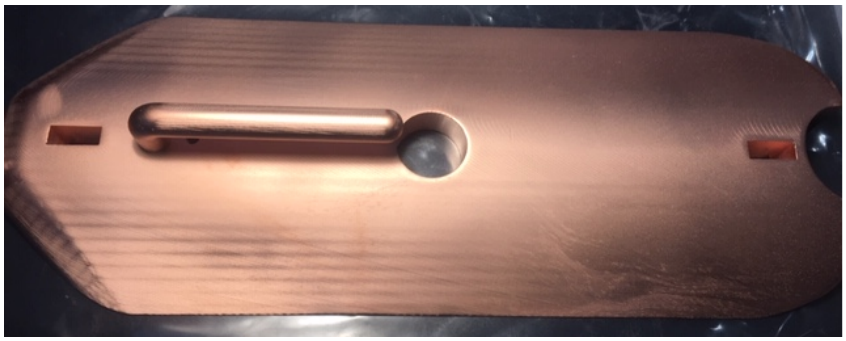

Figure 5.14: The SUAS ground plane with attached IFA fabricated out of house

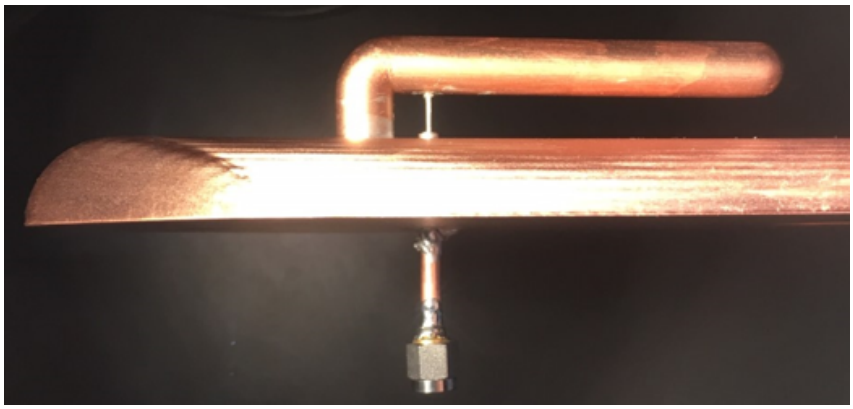

Figure 5.15: The connectorization of the antenna made out of house

5.4 Chapter Summary

At first, the goal was to fabricate a SUAS ground plane with an attached IFA using additive manufacturing and electroplating. However, the in-house fabrication method that was available simply had too much variability for the existing IFA design. To solve this, the antenna design was altered to allow for greater variability in the fabrication process. Finally, the antenna was printed and plated out of house because of the increased accuracy that is possible and then the connectorization was completed in house. The final fabrication closely agreed to the final ground plane design.

Chapter 6

SUAS Antenna Measurements

6.1 Return Loss Measurements

The first step in the measurement process was to measure the return loss of the fabricated antenna to determine the VSWR$\leq$ 2 bandwidth. This preliminary measurement should be a benchmark for the level of success of the fabricated design as previous tolerance analysis has shown that small alterations in the dimension of the structure greatly affect the return loss of the antenna. The antenna was connected to the PNA and supported by a block of foam, as shown in Figure 6.1, for the measurements. The measured return loss is compared to the simulated measurement in Figure 6.2. The measured return loss shows strong agreement with the simulated design. The VSWR$\leq$ 2 bandwidth of the measured antenna begins at 895 MHz and ends at 930 MHz with a maximum return loss of 35 dB occurring at 914 MHz. It should be noted that these original measurements were taken in a semi-metallic environment because of where the PNA is located in the lab. This affected the return loss as the values for S_{11} changed based on how the antenna was oriented. For the data presented below, the antenna was pointed towards the most open part of the measurement area. While this does strongly suggest that the antenna is successfully radiating, it does impact the accuracy of the return loss measurements. Overall, the

initial results suggest that the fabrication was successful with any deviations in the results being caused by small changes between the simulated model and the fabricated design and the measurement environment.

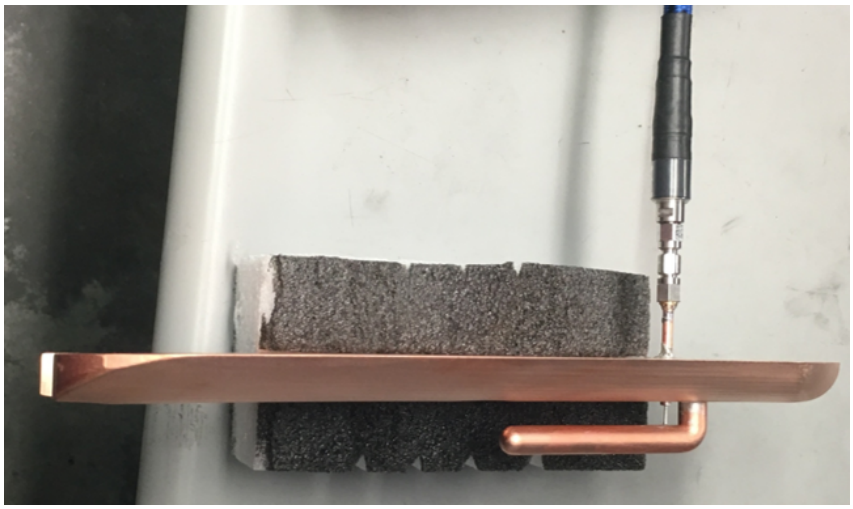

Figure 6.1: The experimental setup for measuring the return loss

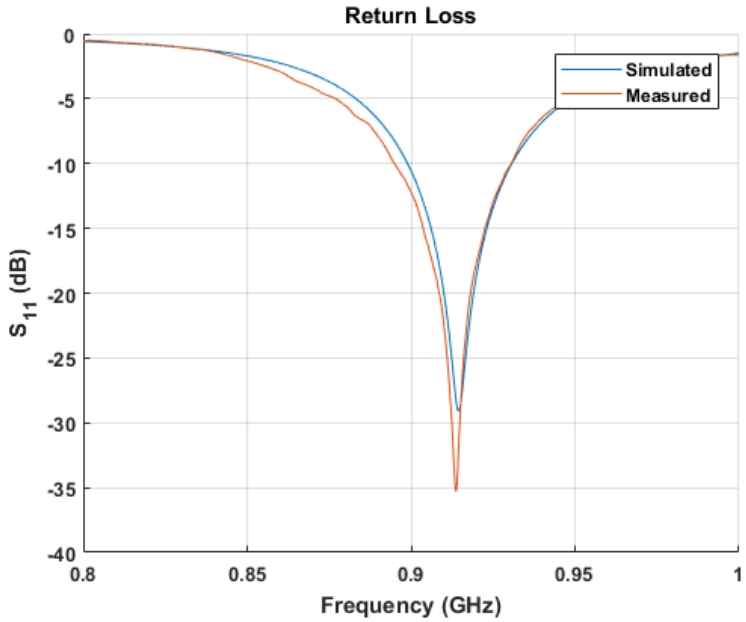

Figure 6.2: The measured return loss of the SUAS antenna compared to the simulated measurement

6.2 Antenna Gain Measurements

With positive results from the initial return loss measurements, the next step in the measurement process was to measure the gain of the antenna. After calibrating the realized gain measurements of the chamber using a dipole antenna connected to a balun operating at 915 MHz, the gain of the IFA was measured in the three cutplanes shown previously in Figure 4.26. The experimental setup for the first measurement of the IFA is shown in Figure 6.3. For this design, the bottom of the SUAS ground plane was first loosely covered with bubble wrap before being inserted into a block of foam for mechanical support. This support system should not have a significant impact on the radiation of the structure as Figure 4.22 shows that this part of the SUAS ground plane has a minimal current distribution. With the SUAS ground plane supported in a vertical position, the foam block was then attached to the measurement pedestal in the anechoic chamber, and the gain was measured. The results of this measurement are shown below in Figure 6.4. Although the general shape shows a strong agreement between the measured and simulated results, the measured pattern has a noticeably higher gain than the simulated results for almost the entire cutplane. This divergence will be further analyzed in the following section detailing the error analysis of these measurements.

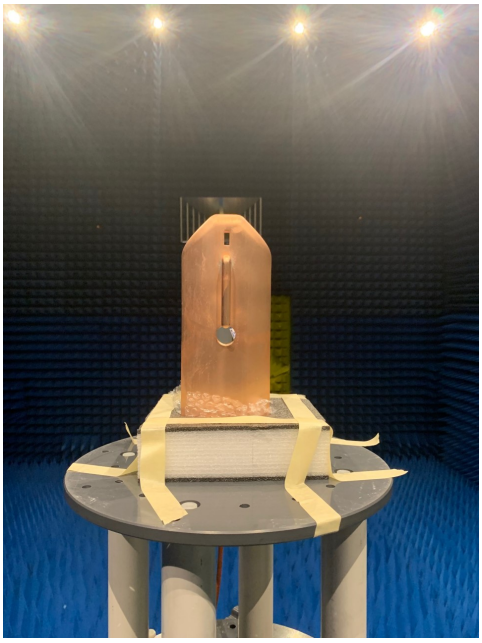

Figure 6.3: The experimental setup for measuring the $\phi = 0°$ cutplane

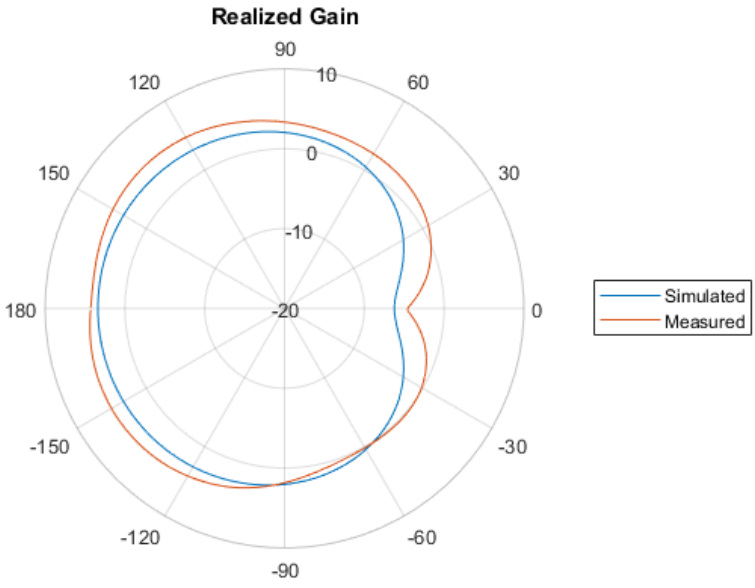

Figure 6.4: The measured vs. simulated realized gain of the Phi=0° cutplane at 915 MHz

The next measurement was of the $\phi = -90°$ cutplane. The experimental setup

is shown in Figure 6.5. For this measurement, the bottom of the SUAS ground plane was held by the same foam block used in the first measurement while the side of the ground plane was supported by another foam block. The results of this measurement are shown in Figure 6.6. Although the measurement shows strong agreement with the simulated results at broadside, $\Theta = 180°$, the measured radiation pattern has a significantly larger backlobe than what was simulated. Furthermore, there is a significant difference between the measured and simulated data as the measurement approached the ends of the antenna, $\Theta = \pm(90° \text{ to } 120°)$.

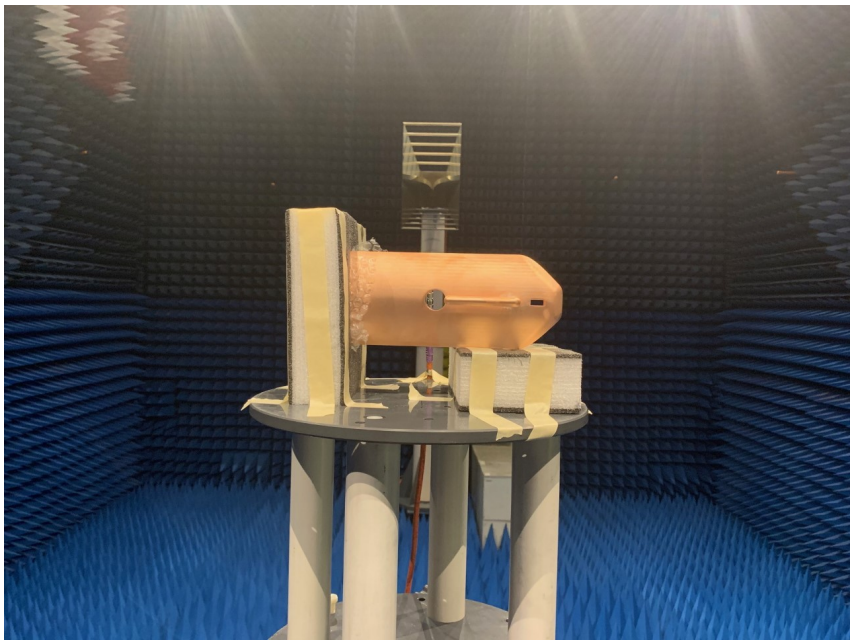

Figure 6.5: The experimental setup for measuring the $\phi = -90°$ cutplane

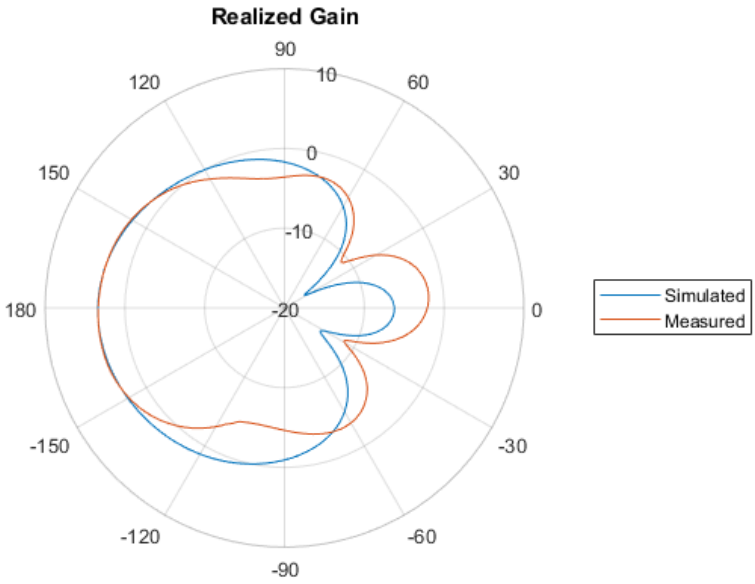

Figure 6.6: The measured vs. simulated realized gain of the $\phi = -90°$ cutplane at 915 MHz

The final measurement was of the $\Theta = 0°$ cutplane. The experimental setup is shown in Figure 6.7. For this measurement, the original block of foam once more holds the bottom of the SUAS ground plane while the top of is supported by another foam block. The results are shown in Figure 6.8. Although the measured results generally agree with the simulated pattern, there is a noticeable increase in the power radiated at $\phi = 0$ and 180 while there is less power radiated at $\phi = 0$ and -90.

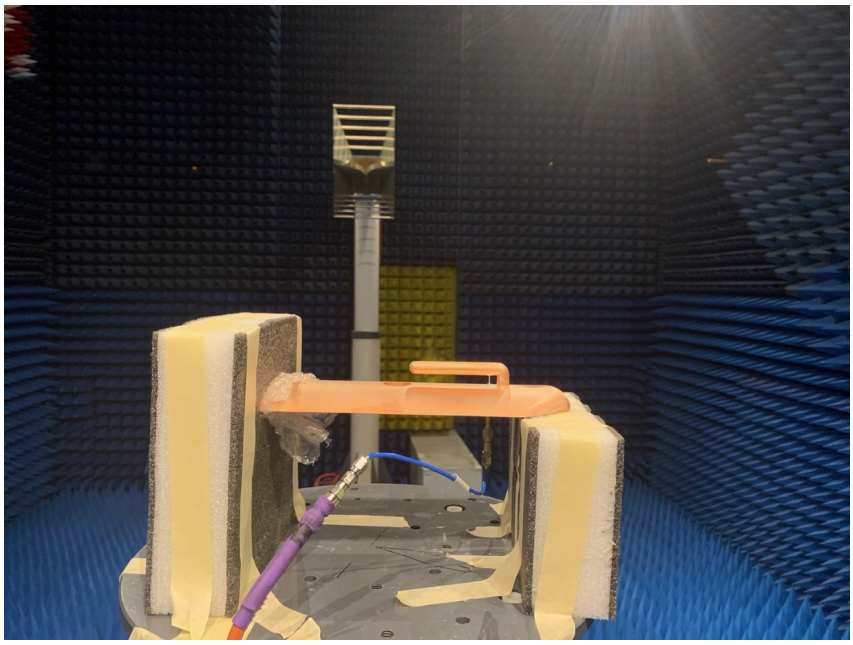

Figure 6.7: The experimental setup for measuring the $\Theta = 0^\circ$ cutplane

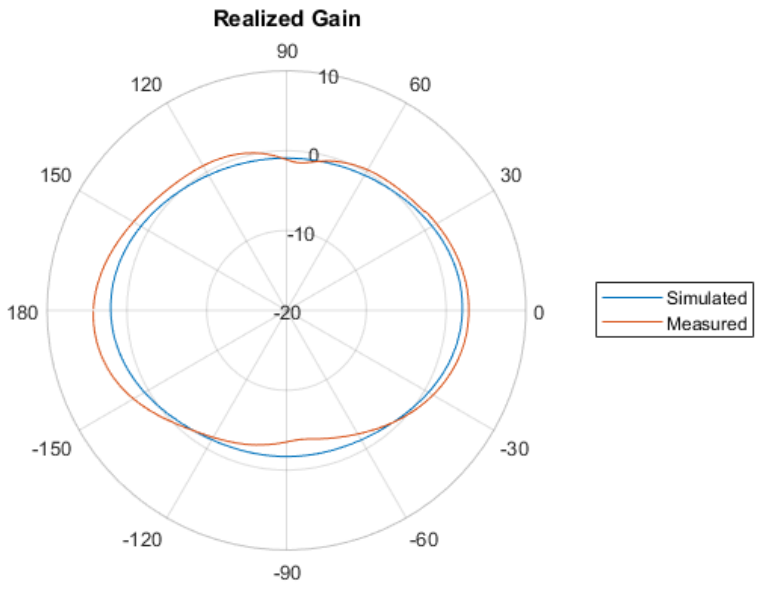

Figure 6.8: The measured vs. simulated realized gain of the $\Theta = 0^\circ$ cutplane at 915 MHz

In the end, the measured results are clearly and consistently divergent from the

simulated model. In each of the measured cutplanes, the realized gain of the fabricated antenna is more directive in the $\phi = 0^\circ$ cutplane at the cost of less directivity in the $\phi = -90^\circ$ cutplane. This divergence from simulation could be caused by a combination of three distinct sources of errors: simulation inaccuracy, fabrication tolerances, and the measurement process. These possible sources of error are further investigated in the subsequent section in an attempt to find the source of the measurement error.

6.3 Error Analysis

As discussed previously, the deviation between the simulated and measured results is likely caused by inaccurate simulations, fabrication, or measurement (or some combination of the three). The first of these error sources that was investigated was simulation inaccuracy. There was the potential for a flaw in the design process because the the original design had its basis in FEKO, while the characterization of the excited structure was entirely simulated in HFSS. This potential for error was heightened because HFSS has a difficulty meshing surface curvature, and could therefore have inaccurately simulated the effects of exciting a resonant wire antenna above a curved surface. To see if this error existed, the model of the SUAS ground plane with an excited IFA was simulated in FEKO and the results of the comparison between the simulations in the three primary cutplanes is shown in Figure 6.9. Although the FEKO model has slightly less realized gain across all of the cutplanes, it is clear that there is very strong simulation agreement. Both simulation engines independently arrived at almost exactly the same result. This indicates that there was not simulation error and that one of the other two possible sources of error is the reason for the difference between the measured and simulated results.

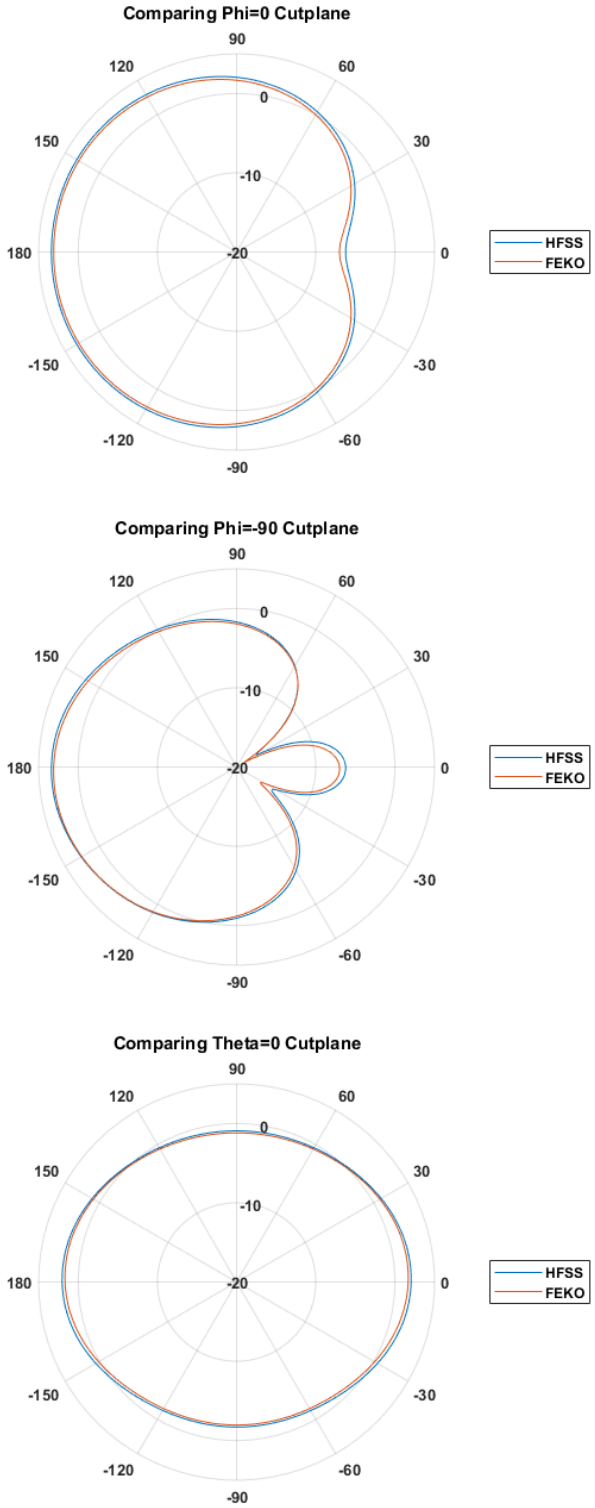

Figure 6.9: Comparison of realized gain between HFSS and FEKO for the three primary cutplanes at 915 MHz

The next source of error that was investigated was inaccurate fabrication. Now that the simulation accuracy has been confirmed, this error investigation was done using an HFSS parametric sweep. After sweeping the quoted fabrication tolerances produced no noticeable change to the realized gain in the two Θ cutplanes, the tolerances were increased to ± 0.5 mm for all of the antenna parameters. The results of this analysis are shown in Figure 6.10. As can be seen from this figure, not even an analysis of compounded tolerances significantly outside the quoted range produced a significant change in the realized gain of the IFA on the SUAS ground structure. Therefore, the error in the realized gain measurements was likely not caused by fabrication inaccuracy.

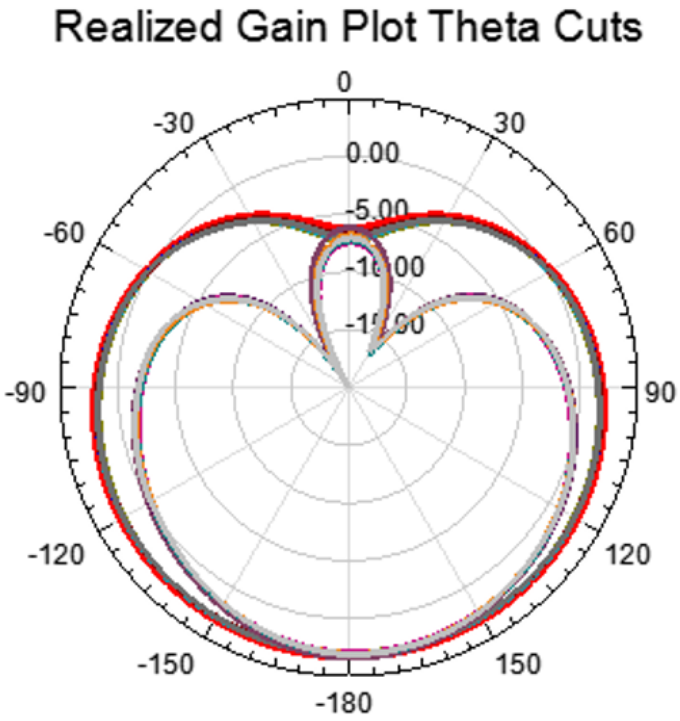

Figure 6.10: Tolerance analysis of fabrication effects on the realized gain of the IFA antenna at 915 MHz

With the divergence between the previous measurements and the simulated results not due to simulation inaccuracy or the fabrication error, the only remaining

source of error was measurement error. The first step in identifying the source of the measurement error was to measure the effect of the foam support system on the return loss of the antenna. For this experiment, the return loss of the antenna was measured with and without the foam supports in a miniature anechoic chamber. This chamber, shown in Figure 6.11, minimized the previously discussed environmental impact on the return loss and improved the accuracy of the measurements. The graphical comparison of the two measurements is shown in Figure 6.12. Clearly, the foam support does not affect the IFA's return loss. Furthermore, as depicted in Figure 6.13, the return loss measured in the small anechoic chamber more closely agrees with the simulated values than the initial measurement. The VSWR bandwidth is practically identical between the secondary measurements and the simulation. The only divergence between the two is that the measured system has a lower maximum return loss than what was simulated. This can be explained by inefficiencies in the connectorization process and surface roughness. Overall, this measurement primarily proves that the foam supports did not alter the realized gain patterns by affecting the return loss of the antenna. Additionally, the new measurements in the anechoic chamber further demonstrate that the fabrication was successful.

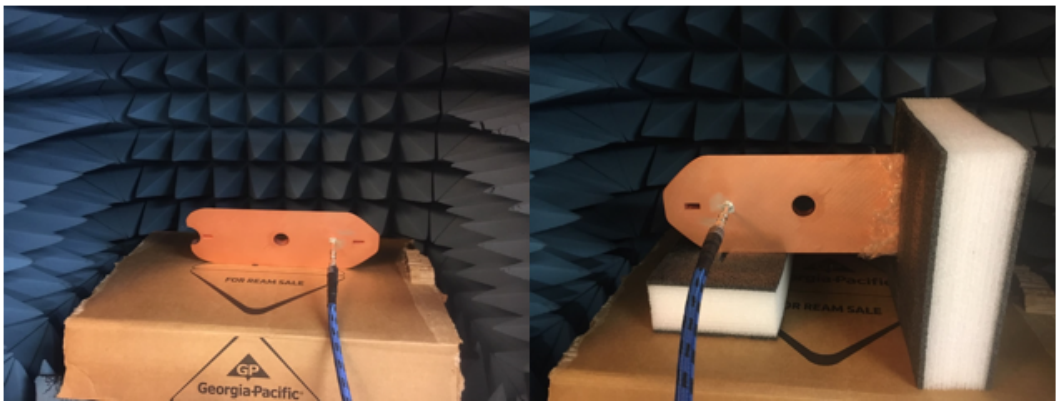

Figure 6.11: Measurement setup for the comparative return loss measurements

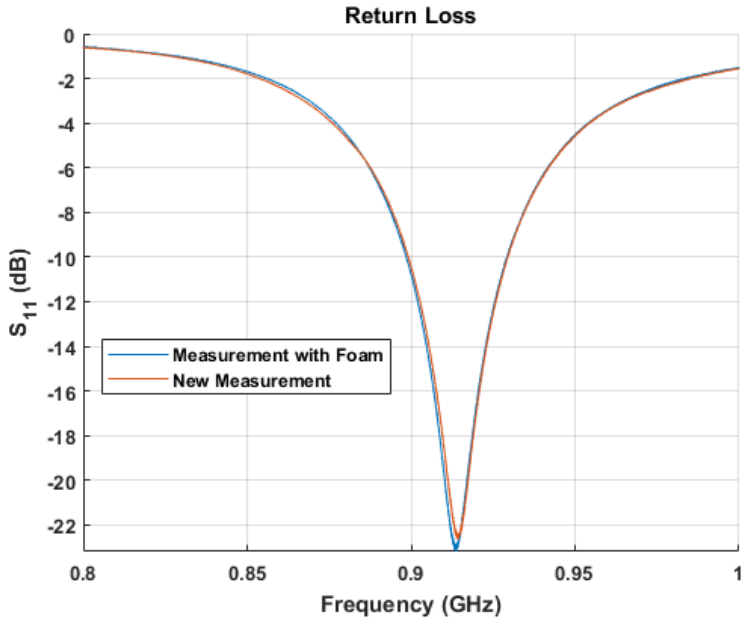

Figure 6.12: System return loss with and without foam supports

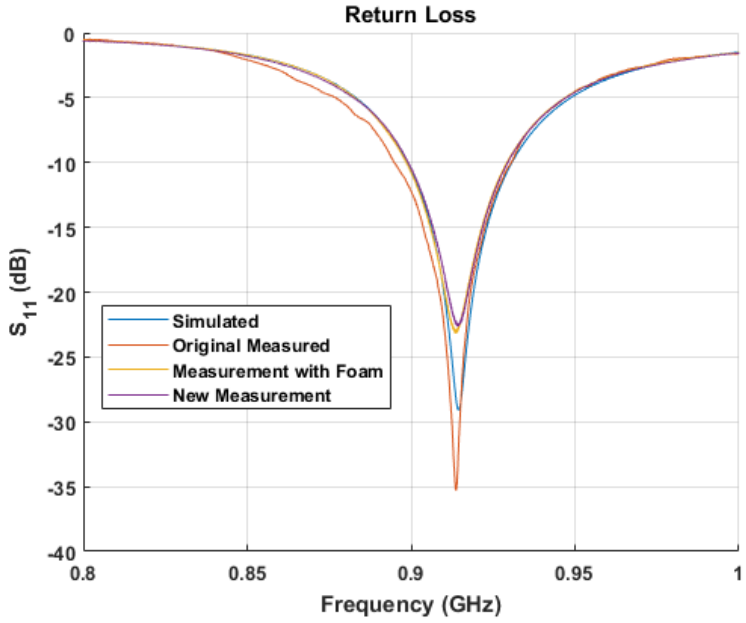

Figure 6.13: All return loss measurements compared to simulation

After the foam's effect on the return loss of the antenna was characterized and subsequently ruled out as a source of error, the next source of error to be investigated

was the foam's direct effect on the radiated gain. The greatest divergence in the lower hemisphere's radiation pattern, shown in Figure 6.6, occurred at the the angle where the SUAS antenna would be radiating through the foam support. Because the measured gain was significantly less than expected in this range, it is possible that the foam acts as an absorber and therefore is particularly ill-suited to measure this cutplane. To test this result, the support was replaced by a large section of cardboard, shown in Figure 6.14. The results of this measurement can be seen in Figure 6.15. The measurement taken with the large cardboard support is clearly closer to the simulated result than the measurement taken on the form support. From this plot, it can be determined that the foam acted as a directional absorber that affected the accuracy of the gain measurement.

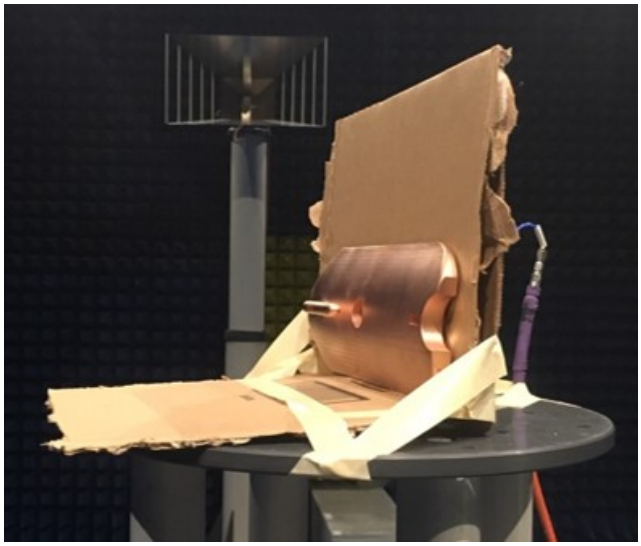

Figure 6.14: Cardboard as a support structure

Now that the foam has been discovered to be the source of the original measurement error, the final step in this process was to improve on the cardboard support system shown in Figure 6.14. The new cardboard support for the measurement of the $\phi = -90^{\circ}$ cutplane is shown below in Figure 6.16.

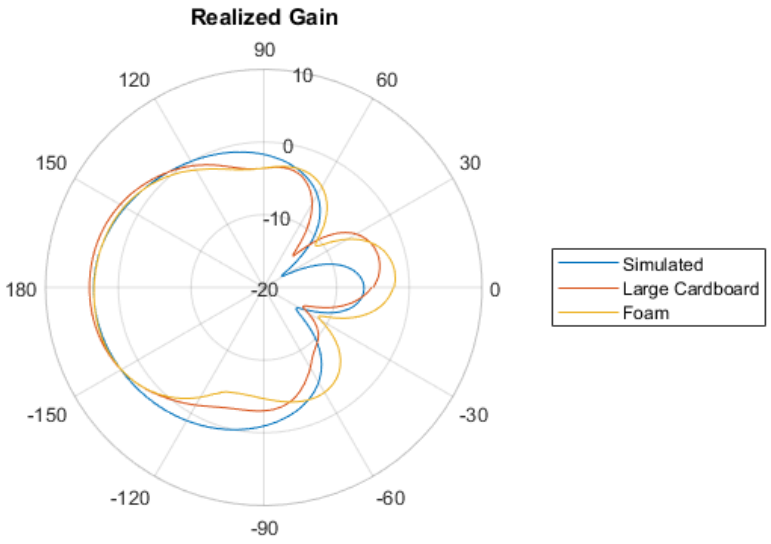

Figure 6.15: Realized gain comparison in the $\phi = -90°$ cutplane at 915 MHz

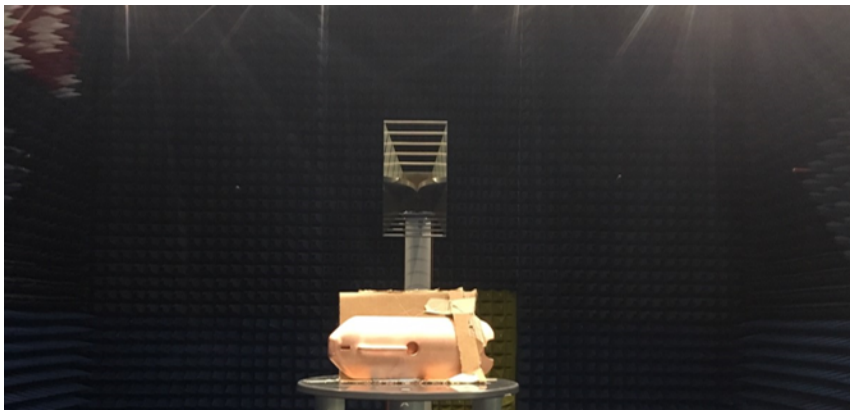

Figure 6.16: Improved cardboard support structure

From Figure 6.17, it can be seen that the use of a smaller cardboard support is the closest match to the simulated realized gain. The improved results are due to the fact that the small cardboard support minimizes possible reflections and absorbtion seen by other materials and larger support structures. Future measurements will rely on efficient cardboard supports to more accurately measure the realized gain.

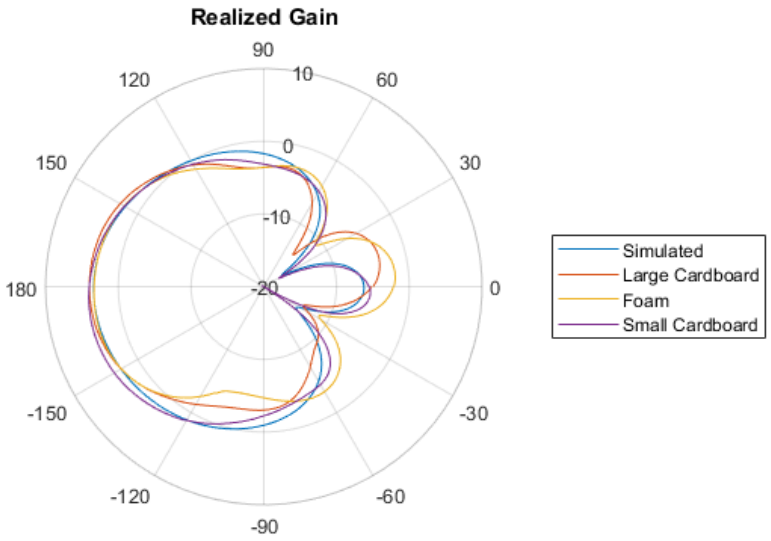

Figure 6.17: Comparison of the $\phi = -90°$ cutplane radiation patterns at 915 MHz based on the support system used

6.4 Effects of Metallic Loading

After the verification of the antenna performance in "air" was completed, the effects of metallic loading on the antenna could be measured. It was shown in [17] that the compact design of quadcopters and their internal electronics creates a complex metallic environment that causes severe performance degradation and placement sensitivity for standard antennas. This antenna system was designed in large part to prevent this effect by essentially placing a radiation boundary between the radiating element and the craft's internals. In order to measure the efficacy of this design in a practical context, two quadcopter batteries were connected to the back of the cardboard support structure seen in Figure 6.16. This setup is shown in Figure 6.18 and the results are shown in Figure 6.19.

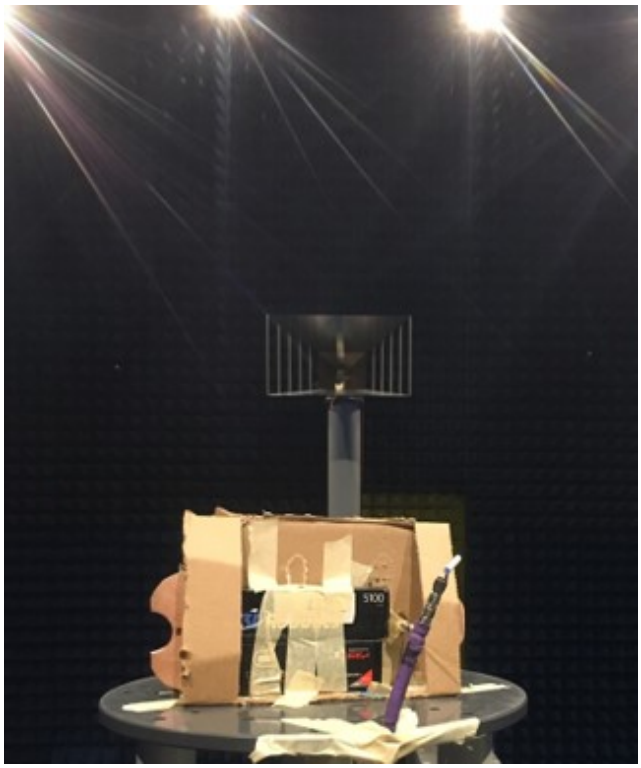

Figure 6.18: Small cardboard support structure with SUAS batteries attached to the back

Figure 6.19 shows that the addition of the batteries to the structure does not change the realized gain of the antenna. Because [17] discovered that the battery was the most significant metallic load in the SUAS, and since the batteries in this test were placed within 0.01λ of the top of the antenna ground plane, it can be stated with a high degree of certainty that this antenna is not affected by practical metallic loading from SUAS internals.

The reason why the only realized gain measurements, after the first set of measurements using foam supports, were of the $\phi = -90^{\circ}$ cutplane is of note. At first, this was out of necessity after the initial measurements showed that this cutplane had the largest divergence between the measurements and the simulated results. After successful completion of the measurements in this cutplane, the measurements

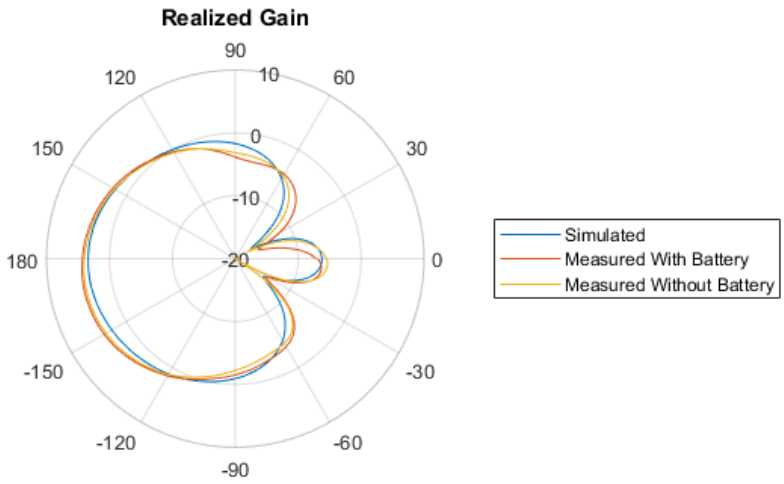

Figure 6.19: Effects of metallic loading on the $\phi = -90°$ cutplane radiation pattern at 915 MHz

of the other two cutplanes needed to be redone for greater accuracy and to report the effects of metallic loading. However, before this could be done, the IFA was irreparably broken from the body of the craft. Future work will be necessary to take these measurements

6.5 Chapter Summary

Over the course of the measurement process, several key aspects of the antenna design were verified. First, the final fabrication method, including the work done out of house and the connectorization method, was deemed an initial success based on the close match between the measured and simulated return loss values. Later, the strong agreement between realized and simulated gain measurements verified that the antenna synthesis method, fabrication process, and final measurement setup were valid for future designs and measurements. At the end of the measurement

process, the entire design hypothesis was validated when the addition of two SUAS batteries less than 0.01λ away from the ground plane did not significantly alter the realized gain pattern. In the end, the success of the antenna design and fabrication was verified as multiple accurate measurements proved that the antenna radiated quasi-isotropically in the lower hemisphere while being unaffected by metallic loading.

Chapter 7

Conclusions and Further Work

7.1 Conclusion

Unmanned aerial vehicles are becoming increasingly prevalent in private, commercial, and public use. SUAS communication requires a consistent signal connection so that the system can be safely remotely operated while maintaining a strong data up-link for any remote sensing capabilities. The realized gain of the antenna needs to be quasi-isotropic so that the signal reception will remain strong regardless of platform orientation. Furthermore, efficient long-range communication for these SWaP constrained devices necessitates relatively low frequency communication using antennas that are compact and aerodynamic. The commercial SUAS antenna market is dominated by two antennas that do not meet these basic requirements. The first popular antenna is an inefficient inductively loaded monopole antenna that is relatively aerodynamic at the cost of significant radiation nulls when applied to a SUAS. The other commonly available SUAS antenna is the skew-planar antenna that is prohibitively large at the lower frequencies required to avoid significant attenuation at longer ranges. While the general capabilities and mechanical complexity of the SUAS continue to grow as the technology underlying their design develops, the antenna performance of these vehicles continues to be rudimentary at best.

Previous attempts to design an antenna that performs demonstrably better led to the design and characterization of planar quasi-isotropic structures that could be conformally applied to the SUAS [17]. While these structures showed significant operational benefits when applied to the foam or plastic wings of fixed wing platforms, their performance suffered notable degradation when applied to quadcopters because of the densely packed metallic internals. To correct this, a new antenna had to be designed to optimally function in this environment.

The design of the new antenna began with the creation of an aerodynamic ground plane that would serve as a radiation boundary to mitigate the impact of craft internals on the antenna's radiation. This structure was then analyzed using the theory of characteristic modes to determine the ideal current distribution on the ground plane's surface. A resonant structure with this generalized current distribution was then placed on the structure. This addition both altered the existing modality of the ground plane and created a new significant mode so that the excitation of the resonant structure resulted in the simultaneous excitation of several significant ground plane modes. The resulting radiation pattern was quasi-isotropic in the craft's lower hemisphere and was unaffected by metallically loading the structure. Thus, the final design was ideal for the communication system of a quadcopter SUAS.

7.2 Scientific Impact

Nominally, the overarching goal of this project was completed with the successful fabrication and measurement of the SUAS antenna. This new antenna was designed specifically for quadcopter SUAS applications and has the potential to significantly improve the overall performance of meteorological SUAS by improving

data fidelity rates and increasing the maximum communication range. However, the larger contribution to science as a whole was not the design of this specific antenna. Rather, it was the derivation of a novel antenna synthesis process. Previous research on the method of moments and characteristic modal analysis has relied almost exclusively on analyzing a metallic structure and designing a feed network to directly couple into an existing mode. Some research has been done on altering the metallic structure to improve the bandwidth of a radiating element while other research has been completed on the creation of MIMO radiators by coupling into two or more orthogonal modes of the structure. However, to the authors knowledge, this research is the first time that the theory of characteristic modes has been utilized to select and place a characterized resonant element with the goal of altering the impedance of the original structure to allow for the efficient and simultaneous excitation of multiple significant modes on an electrically medium ground plane. The potential impact of this development is significant as it offers an alternative antenna synthesis procedure based on the theory of characteristic modes for many metallic objects.

7.3 Further Work

Initially, the further work needs to be focused upon the collection of additional measurements and the improvement of the existing design. These measurements would include the additional realized gain cutplanes for both the loaded and unloaded structure as well as measurements of flight data to demonstrate the practical performance characteristics. Before flight data can be taken, the internals of the existing quadcopter will need to be slightly adjusted to allow for the antenna to connect to the SUAS radio. Subsequently, the SUAS ground plane will need to be

conformally attached to the rest of the craft. With corroborating flight data to validate the chamber measurements, the only remaining goals on this individual project will be research into improving the practicality of the design. This research would include, but not be limited to, the design of a hollow core to the SUAS ground plane to reduce its weight, an investigation of other fabrication methodologies to create a more stress resistant IFA, and a study on the tradeoffs among the resulting radiation pattern, aerodynamics, and structural viability of the addition of a radome to the design that would cover the IFA.

Even once this individual project is complete, the further work into this topic is potentially expansive. To begin, another attempt at applying the general antenna synthesis procedure presented in this paper to other electrically medium designs to determine its efficacy would be important. If the method proves to be effective, subsequent research could work to expand the theory and build a repository of functional examples demonstrating its application.

References

[1] J. Granger and J. Bolljahn, "Aircraft antennas", *Proceedings of the IRE*, vol. 43, no. 5, pp. 533–550, 1955.

[2] Y. Chen and C.-F. Wang, "Electrically small uav antenna design using characteristic modes", *IEEE Transactions on Antennas and Propagation*, vol. 62, no. 2, pp. 535–545, 2014.

[3] Z.-Q. Liu, Y.-S. Zhang, Z. Qian, Z. P. Han, and W. Ni, "A novel broad beamwidth conformal antenna on unmanned aerial vehicle", *IEEE Antennas and Wireless Propagation Letters*, vol. 11, pp. 196–199, 2012.

[4] K. Obeidat, R. G. Rojas, and B. Raines, "Design of antenna conformal to v-shaped tail of uav based on the method of characteristic modes", in *Antennas and Propagation, 2009. EuCAP 2009. 3rd European Conference on*, IEEE, 2009, pp. 2493–2496.

[5] L. Gupta, R. Jain, and G. Vaszkun, "Survey of important issues in uav communication networks", *IEEE Communications Surveys & Tutorials*, vol. 18, no. 2, pp. 1123–1152, 2016.

[6] E. W. Frew and T. X. Brown, "Airborne communication networks for small unmanned aircraft systems", *Proceedings of the IEEE*, vol. 96, no. 12, 2008.

[7] H. Nakano, N. Chiba, and J. Yamauchi, "Numerical analysis of collinear monopole antennas with coils", *Electronics letters*, vol. 27, no. 12, pp. 1103–1104, 1991.

[8] T. Tanaka, S. Egashira, and A. Sakitani, "Am-fm-cellular mobile telephone tri-band antenna with double sleeves", in *Antennas and Propagation Society International Symposium, 1991. AP-S. Digest*, IEEE, 1991, pp. 958–961.

[9] I. K. Kim and V. V. Varadan, "Flexible isotropic antenna using a split ring resonator on a thin film substrate", in *Antennas and Propagation (APSURSI), 2011 IEEE International Symposium on*, IEEE, 2011, pp. 3333–3335.

[10] A. Mehdipour, H. Aliakbarian, and J. Rashed-Mohassel, "A novel electrically small spherical wire antenna with almost isotropic radiation pattern", *IEEE Antennas and Wireless Propagation Letters*, vol. 7, pp. 396–399, 2008.

[11] D. Bugnolo, "A quasi-" isotropic" antenna in the microwave spectrum", *IRE Transactions on Antennas and Propagation*, vol. 10, no. 4, pp. 377–383, 1962.

[12] H. Mathis, "A short proof that an isotropic antenna is impossible", *Proc IRE*, vol. 39, no. 8, p. 970, 1951.

[13] ——, "On isotropic antennas", *Proc IRE*, vol. 42, p. 1810, 1954.

[14] W. Saunders, "On the unity gain antenna", *Electromagnetic Theory and antennas*, p. 1125, 1963.

[15] W. Scott and K. Hoo, "A theorem on the polarization of null-free antennas", in *1965 Antennas and Propagation Society International Symposium*, vol. 3, Aug. 1965, pp. 282–282. DOI: 10.1109/APS.1965.1150296.

[16] G. Deschamps, J. Dyson, and P. Mast, "Two-port isotropic radiator for unpolarized waves", *IEEE Transactions on Antennas and Propagation*, vol. 17, no. 6, pp. 809–810, Nov. 1969, ISSN: 0018-926X. DOI: 10.1109/TAP.1969.1139543.

[17] T. Poydence, *Structure-independent Conformal Quasi-isotropic Antennas for Small Unmanned Aircraft System Applications*. University of Oklahoma, 2017. [Online]. Available: https://books.google.com/books?id=TFe2uQEACAAJ.

[18] A. Stjernman, "Antenna mutual coupling effects on correlation, efficiency and shannon capacity", in *Antennas and Propagation, 2006. EuCAP 2006. First European Conference on*, IEEE, 2006, pp. 1–6.

[19] R. Tanner, "Shunt and notch-fed hf aircraft antennas", *IRE Transactions on Antennas and Propagation*, vol. 6, no. 1, pp. 35–43, 1958.

[20] C. F. Corbin and G. A. Akers, "Analysis of angle of arrival estimation at hf using an ensemble of structurally integrated antennas", in *Signal Processing, Sensor Fusion, and Target Recognition XXII*, International Society for Optics and Photonics, vol. 8745, 2013, 87451H.

[21] J. Anguera, A. Andújar, and C. García, "Multiband and small coplanar antenna system for wireless handheld devices", *IEEE Transactions on Antennas and Propagation*, vol. 61, no. 7, pp. 3782–3789, 2013.

[22] N. L. Bohannon and J. T. Bernhard, "Design guidelines using characteristic mode theory for improving the bandwidth of pifas", *IEEE Transactions on Antennas and Propagation*, vol. 63, no. 2, pp. 459–465, 2015.

[23] ——, "Utilizing the impedance matrix to design antennas with a characteristic far-field pattern", *IEEE Antennas and Wireless Propagation Letters*, vol. 16, pp. 2836–2839, 2017.

[24] C. Balanis, *Antenna Theory: Analysis and Design*, 3rd ed. Hoboken, NJ: John Wiley & Sons, 2005.

[25] J. F. Kuhling, M. Feenaghty, and R. Dahle, "A wideband cascaded skew planar wheel antenna for rf energy harvesting", in *2018 IEEE Wireless Power Transfer Conference (WPTC)*, IEEE, 2018, pp. 1–4.

[26] R. Mellen and C. Milner, "The skew-planar wheel antenna", *QST*, Nov. 1963.

[27] K. Fujimoto and J. James, Eds., *Mobile Antenna Systems Handbook*, 1st. Norwood, MA, USA: Artech House, Inc., 1994, ISBN: 089006539X.

[28] R. Burberry, "Electrically small antennas: A review", in *IEE Colloquium on Electrically Small Antennas*, IET, 1990, pp. 1–1.

[29] HMGCC, *Loop antennas*, Allerton Antenna Applications Symposium, 2015.

[30] ARRL, "A circular antenna for u.h.f.", *QST*, Nov. 1942.

[31] S. R. Best, "Improving the performance properties of a dipole element closely spaced to a pec ground plane", *IEEE Antennas and Wireless Propagation Letters*, vol. 3, no. 1, pp. 359–363, 2004.

[32] A. Ayorinde, S. Adekola, and A. I. Mowete, "Analysis of a circular-loop antenna backed by a circular ground-plane of finite extent", in *2017 Progress In Electromagnetics Research Symposium-Spring (PIERS)*, IEEE, 2017, pp. 173–179.

[33] H. A. Hejase, S. D. Gedney, and K. W. Whites, "Effect of a finite ground plane on radiated emissions from a circular loop antenna", *IEEE Transactions on Electromagnetic Compatibility*, vol. 36, no. 4, pp. 364–371, 1994.

[34] K. Iizuka, R. King, and C. Harrison, "Self-and mutual admittances of two identical circular loop antennas in a conducting medium and in air", *IEEE Transactions on Antennas and Propagation*, vol. 14, no. 4, pp. 440–450, 1966.

[35] M. M. Ney, "Method of moments as applied to electromagnetic problems", *IEEE transactions on microwave theory and techniques*, vol. 33, no. 10, pp. 972–980, 1985.

[36] R. Harrington and J. Mautz, "Theory of characteristic modes for conducting bodies", *IEEE Transactions on Antennas and Propagation*, vol. 19, no. 5, pp. 622–628, 1971.

[37] R. F. Harrington, *Field computation by moment methods*. Wiley-IEEE Press, 1993.

[38] Z. Chen and M. M. Ney, "Method of moments: A general framework for frequency-and time-domain numerical methods", in *2007 Workshop on Computational Electromagnetics in Time-Domain*, IEEE, 2007, pp. 1–4.

[39] M. N. Sadiku, *Numerical techniques in electromagnetics*. CRC press, 2000.

[40] G. Guarnieri, S. Selleri, G. Pelosi, C. Dedeban, and C. Pichot, "Innovative basis and weight functions for wire junctions in time domain moment method", *IEE Proceedings-Microwaves, Antennas and Propagation*, vol. 153, no. 1, pp. 61–66, 2006.

[41] T. J. Higgins and D. K. Reitan, "Calculation of the capacitance of a circular annulus by the method of subareas", *Transactions of the American Institute of Electrical Engineers*, vol. 70, no. 1, pp. 926–933, 1951.

[42] U. Grenander and G. Szegö, *Toeplitz forms and their applications*. Univ of California Press, 1984.

[43] R. Garbacz, "Modal expansions for resonance scattering phenomena", *Proceedings of the IEEE*, vol. 53, no. 8, pp. 856–864, 1965.

[44] R. Garbacz and R. Turpin, "A generalized expansion for radiated and scattered fields", *IEEE Transactions on Antennas and Propagation*, vol. 19, no. 3, pp. 348–358, 1971.

[45] ANSYS, *High frequency structure simulator*, 2018.

[46] L. J. Chu, "Physical limitations of omni-directional antennas", *Journal of applied physics*, vol. 19, no. 12, pp. 1163–1175, 1948.

[47] Z. Bayraktar, M. Komurcu, Z. H. Jiang, D. H. Werner, and P. L. Werner, "Stub-loaded inverted-f antenna synthesis via wind driven optimization", in *2011 IEEE International Symposium on Antennas and Propagation (APSURSI)*, IEEE, 2011, pp. 2920–2923.

[48] D. Liu and B. Gaucher, "The inverted-f antenna height effects on bandwidth", in *2005 IEEE Antennas and Propagation Society International Symposium*, IEEE, vol. 2, 2005, pp. 367–370.